



## **The Plasma Way to Ammonia**

Modelling and Understanding Plasma-Derived NH<sub>3</sub>

**Armando Rafael Pires Gonçalves**

Thesis to obtain the Master of Science Degree in

**Engineering Physics Technology**

Supervisors: Prof. Luís Lemos Alves  
Dr. Olivier Guaitella

**September 2025**



# **Declaration**

I declare that this document is an original work of my own authorship and that it fulfills all the requirements of the Code of Conduct and Good Practices of the Universidade de Lisboa.



*Lorem ipsum dolor sit amet, consectetur adipiscing elit, sed do eiusmod tempor incididunt ut labore et dolore magna aliqua  
quaerat.*

- Lorem I. Dolor

This work was created using the Typst typesetting language.



# Acknowledgments

Lorem ipsum dolor sit amet, consectetur adipiscing elit, sed do eiusmod tempor incididunt ut labore et dolore magna aliquam quaerat voluptatem. Ut enim aequo doleamus animo, cum corpore dolemus, fieri tamen permagna accessio potest, si aliquod aeternum et infinitum impendere malum nobis opinemur. Quod idem licet transferre in voluptatem, ut postea variari voluptas distingue possit, augeri amplificarique non possit. At etiam Athenis, ut e patre audiebam facete et urbane Stoicos irridente, statua est in quo a nobis philosophia defensa et collaudata est, cum id, quod maxime placeat, facere possimus, omnis voluptas assumenda est, omnis dolor repellendus. Temporibus autem quibusdam et aut officiis debitibus aut rerum necessitatibus saepe eveniet, ut et voluptates repudiandae sint et molestiae non recusandae. Itaque earum rerum defuturum, quas natura non depravata desiderat. Et quem ad me accedis, saluto: 'chaere,' inquam, 'Tite!' lictores, turma omnis chorusque: 'chaere, Tite!' hinc hostis mi Albucius, hinc inimicus. Sed iure Mucius.

  Lorem ipsum dolor sit amet, consectetur adipiscing elit, sed do eiusmod tempor incididunt ut labore et dolore magna aliquam quaerat voluptatem. Ut enim aequo doleamus animo, cum corpore dolemus, fieri.



# **Abstract**

Lorem ipsum dolor sit amet, consectetur adipiscing elit, sed do eiusmod tempor incididunt ut labore et dolore magna aliquam quaerat voluptatem. Ut enim aequo doleamus animo, cum corpore dolemus, fieri tamen permagna accessio potest, si aliquod aeternum et infinitum impendere malum nobis opinemur. Quod idem licet transferre in voluptatem, ut postea variari voluptas distingue possit, augeri amplificarique non possit. At etiam Athenis, ut e patre audiebam facete et urbane Stoicos irridente, statua est in quo a nobis philosophia defensa et collaudata est, cum id, quod maxime placeat, facere possimus, omnis.

Lorem ipsum dolor sit amet, consectetur adipiscing elit, sed do eiusmod tempor incididunt ut labore et dolore magna aliquam quaerat voluptatem. Ut enim aequo doleamus animo, cum corpore dolemus, fieri.

## **Keywords**

Lorem, Ipsum, Dolor, Sit, Amet



# Resumo

  Lorem ipsum dolor sit amet, consectetur adipiscing elit, sed do eiusmod tempor incididunt ut labore et dolore magna aliquam quaerat voluptatem. Ut enim aequo doleamus animo, cum corpore dolemus, fieri tamen permagna accessio potest, si aliquod aeternum et infinitum impendere malum nobis opinemur. Quod idem licet transferre in voluptatem, ut postea variari voluptas distingue possit, augeri amplificarique non possit. At etiam Athenis, ut e patre audiebam facete et urbane Stoicos irridente, statua est in quo a nobis philosophia defensa et collaudata est, cum id, quod maxime placeat, facere possimus, omnis.

  Lorem ipsum dolor sit amet, consectetur adipiscing elit, sed do eiusmod tempor incididunt ut labore et dolore magna aliquam quaerat voluptatem. Ut enim aequo doleamus animo, cum corpore dolemus, fieri.

## Palavras Chave

  Lorem, Ipsum, Dolor, Sit, Amet



# Contents

<b>1 Introduction</b>	<b>1</b>
1.1 Context and Motivation .....	2
1.1.1 Why Ammonia? .....	2
1.1.2 The PSI.COM Project .....	4
1.1.3 Challenges in Modeling N <sub>2</sub> -H <sub>2</sub> Plasma .....	5
1.2 Thesis Objectives and Structure .....	6
<b>2 Theoretical Background and State of the Art</b>	<b>9</b>
2.1 The Electron Boltzmann Equation .....	10
2.1.1 Numerical Solution of the EBE .....	13
2.2 Chemical Kinetics .....	13
2.2.1 Computational Methodologies .....	17
2.3 Machine Learning in Plasma Chemistry .....	18
<b>3 Experimental Measurements</b>	<b>21</b>
3.1 Experimental Setup and Diagnostics .....	22
3.1.1 Plasma Diagnostics .....	24
3.1.1.1 Electrical Probes .....	27
3.2 Experimental Campaign at LPP .....	27
3.2.1 Campaign objectives and methodology .....	27
3.2.2 Measurement protocols and procedures .....	28
3.2.3 Data acquisition and processing .....	28
3.2.4 Reproducibility assessment .....	29
3.3 Results and Analysis .....	29
3.3.1 Gas and Wall Temperatures .....	29
3.3.2 [NH <sub>3</sub> ] vs Temperature Analysis .....	29
3.3.3 Discharge characteristics (E/N vs NR) .....	30
3.3.4 Species density profiles .....	30
3.3.5 Spectra from LPP Laboratory .....	30
3.3.6 Ammonia production rates .....	31
3.3.7 Model validation and refinement needs .....	31
<b>4 Modelling of N<sub>2</sub> – H<sub>2</sub> Plasmas</b>	<b>33</b>
4.1 Chemical Model Development .....	34
4.1.1 Mesoscopic Surface Model .....	40

4.1.2 Implementation in LoKI-B+C .....	44
4.2 Validation of the Chemical Model .....	48
4.2.1 Simulation setup in LoKI .....	48
4.2.1.1 Analysis of Experimental Conditions and Methodologies .....	48
4.2.2 Results and Discussion .....	50
4.2.2.1 Electrical Characteristics: Electric Field and Reduced Electric Field .....	50
4.2.2.2 Atomic Species Concentration in $N_2$ - $H_2$ Mixtures .....	52
4.2.2.3 Ammonia ( $NH_3$ ) Synthesis .....	54
4.2.2.4 Additional Validation: Reduced Electric Field in $N_2$ - $H_2$ Mixtures .....	56
<b>5 Tool Development</b>	<b>63</b>
5.1 Variable Energy Grid Implementation in LoKI-B .....	64
5.1.1 Motivation for variable grids .....	64
5.1.2 Geometric progression approach .....	64
5.1.3 Discrete operator implementation .....	64
5.1.4 Conservation properties and numerical stability .....	64
5.1.5 Performance benchmarking .....	65
5.1.6 Computational efficiency gains .....	65
5.1.7 Accuracy preservation .....	65
5.1.8 Optimal grid parameters .....	66
5.1.9 Comparison with fixed grids .....	66
5.2 Graphical User Interface Development .....	66
5.2.1 User experience requirements .....	66
5.2.2 MATLAB GUI design principles .....	67
5.2.3 Integration with LoKI-B solver .....	67
5.2.4 Workflow optimization for researchers .....	67
5.3 Machine Learning Framework for Scheme Reduction .....	68
5.3.1 Petri net representation of reaction networks .....	68
5.3.2 Training data preparation from LoKI simulations .....	68
5.3.3 Algorithm development and validation .....	68
5.3.4 Automated identification of non-essential reactions .....	69
5.4 Results and Performance Analysis .....	69
5.4.1 ML model performance .....	69
5.4.2 Identified non-essential reactions .....	70
5.4.3 Reduced scheme validation .....	70
5.4.4 Computational savings .....	70

<b>6 Conclusions and Future Work</b>	<b>71</b>
6.1 Summary of Achievements .....	72
6.1.1 Main contributions of the thesis .....	72
6.1.2 Integration of all developed components .....	72
6.2 Impact on N <sub>2</sub> -H <sub>2</sub> Plasma Modeling .....	73
6.2.1 Improved accuracy and efficiency .....	73
6.2.2 Enhanced experimental validation capabilities .....	73
6.3 Future Research Directions .....	74
6.3.1 Extension to other gas mixtures .....	74
6.3.2 Upgrade of the Variable Energy Grid Implementation .....	74
6.3.2.1 Discrete operators .....	74
6.3.2.2 User-defined energy grids .....	74
6.3.3 Advanced ML techniques .....	74
6.4 Publications and Dissemination .....	75
6.4.1 Conference presentations .....	75
6.4.2 Software distribution .....	75
<b>Bibliography</b>	<b>77</b>
<b>A Mathematical Derivations</b>	<b>83</b>
A.1 Complete derivation of the Electron Boltzmann Equation .....	83
A.1.1 Kinetic theory foundation .....	83
A.1.2 Force term derivation .....	83
A.1.3 Collision integral formulation .....	83
A.1.4 Final equation form .....	83
A.2 Two-term approximation mathematical details .....	84
A.2.1 Spherical harmonic expansion .....	84
A.2.2 Isotropic equation derivation .....	84
A.2.3 Anisotropic equation derivation .....	84
A.2.4 Collision terms .....	84
A.3 Discrete operator derivations for variable grids .....	84
A.3.1 Finite difference approximations .....	84
A.3.2 Conservation-based discretization .....	84
A.3.3 Matrix formulation .....	85
A.4 Conservation laws in discretized form .....	85
A.4.1 Particle conservation .....	85
A.4.2 Energy conservation .....	85

A.4.3 Positivity preservation .....	85
A.4.4 Numerical implementation .....	86
<b>B Computational Implementation Details</b>	<b>87</b>
B.1 Variable grid algorithm pseudocode .....	87
B.1.1 Main algorithm structure .....	87
B.1.2 Grid generation algorithm .....	88
B.1.3 Conservation enforcement .....	88
B.2 Discrete operator matrix assembly .....	89
B.2.1 Matrix structure .....	89
B.2.2 Collision operator assembly .....	89
B.2.3 Field operator assembly .....	90
B.3 GUI software architecture .....	90
B.3.1 Main GUI structure .....	90
B.3.2 Parameter input handling .....	91
B.3.3 Result visualization .....	91
B.4 ML model training procedures .....	92
B.4.1 Data preparation .....	92
B.4.2 Model training .....	92
B.4.3 Model validation .....	93
B.4.4 Performance evaluation .....	94
<b>C Experimental Data and Protocols</b>	<b>95</b>
C.1 Complete experimental datasets .....	95
C.1.1 Discharge characteristics data .....	95
C.1.2 Wall Temperature measurements .....	95
C.1.3 Ammonia production data .....	96
C.2 Measurement protocols and procedures .....	96
C.2.1 Gas handling protocols .....	96
C.2.2 Discharge operation protocols .....	96
C.2.3 Diagnostic calibration procedures .....	97
C.2.4 Data acquisition protocols .....	97
C.3 Error analysis and uncertainty estimation (this is standard stuff, although I didn't do it) .....	97
C.3.1 Systematic error analysis .....	97
C.3.2 Random error analysis .....	98
C.3.3 Uncertainty propagation .....	98
C.3.4 Validation procedures .....	98

C.4 Equipment specifications and calibration .....	99
C.4.1 FTIR specifications .....	99
C.4.2 Optical emission spectrometer specifications .....	99
C.4.3 LIF system specifications .....	99
C.4.4 Electrical measurement specifications .....	100
C.4.5 Calibration procedures .....	100
<b>D Kinetic Data Compilation</b>	<b>101</b>
D.1 Complete rate coefficient database .....	101
D.1.1 Electron-impact cross-sections .....	101
D.1.2 Heavy species rate coefficients .....	101
D.1.3 Excited state reactions .....	102
D.2 Cross-sections and Data Validation .....	102
D.2.1 What is a cross-section? .....	102
D.2.2 Experimental data sources .....	103
D.2.3 Theoretical data sources .....	103
D.2.4 Validation procedures .....	103
D.2.5 Recommended values .....	104
D.3 Comparison tables between different authors .....	104
D.3.1 N <sub>2</sub> cross-section comparisons .....	104
D.3.2 H <sub>2</sub> cross-section comparisons .....	105
D.3.3 Heavy species reaction comparisons .....	105
D.3.4 Statistical analysis .....	105
D.4 Recommended values with uncertainties .....	106
D.4.1 Selection methodology .....	106
D.4.2 Uncertainty quantification .....	106
D.4.3 Temperature and pressure dependence .....	106
D.4.4 Validation against experiments .....	107
<b>E Software Documentation</b>	<b>109</b>
E.1 LoKI-B modifications and new features .....	109
E.1.1 Variable grid implementation .....	109
E.1.2 Performance optimizations .....	109
E.1.3 New input/output capabilities .....	110
E.1.4 Integration with other tools .....	110
E.2 GUI user manual .....	110
E.2.1 Installation and setup .....	110

E.2.2 Basic operation .....	111
E.2.3 Advanced features .....	111
E.2.4 Troubleshooting guide .....	111
E.3 ML framework documentation .....	112
E.3.1 Framework architecture .....	112
E.3.2 Model training procedures .....	112
E.3.3 Model evaluation .....	112
E.3.4 Usage examples .....	113
E.4 Installation and usage guides .....	113
E.4.1 System requirements .....	113
E.4.2 Installation procedures .....	113
E.4.3 Configuration options .....	114
E.4.4 Usage tutorials .....	114
<b>F Additional Results</b>	<b>115</b>
F.1 Extended simulation results...? .....	115
F.2 Sensitivity analysis details? .....	115
F.2.1 Global sensitivity analysis .....	115
F.2.2 Local sensitivity analysis .....	115
F.2.3 Reaction sensitivity analysis .....	116
F.2.4 Output sensitivity analysis .....	116
F.3 Performance benchmarking data .....	116
F.3.1 Computational performance .....	116
F.3.2 Accuracy benchmarking .....	117
F.3.3 Robustness testing .....	117
F.3.4 User experience benchmarking :) (got this one from Game Design course) .....	117
F.4 Statistical analysis supplementary material?? .....	118
F.4.1 Statistical methods .....	118
F.4.2 Data analysis procedures .....	118
F.4.3 Validation procedures .....	118
F.4.4 Quality assessment .....	119

# List of Figures

1.1 Natural Nitrogen Conversion Processes.....	2
2.1 Example of Petri net for the reaction $N_2 + 3H_2 \rightarrow 2NH_3$ .....	19
3.1 Simple schematic of a DC glow discharge system, adapted from [1].....	22
3.2 RF discharge setup showing match box and electrode configuration.....	24
4.1 Validation of swarm parameters for $H_2$ and $NH_3$ .....	47
4.2 Axial electric field ( $E$ ) as a function of discharge current ( $I$ ) in pure nitrogen plasma at two pressures: 133 Pa (purple) and 266 Pa (orange). Points and crosses represent experimental data from Cernogora and Brovikova, while solid and dashed lines show simulation results with Cernogora and Brovikova data, respectively.....	50
4.3 Left: Reduced electric field ( $E/N$ ) in Td. Right: Electric field ( $E$ ) in V cm <sup>-1</sup> . Both as a function of $NR$ (gas density times tube radius) for a fixed current of 40 mA in pure nitrogen. Simulation lines follow experimental (points) trends from Cernogora and Brovikova datasets.....	51
4.4 Reduced electric field ( $E/N$ ) in pure hydrogen plasma as a function of $NR$ . The simulation (solid line) shows excellent agreement with experimental measurements from Amorim <i>et al.</i> [2].....	52
4.5 Concentration of atomic nitrogen ([N]) as a function of $H_2$ percentage in the discharge, for Amorim <i>et al.</i> [2] data. The simulation captures the catalytic effect of hydrogen on nitrogen dissociation, showing a peak enhancement around 1-2% $H_2$ .....	53
4.6 Relative concentration of atomic hydrogen ([H]) as a function of $H_2$ percentage. The simulation shows excellent quantitative agreement with three different experimental datasets, namely Amorim <i>et al.</i> [2], across the entire composition range.....	53
4.7 Absolute concentration of ammonia ( $[NH_3]$ ) as a function of $H_2$ percentage, for Amorim <i>et al.</i> [2] data. The orange line shows the simulation result scaled by a factor of 3 for comparison.....	54
4.8 Sensitivity of predicted $[NH_3]$ concentration to gas residence time in the plasma. Different lines represent simulations with residence times of 5 ms (blue), 10 ms (orange), 20 ms (green), for Amorim <i>et al.</i> [2] data. The 10 ms residence time provides the best fit to experimental data.....	55
4.9 Reduced electric field ( $E/N$ ) as a function of hydrogen percentage ( $H_2\%$ ) for two pressure conditions: 266.0 Pa (blue) and 665.0 Pa (orange). Shaded bands represent simulation results with uncertainty ranges, while points with error bars show experimental measurements from LPP..	
	56



# List of Tables

4.1 Forward rate coefficients for N <sub>2</sub> -H <sub>2</sub> chemistry.....	35
4.2 Reverse rate coefficients for N <sub>2</sub> -H <sub>2</sub> chemistry.....	38
4.3 Summary of operational parameters.....	48



# List of Algorithms

4.1 Mesoscopic surface model reactions for N <sub>2</sub> -H <sub>2</sub> system - Part 1: Core reactions (Gordiets <i>et al.</i> 1998).....	41
4.2 Mesoscopic surface model reactions for N <sub>2</sub> -H <sub>2</sub> system - Part 2: NH <sub>3</sub> synthesis pathway.....	42
4.3 Mesoscopic surface model reactions for N <sub>2</sub> -H <sub>2</sub> system - Part 3: Metastable species mechanisms	42
4.4 Example reactions from N2H2_CS18a.chem kinetic scheme.....	45
4.5 NH <sub>3</sub> electronic excitation cross-section snippet taken from LXCat.....	45
4.6 H <sub>2</sub> vibrational excitation cross-section snippet taken from LXCat.....	46
4.7 Example configuration file (N2H2_simulation.in) for LoKI-B+C simulations of N <sub>2</sub> -H <sub>2</sub> plasmas... .	58



# **Glossary**

## **Abbreviations**

## **Symbols**



# 1

## Introduction

## Contents

---

1.1 Context and Motivation .....	2
1.2 Thesis Objectives and Structure .....	6

---

## 1.1 Context and Motivation

*“You are what you eat”.*

Some of us consume meat, others set their limit to fish. Some choose the vegan path, while others embrace peculiar diets like the cabbage soup one[3]. Yet, regardless of our culinary preferences, nearly all of our food — around 90%[4] — comes from the same age-old origin: **agriculture**. Beyond the small contributions of wild seafood and hunting, human sustenance is overwhelmingly a product of managed agricultural systems[5].

These systems, however, were governed for millennia by an immutable bottleneck that no civilization could escape. The **natural nitrogen cycle**.

### 1.1.1 Why Ammonia?

**Nitrogen (N)**, in its diatomic form ( $N_2$ ), is the most abundant gas in Earth’s atmosphere. Being largely inert, it’s when combined with **Hydrogen (H<sub>2</sub>)** to form **Ammonia (NH<sub>3</sub>)** that it unlocks its full biological potential. The continuous transformation of nitrogen between the atmosphere, land, and living organisms constitutes the biogeochemical **nitrogen cycle**, a planetary-scale process. The conversion of nitrogen into usable ammonia, known as **nitrogen fixation**, occurs through several natural pathways[6], [7], [8]:

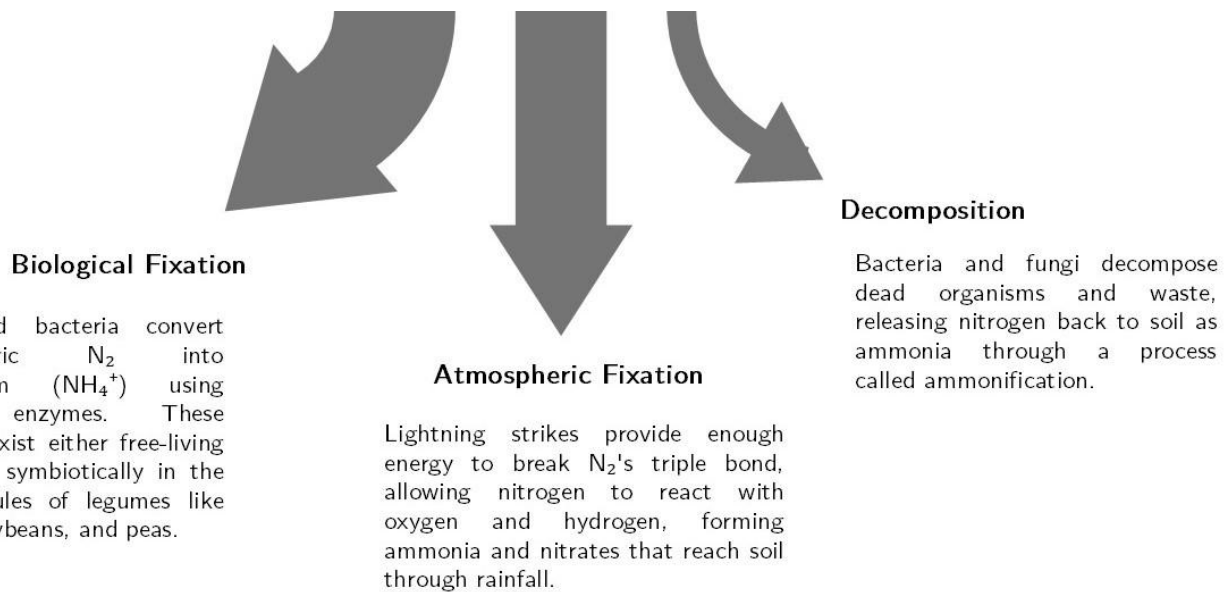


**Figure 1.1:** Natural Nitrogen Conversion Processes

Once fixed into ammonia or ammonium, nitrogen enters the food web. Soil bacteria can further convert ammonia into nitrites (NO<sub>2</sub><sup>-</sup>) and then nitrates (NO<sub>3</sub><sup>-</sup>) through a process called **nitrification**. Plants absorb these nitrogen compounds from the soil through their roots, assimilating them to build proteins and DNA. Animals, in turn, acquire this essential nitrogen by consuming plants or other animals [9], [10].

Because the natural conversion of inert  $N_2$  into bioavailable ammonia is a slow and finite process, the supply of fixed nitrogen is the primary limiting nutrient for growth in most terrestrial and aquatic ecosystems. The productivity of land was indeed limited by the availability of naturally fixed nitrogen for thousands of years, forcing reliance on practices like crop rotation with legumes and the use of animal manure[11]. This fundamental limit was shattered in the early 20th century with the invention of the **Haber-Bosch** process, an industrial procedure that effectively hijacks the planetary nitrogen cycle and represents one of the most significant technological advancements in human history[12].

Developed by German chemists **Fritz Haber** and **Carl Bosch**, the process synthesizes ammonia from its constituents:



To achieve this, the process requires extreme conditions; a mixture of nitrogen, cryogenically separated from the air, and hydrogen is subjected to very high pressures (typically 50–200 bar) and high temperatures (400–500°C) in the presence of a metal catalyst, most commonly iron-based[13].

The historical and societal impact of the Haber-Bosch process cannot be overstated - it provided, for the first time, a cheap, scalable, and seemingly limitless source of nitrogen fertilizer, breaking humanity's dependence on finite natural sources like mined Chilean saltpetre[12]. The widespread application of ammonia-based fertilizers is credited with preventing mass starvation and supporting a global population that has grown from 1.6 billion in 1900 to over 8 billion today. It is estimated that synthetic nitrogen fertilizers are used to grow the food that sustains half of the current global population[14].

Today ammonia is the second most synthesized chemical on Earth, only behind to sulfuric acid ( $H_2SO_4$ ), with global industrial production reaching 180 million tonnes in 2021[15], [16]. And the reality is that ammonia is not only important for agricultural uses. In fact, it is also used extensively across diverse industrial sectors due to its unique chemical and thermodynamic properties. In refrigeration applications, ammonia serves as one of the most efficient industrial coolants, with its low boiling point and high heat absorption capacity making it ideal for large-scale food processing facilities, cold storage operations, and industrial cooling systems[17], [18]. The chemical industry relies heavily on ammonia as a fundamental building block for synthesizing plastics[19], synthetic fibers like nylon[20], and numerous pharmaceutical compounds, including common medications such as antibiotics and analgesics[21], [22].

Beyond manufacturing, ammonia also serves essential environmental and industrial stabilization functions, including water disinfection through chloramine formation[23], air pollution control by converting harmful nitrogen oxides into benign compounds[24], [25], metal processing applications for both protective atmospheres and ore extraction[26], [27], petroleum refining for acid neutralization[28], and rubber production for latex stabilization[29].

The global shift to hydrogen as a clean energy source faces a critical challenge: hydrogen's extremely low energy density requires either high-pressure compression (700 bar) or cryogenic liquefaction (-253°C) for storage and transport, making it costly and logistically complex[30]. Ammonia's name emerges again, this time as a hydrogen carrier solution, since it can be stored as a liquid under manageable conditions (boiling point of liquid ammonia at atmospheric pressure is -33.3°C[31], far less

extreme than hydrogen's requirements). Unlike hydrogen, which lacks global infrastructure, ammonia benefits from an established worldwide supply chain with existing production facilities, pipelines, port terminals, and marine tankers developed over decades of commercial use. This infrastructure advantage could accelerate hydrogen economy deployment. The proposed value chain involves producing ammonia where renewable energy is abundant, transporting it in liquid form globally, and then "cracking" it at destination points to release high-purity hydrogen through catalytic decomposition.

—[missing references]—

Ammonia can also function directly as a direct zero-carbon fuel, producing only nitrogen and water when combusted, in ideal conditions ( $4\text{NH}_3 + 3\text{O}_2 \rightarrow 2\text{N}_2 + 6\text{H}_2\text{O}$ ). Major engine manufacturers and companies like Toyota are developing ammonia-fueled engines for ships and trucks. **High-temperature Solid Oxide Fuel Cells (SOFCs)** offer more efficient energy conversion by directly decomposing ammonia at temperatures above 600°C. Key challenges include developing durable catalysts for breaking N-H bonds, preventing ammonia crossover through membranes, and ensuring long-term stability.

With no big surprise, the ammonia industry is enormous. In 2024 the global market was \$224 billion. Analysts forecast steady growth (CAGR 2–6%) as agriculture demand rises and new energy uses develop. By 2030 value may exceed \$300 billion. Current global  $\text{NH}_3$  production is on the order of 150–200 million tonnes per year, with one report projecting demand growing from ~150 Mt in 2024 to ~190 Mt by 2034.

This transformative power, however, comes with an enormous energy and environmental cost. The Haber-Bosch process is one of the most energy-intensive industrial processes in the world. Its operation accounts for an estimated 1-2% of total global energy consumption and 3-5% of global natural gas consumption [MISSING REFERENCES!!]. This heavy reliance on fossil fuels for the energy to run the high-pressure reactors makes ammonia production a massive source of greenhouse gas emissions. The industry is responsible for approximately 1.3-1.8% of global anthropogenic  $\text{CO}_2$  emissions. With every tonne of ammonia produced through conventional methods, 2.7 tonnes of  $\text{CO}_2$  are released into the atmosphere. As this essential chemical accounts for 1-2% of global energy consumption and 1.3% of all human-caused carbon emissions, it is imperative to seek new solutions that allow us to obtain this vital raw material in greener, more efficient, and less polluting ways. And that's exactly where the plasmas come in.

### 1.1.2 The PSI.COM Project

The Plasma Surface Interaction and COupled Modelling (PSI.COM) project focuses on advancing the understanding and modelling of plasma-surface chemistry in  $\text{N}_2 - \text{H}_2$  mixtures. Its core objectives include bridging the gap between plasma volume and surface reactivity, leveraging experimental measurements with kinetic simulations, and optimizing chemistry schemes for more efficient modelling.

PSI.COM brings together the complementary expertise of the N-PRiME group (IPFN, Instituto Superior Técnico, Lisbon, Portugal) and LPP (École Polytechnique, Palaiseau, France) in low-temperature plasma modelling and diagnostics. Key tasks include investigating  $\text{N}_2 - \text{H}_2$  plasmas for ammonia production, enhancing the LisbOn Kinetics (LoKI) tool suite [32] to improve the coupling between its

Chemistry and Boltzmann components and to incorporate surface reactions and machine learning-based sensitivity analysis, and contributing to the development of an open-access data-storage library in collaboration with LXCat tech-team [33].

Plasma-assisted ammonia synthesis offers several potential advantages over conventional methods, including operation at lower temperatures and pressures, reduced energy consumption, and the ability to utilize renewable energy sources. However, the complex interplay between electron kinetics, heavy species chemistry, and surface processes in N<sub>2</sub>-H<sub>2</sub> plasmas presents significant challenges for both experimental characterization and theoretical modeling.

Accurate plasma modeling is essential for understanding the underlying mechanisms, optimizing process parameters, and scaling up from laboratory to industrial applications. The development of reliable kinetic models requires comprehensive knowledge of electron-molecule interactions, reaction pathways, and rate coefficients across a wide range of conditions.

Despite significant advances in plasma modeling over the past decades, several challenges persist in accurately describing N<sub>2</sub>-H<sub>2</sub> plasma chemistry, namely the complexity of electron kinetics, the completeness of reaction mechanisms, the accuracy of rate coefficients, and the overall computational cost. Addressing these challenges forms the primary motivation for this work.

### 1.1.3 Challenges in Modeling N<sub>2</sub>-H<sub>2</sub> Plasma

Despite significant advances in plasma modeling over the past decades, several fundamental challenges persist in accurately describing N<sub>2</sub>-H<sub>2</sub> plasma chemistry, necessitating well grounded computational approaches to handle the inherent complexity of these systems.

The electron energy distribution function (EEDF) in molecular gases exhibits highly complex, non-Maxwellian structures due to multiple inelastic collision processes including vibrational excitation, electronic transitions, and rotational coupling. Unlike atomic plasmas where the EEDF can often be approximated by simple analytical functions, molecular systems require sophisticated numerical methods such as Boltzmann equation solvers or Monte Carlo techniques to accurately capture the intricate energy distribution patterns. These non-equilibrium effects become particularly pronounced at low pressures and moderate electron densities, where electron kinetic features are dominant.

The N<sub>2</sub>-H<sub>2</sub> plasma system encompasses an extraordinarily complex network involving hundreds of possible reaction pathways. This includes electronic excitations to multiple excited states of N<sub>2</sub> and H<sub>2</sub>, extensive vibrational and rotational ladder climbing processes, dissociation channels producing various atomic and molecular fragments (N, H, NH, NH<sub>2</sub>, NH<sub>3</sub>), ionization processes creating positive ions (N<sub>2</sub><sup>+</sup>, H<sub>2</sub><sup>+</sup>, NH<sub>4</sub><sup>+</sup>, etc.) and electrons, three-body recombination reactions, and surface-mediated processes involving adsorption, desorption and diffusion, which contribute to heterogeneous catalysis. The coupling between gas-phase and surface chemistry adds another layer of complexity, particularly in determining the balance between bulk production and surface loss mechanisms.

Many critical rate coefficients, particularly those involving electronically excited species and vibrationally excited molecules, suffer from significant uncertainties or complete absence of experimental data. The temperature dependencies of these rates, often following non-Arrhenius behavior due to quantum

effects, are frequently unknown or poorly characterized. This is especially problematic for reactions involving highly excited  $N_2$  vibrational states, which can dramatically alter the dissociation pathways and overall plasma chemistry. Additionally, the coupling between different energy modes (translational, rotational, vibrational, electronic) in non-equilibrium conditions requires careful consideration of mode-specific rate coefficients.

Full kinetic models incorporating electron kinetics, detailed state-to-state chemistry, and transport phenomena are computationally prohibitive for many practical applications. The stiff nature of the resulting ordinary differential equation systems, spanning timescales from femtoseconds (electron processes) to seconds (diffusion and surface processes), demands robust numerical algorithms and significant computational resources. This computational burden severely limits the feasibility of extensive parameter studies, optimization campaigns, and real-time process control applications.

Ideally, describing the interaction between electrons, ions, and neutral species with reactor surfaces should include processes such as secondary electron emission, ion-induced desorption, surface recombination, and plasma-surface charge exchange. The surface properties, including material composition, roughness, and contamination, may influence significantly these interactions and should be carefully characterized and modeled. However, considering these effects introduces additional complexity to the modeling effort.

## 1.2 Thesis Objectives and Structure

This thesis is structured to systematically address the challenges in  $N_2 - H_2$  plasma modelling. Each chapter builds upon the last, culminating in a comprehensive and validated framework for modeling plasma-assisted ammonia synthesis.

The work begins in **Chapter 2**, which lays the **Theoretical Foundation** for the entire thesis. It provides a detailed overview of low-temperature plasma physics, the formulation of the electron Boltzmann equation, and the principles of chemical model used for understanding  $N_2 - H_2$  plasma kinetics.

**Chapter 3** is dedicated to the **Experimental Measurements** that form the empirical basis for this work. A central objective is to ground the simulations in physical reality; therefore, this chapter details the experimental setup at LPP, the diagnostic techniques employed, and the data acquisition protocols used to characterize the  $N_2 - H_2$  plasma discharges.

With the established theoretical and experimental groundwork, **Chapter 4** details the **Modelling of NH<sub>3</sub> Plasmas**. This chapter explains the construction of the kinetic models for both surface and volume, incorporating the reaction schemes, the rate coefficients and the cross-section data relevant to the system. It also presents the validation of these models, identifying the key creation and destruction mechanisms of the most relevant plasma species.

**Chapter 5** documents the **Tool Development** executed during this work. This chapter presents specific contributions to the LisbOn Kinetics (LoKI) tool suite. The technical work includes the implementation of the continuous operators of the Electron Boltzmann Equation (EBE) on a variable energy grid,

in addition to the benchmarking against results obtained from uniform energy grid. It also presents the development of a Graphical User Interface (GUI) for the Input of the numerical solver. (aplicar chatgpt)

[Furthermore, this chapter covers the application of machine learning methods to perform sensitivity analysis and to identify non-essential reactions, enabling automated reaction scheme reduction.]

Finally, **Chapter 6** presents the **Conclusions**. This chapter summarizes the results from the preceding chapters, discusses the implications of these results for the field of plasma-assisted ammonia synthesis, and proposes directions for future work. The contributions of the thesis, such as the additions to the LoKI simulation tool, are presented.



# 2

## Theoretical Background and State of the Art

### Contents

---

2.1 The Electron Boltzmann Equation .....	10
2.2 Chemical Kinetics .....	13
2.3 Machine Learning in Plasma Chemistry .....	18

---

Plasma is often referred to as the fourth state of matter, consisting of a quasi-neutral, ionized gas composed of electrons, ions, and neutral particles, exhibiting a collective behavior. This state of matter is, in fact, the most prevalent in the observable universe, constituting stars and the vast interstellar medium. The presence of charge carriers makes plasma electrically conductive and highly responsive to electromagnetic fields.

Plasmas can be broadly categorized based on the degree of thermal equilibrium between their constituent particles. In thermal plasmas, frequent collisions among all particles lead to a state of local thermodynamic equilibrium (LTE), where the electrons and heavy species (ions and neutral atoms or molecules) share a common, typically very high, temperature.

Conversely, the plasmas utilized for ammonia synthesis are non-thermal or non-equilibrium plasmas, often referred to as low-temperature plasmas (LTPs) or cold plasmas. In these systems, electrons are accelerated by external electric fields far more efficiently than the ions, due to their extremely small mass and high mobility. The energy gained by electrons from the field is then dissipated through elastic and inelastic collisions. Although the frequency of electron-neutral elastic collisions is considerably high, the corresponding energy transfer is very inefficient since it scales with the electron-to-heavy-species mass ratio,  $\frac{m_e}{m_h}$ . Consequently, a profound state of non-equilibrium is established, characterized by highly energetic electrons coexisting with heavy species that remain near ambient temperature. Electron temperatures ( $T_e$ ) can reach values of 1–10 electron-volts (eV), equivalent to approximately 11,600–116,000 K, while the temperatures of the neutral gas species ( $T_g$ ) and the ions ( $T_i$ ) remain low, typically in the range of 300–1000 K. This fundamental property of LTPs is the cornerstone of applications involving cold plasmas, namely ammonia synthesis, since it allows for the generation of a highly reactive chemical environments. Without the need for bulk gas heating, the high energy costs of conventional thermocatalytic methods are effectively circumvented.

Another key parameter defining these systems is the degree of ionisation,  $\alpha$ , corresponding to the ratio of the electron number density ( $n_e$ ) to the total number density of heavy particles ( $n_g$ ). For LTPs used in chemical synthesis, the plasma is typically weakly or partially ionized, with  $\alpha$  often in the range of  $10^{-5}$  to  $10^{-4}$ . This means that the plasma is composed predominantly of neutral gas particles. As a result, electron-neutral collisions are the most relevant kinetic processes, initiating the entire chain of chemical reactions that leads to product formation. These high collisionality processes can be studied using the Electron Boltzmann Equation.

## 2.1 The Electron Boltzmann Equation

The Electron Boltzmann Equation (EBe) provides a rigorous, statistical description of the electron kinetics in a plasma, moving beyond simplistic assumptions of thermal equilibrium.

The EBe describes the evolution of the **electron distribution function (EDF)** in phase space. This distribution function,  $f(\vec{r}, \vec{v}, t)$ , represents the probability density of finding electrons at position  $\vec{r}$  with velocity  $\vec{v}$  at time  $t$  in a six-dimensional phase space. The quantity  $f(\vec{r}, \vec{v}, t) d\vec{r} d\vec{v}$  represents the number of electrons within an infinitesimal volume element  $d\vec{r}$  around position  $\vec{r}$  and  $d\vec{v}$  around velocity  $\vec{v}$ , at

time  $t$ . The equation itself is a statement of conservation of particles in phase space, accounting for all processes that can change the number of electrons in a given phase-space element.

The general form of the Boltzmann equation for a particle of mass  $m$  is:

$$\frac{\partial f}{\partial t} + \vec{v} \cdot \nabla_r f + \frac{\vec{F}}{m} \cdot \nabla_v f = \left( \frac{\partial f}{\partial t} \right)_{\text{coll}} \quad (2.1)$$

Each term in this equation has a distinct physical meaning:

- $\frac{\partial f}{\partial t}$ : The change in  $f$  due to the intrinsic time evolution of the distribution function.
- $\vec{v} \cdot \nabla_r f$ : The change in  $f$  due to the motion of electrons in configuration space (spatial transport or convection).
- $\frac{\vec{F}}{m} \cdot \nabla_v f$ : The change in  $f$  due to particle acceleration by a force  $\vec{F}$ , which, for charged particles, is typically the Lorentz force  $\vec{F} = q(\vec{E} + \vec{v} \times \vec{B})$  from electric ( $\vec{E}$ ) and magnetic ( $\vec{B}$ ) fields.
- $\left( \frac{\partial f}{\partial t} \right)_{\text{coll}}$ : The collision integral, which represents the rate of change of  $f$  due to collisions. This term accounts for particles being scattered into and out of the velocity element  $d\vec{v}$  through elastic and inelastic processes.

The collision integral is the most complex term, as it involves an integration over all possible collision partners and scattering angles. For electrons, it encapsulates the microphysics of electron-neutral, electron-ion, and electron-electron interactions.

The EBE has a great physical significance. Its solution bridges the microscopic physics of individual collisions (encoded in the cross-sections, see Section D.2.1, within the collision integral) and the macroscopic properties of the plasma. Once the EDF is known, macroscopic parameters can be calculated self-consistently by taking appropriate integrals of the distribution function. These macroscopic parameters, such as electron transport parameters (mobility  $\mu_e$ , diffusion coefficient  $D_e$ ) and electron-impact rate coefficients ( $k_j$ ) are essential for the fluid modelling of the plasma. This approach is fundamentally more accurate than assuming an *a priori* EDF, such as a Maxwellian distribution function, which is often not valid in the non-equilibrium conditions of interest.

The full Boltzmann equation is a complex seven-dimensional (six phase-space dimensions plus time) integro-differential equation that is computationally prohibitive to solve for most practical applications in plasma chemistry modeling. To make the problem tractable, a widely adopted and highly successful simplification known as the **small anisotropy approximation** is employed.

This approximation is based on expanding the velocity-dependent distribution function,  $f(\vec{r}, \vec{v}, t)$ , in a series of spherical harmonics (or Legendre polynomials in the one-dimensional case) in velocity space. The key physical assumption is that the electron velocity distribution is **nearly isotropic**, meaning it is dominated by its spherically symmetric component, with only a small directional perturbation caused by different effects (e.g., electric fields, density gradients and collisions). Under this assumption, the expansion can be truncated after the first **two terms** [....William P Allis]:

$$f(\vec{r}, \vec{v}, t) \approx f_0(\vec{r}, v, t) + \frac{\vec{v}}{v} \cdot \vec{f}_1(\vec{r}, v, t) \quad (2.2)$$

Here,  $f_0$  is the isotropic part of the distribution function (which depends only on the magnitude of the velocity,  $v$ ), and  $\vec{f}_1$  is the first-order anisotropic perturbation, representing a small directional flux.

Substituting this expansion into the full Boltzmann equation and performing an integration over the solid angle in velocity space allows the complex equation to be separated into a coupled system of two simpler equations for  $f_0$  and  $\vec{f}_1$ . This system can then be combined into a single, second-order partial differential equation for the isotropic part,  $f_0(u)$ , typically referred to as the **electron energy distribution function (EEDF)**, which depends only on the kinetic energy  $u$ . The equation reads:

...

Note that usually the isotropic EEDF deviates from a Maxwellian distribution. In LTPs, the energy gain from the electric field and the energy losses through various electron-neutral collisions can significantly modify the shape of the EEDF from a simple Maxwellian profile. For instance, in molecular gases, the EEDF may be strongly depleted at energies corresponding to the various thresholds of the cross-section processes. Common non-Maxwellian forms include the **Druyvesteyn distribution** [...], though in many real gas mixtures, the EEDF can be even more complex and must be calculated numerically.

The primary advantage of this two-term approximation is the immense reduction in computational complexity. It transforms the problem into a much more manageable form that can be quickly solved, enabling its use in complex plasma chemistry models where hundreds of rate coefficients must be calculated. This is the approach implemented in widely used Boltzmann solvers such as BOLSIG+ and LisbOn KInetics Boltzmann solver (LoKI-B) (see Section 2.1.1).

However, the approximation has inherent limitations tied to its core assumption of small anisotropies. This assumption holds when electron-neutral collisions are frequent and predominantly elastic, effectively randomizing the electron's velocity direction between accelerations by the electric field. The approximation can become less accurate or even fail under conditions of high anisotropies, which can occur at high values of the reduced electric field ( $E/N$ , with  $E$  the electric field and  $N$  the density of the gas), where the field-induced drift becomes significant compared to the random thermal motion.

[modificar]The specific gas mixture under study, N<sub>2</sub>-H<sub>2</sub>, presents a particular challenge to the validity of the two-term approximation. Molecular nitrogen is known for its large cross-sections for vibrational excitation in the electron energy range of 2-4 eV. These are highly inelastic processes where an electron can lose a significant fraction of its energy in a single collision. Such strong, non-randomizing energy loss mechanisms can significantly perturb the electron distribution, potentially leading to a higher degree of anisotropy than the approximation can accurately capture. This suggests that while the two-term approximation is a powerful and essential tool, its application to N<sub>2</sub>-rich plasmas requires, obviously, careful consideration.

### 2.1.1 Numerical Solution of the EBE

Several numerical methods are employed to solve the EBE. When using the two-term approximation, the differential operators are written in a discretized energy grid. Often, the discretization adopts finite difference or finite element schemes. In other cases, for example in the **BOLSIG+** solver, an exponential discretization scheme is used instead, which is particularly robust for convection-diffusion-type equations. The resulting system of algebraic equations results in a large, sparse matrix equation that can be solved using standard linear algebra techniques. Alternative approaches to solve the EBE include spectral methods, which expand the solution in a set of basis functions and can offer high accuracy, and Particle-In-Cell (PIC) Monte Carlo Collisional (MCC) methods, which simulate the trajectories of a large number of individual electrons and are not limited by the two-term approximation. [pic mcc]

The numerical solution of the EBE requires the definition of appropriate boundary conditions. For the spatially homogeneous (0D) two-term approximation (see Section 2.2), the equation is solved on a one-dimensional energy grid with boundary conditions applied in energy space. At both zero energy and maximum energy ( $u_{\max}$ ) the conservation of the electron energy flux  $G$  is imposed ( $G(0) = G(u_{\max}) = 0$ ) to prevent the accounting of electrons losing/gaining energy beyond the grid boundaries. If the model is spatially dependent (e.g., 1D in space, 1D in energy), additional boundary conditions must be specified at the physical boundaries of the plasma, such as walls or electrodes. These conditions describe physical processes like electron absorption, reflection, or secondary electron emission [zoltan donko].

This work uses LoKI-B solver, an open-source tool developed at Instituto Superior Técnico, Lisbon []. It is written in MATLAB and it solves the two-term EBE for non-magnetized plasmas excited by DC or HF electric fields. Its design philosophy emphasizes the ability to easily handle any complex any gas mixture with atomic and molecular species, including detailed descriptions of first and second-kind electron collisions with any target state (electronic, vibrational, and rotational) characterized by any population.

## 2.2 Chemical Kinetics

Chemical kinetics in plasma systems typically involve complex spatial and temporal variations in species densities, requiring sophisticated three-dimensional models to capture the full physics. However, for many practical applications, particularly in quasi-homogeneous discharge conditions, spatially averaged zero-dimensional (0D) approaches provide efficient and accurate frameworks for understanding fundamental processes. Zero-dimensional models focus on the temporal evolution of the species densities without the computational overhead of spatial description. These models are valid for well-mixed plasma conditions where transport phenomena can be described by averaged terms over the entire discharge volume. [...]

The temporal evolution of species densities in plasma kinetics is governed by rate balance equations that, for any species  $i$ , take the form:

$$\frac{dn_i}{dt} = \frac{dn_i}{dt} |_{\text{chem}} + \frac{dn_i}{dt} |_{\text{transport}} + \frac{dn_i}{dt} |_{\text{flow}} \quad (2.3)$$

This formulation separates time-evolution contributions from chemical processes (electron impact, heavy particle reactions, etc.), transport mechanisms (diffusion, drift, wall reactions, etc.) and flow (inflow and outflow from the discharge volume). The chemical term encompasses all production and loss mechanisms due to collisions between electrons, ions and neutrals (the latter two being called thereafter **heavy species**) and can generally be written as:

$$k \cdot C$$

where  $k$  is bla bla and  $C$  is bla bla...  $k_{ij}$  is the **electron rate coefficient** and  $k_{ij}^{\text{heavy}}$  is the **heavy-species rate coefficient** for the production of species  $j$  from species  $i$ . These quantities specify the frequency per unit gas density at which the specific collisions occur.

The electron rate coefficients  $k_{ij}$  are calculated using the following expression:

$$k_{ij} = \gamma \int_0^\infty u \sigma_{ij}(u) f(u) du \quad (2.4)$$

where  $\gamma = \sqrt{2 \frac{e}{m_e}}$ ,  $\sigma_{ij}(u)$  is the energy-dependent cross section for the specific process, and  $f(u)$  is the normalized EEDF. Equation (2.4) directly connects the EBE solution (non-equilibrium EEDF) to the chemical kinetics (reaction rates).

The heavy-species rate coefficients  $k_{ij}^{\text{heavy}}$  are obtained from the literature and are typically expressed using Arrhenius-like forms:

$$k_{ij}^{\text{heavy}} = p_{ij} T_g^{q_{ij}} \exp\left(-\frac{E_{ij}}{kT_g}\right) \quad (2.5)$$

where  $p_{ij}$  and  $q_{ij}$  are empirical parameters,  $T_g$  is the gas temperature,  $E_{ij}$  is the activation energy, and  $k$  is the Boltzmann constant. This form accounts for both the thermal velocity dependence (through the  $T_g^{q_{ij}}$  term) and the activation energy barrier (through the exponential term  $\exp\left(-\frac{E_{ij}}{kT_g}\right)$ ) enabling the specific reaction.

The transport terms can be generally written as

$$\frac{dn_i}{dt} |_{\text{transport}} = -(n_i \nu_{\text{charged}} + n_i \nu_{\text{neutral}}) \quad (2.6)$$

where  $\nu_{\text{charged}}$  and  $\nu_{\text{neutral}}$  represent the loss frequencies for charged and neutral species transport, respectively. This decomposed description allows for modeling specific transport mechanisms affecting charged particles (e.g., ambipolar-like diffusion, thermal flux at the wall) and neutral species (e.g., binary diffusion, multi-component diffusion).

The flow term accounts for material transport into and out of the system. The outflow term is expressed as:

$$\frac{dn_i}{dt} |_{\text{flow}} = -k_{\text{out}} n_i \quad (2.7)$$

where the outflow frequency  $k_{\text{out}}$  is determined self-consistently as to ensure particle conservation at steady-state using:

$$\frac{dp}{dt} = 0 \rightarrow \frac{1}{N} \frac{dN}{dt} + \frac{1}{T_g} \frac{dT_g}{dt} = 0 \quad (2.8)$$

(fix. also no numbers)

$$\rightarrow \frac{1}{N} \frac{dN}{dt} |_{\text{chem}} + \frac{1}{N} \frac{dN}{dt} |_{\text{flow}} + \frac{1}{T_g} \frac{dT_g}{dt} = 0 \quad (2.9)$$

$$\rightarrow \sum_i \frac{dn_i}{dt} |_{\text{flow}} = -(\frac{1}{N} \frac{dN}{dt} |_{\text{chem}} + \frac{1}{T_g} \frac{dT_g}{dt}) \cdot \left( \sum_i n_i \right) \quad (2.10)$$

$$\rightarrow k_{\text{out}} = \frac{1}{N} \frac{dN}{dt} |_{\text{chem}} + \frac{1}{T_g} \frac{dT_g}{dt} \quad (2.11)$$

where the total particle density is  $N = \sum_i n_i = p/(k_B T_g)$ .

The synthesis of ammonia at a low-temperature  $N_2 - H_2$  plasma is the result of a highly complex and interconnected network of chemical reactions. This network involves dozens of different species—including electrons, ground-state molecules and atoms, molecular radicals, ions, and electronically and vibrationally excited states—participating in hundreds of individual elementary reactions. A successful kinetic model must capture the most critical of these processes, can occur both in the gas phase (*volume*) and on the surfaces of the reactor.

The overall mechanism can be conceptually divided into three main stages: (1) electron-impact dissociation, excitation and ionization of precursor molecules in the plasma volume, (2) formation of intermediate species, and (3) synthesis of the final product, which predominantly occurs on surfaces (references... miguel jimenez, gordiets). Some highlights of the processes yielding  $NH_3$  include: the dissociation of nitrogen and hydrogen (**corrigir maiúscula**); the ionization of hydrogen and the subsequent charge-transfer mechanisms leading to the formation of  $N_2H^+$  and  $NH_4^+$ ; the collisions of atomic nitrogen and hydrogen with surfaces up to the formation of wall-adsorbed  $NH$  and  $NH_2$  radicals; finally, the surface formation of  $NH_3$  and its release into the volume.

Experimental and modeling provide strong evidence that the final, crucial steps of ammonia synthesis occur on the surfaces of the plasma reactor (e.g., the reactor walls, eventually covered by a dedicated catalyst). The surface acts as a third body, facilitating reactions between adsorbed species and providing a pathway to stabilize the final product. Two primary surface mechanisms are widely discussed:

Mechanism	Description	Example Reaction
-----------	-------------	------------------

---

<b>Eley-Rideal (ER)</b>	Reaction between a particle from the gas phase and a species that is already adsorbed onto the surface. For ammonia synthesis, this typically involves a gas-phase $H_2$ molecule reacting with an adsorbed nitrogen-containing radical.	$H_2(\text{gas}) + NH(\text{surface}) \rightarrow NH_3(\text{gas})$
<b>Langmuir-Hinshelwood (LH)</b>	Reaction between two species adsorbed on the surface. The weakly adsorbed reactant must then diffuse across the surface to find its reaction partner.	$H(\text{surface}) + NH_2(\text{surface}) \rightarrow NH_3(\text{gas})$

---

The interplay between volume and surface processes is a defining feature of plasma-assisted synthesis of ammonia. However, as important to note, the plasma volume is also a destructive environment for the final product. The same energetic species that activate  $N_2$  and  $H_2$  can also efficiently decompose  $NH_3$ , being responsible for major loss channels that limit the net yield. This establishes a clear dichotomy: the volume is primarily for precursor generation and product destruction, while the surface is for product synthesis. To capture the surface chemistry accurately, mesoscopic models are typically employed to bridge the gap between molecular-level interactions and macroscopic surface behavior.

Furthermore, modeling studies have quantified the relative importance of different pathways. A volume-averaged global model by Body and Corr [34], for example, found that the dominant ammonia production mechanism shifts with the feedstock composition. For hydrogen concentrations above 25%, the Langmuir-Hinshelwood reaction between adsorbed  $H$  and adsorbed  $NH_2$  is found to dominate. For lower hydrogen proportions, the Eley-Rideal reaction between a gas-phase  $H$  atom and an adsorbed  $NH_2$  becomes the primary route. In all cases, however, the dominant loss mechanism for ammonia is found to be electron-impact dissociation in the volume.

The network of chemical reactions leading to ammonia production contains more subtle and powerful mechanisms involving a diversity of excited states. While direct electron-impact dissociation and ionization of the ground-state precursors is possible, it is an energetically expensive process. Energy-efficient pathways proceed via electronic and/or vibrational excited states of nitrogen and hydrogen. In this case, the description requires adopting a state-to-state kinetic approach, which considers each state as a distinct species with its own set of reactions and transport properties. Although the approach increases the complexity of the model, it is essential for accurately describing the main kinetic pathways.

Therefore, the set of heavy species in the  $N_2 - H_2$  chemical kinetics encompasses not only ground-state atoms and molecules, but also their excited states. This includes:

all of them. bla bla precursor molecules ( $N_2$ ,  $H_2$ ), atomic radicals (N, H), molecular radicals ("NH",  $NH_2$ ), various ions ( $N_2^+$ ,  $H_3^+$ ,  $NH_4^+$ ,  $H^-$ ), and electronically excited metastable species (e.g.,  $N_2(A^3\Sigma_u^+)$ ).

Key volume processes, involving electron and heavy-species collisions with these states, include **Electronic excitation, Vibrational excitation** (encopassing e-V, E-V, V-V, V-T processes, see "@anexo-

qq”), **Dissociation**, **Ionization**, **Recombination**, **Attachment**, **Detachment**, **Charge-transfer**, and other neutral-neutral and ion-neutral reactions (confirmar na quimica).

Section “@anexo-qq” presents the full list of volume and surface processes considered in chemical kinetics.

### 2.2.1 Computational Methodologies

The solution of a plasma chemistry model uses two main computational blocks: a Boltzmann equation solver to describe the electron kinetics and determine the electron transport parameters and rate coefficients, and a chemistry solver to handle the time evolution of the heavy-species densities.

The **LisbOn KInetics Chemical solver (LoKI-C)** is the counterpart to LoKI-B within the LoKI suite. It is a 0D (volume-averaged) solver that integrates the system of rate balance equations (reference equation before) for all relevant charged and neutral species in the plasma, both in the volume and on the surfaces.

Other notable 0D plasma chemistry solvers include ZDPlaskin (University of Toulouse), which provides coupled electron-heavy species kinetics with extensive reaction databases and automated cross-section interpolation for plasma chemistry.

To achieve a self-consistent solution for the plasma state, the electron kinetics and the heavy-species chemistry must be coupled, as the EEDF influences the electron-impact rates, and in turn, is influenced by the gaseous mixture composition defined by the chemical reactions.

For simulations that resolve the time evolution of the plasma, the coupling between the electron and heavy-species kinetics can be handled with different numerical schemes. Explicit coupling involves solving the EBE and the chemistry equations sequentially in time; for a given time step, the plasma state is advanced using rates from the previous time step, and then the chemistry is advanced. This approach is straightforward to implement but can suffer from numerical instability, requiring very small time steps if the system is “stiff” (i.e., contains processes with vastly different timescales). Implicit coupling, in contrast, solves the equations for the plasma and chemistry simultaneously as a single coupled system at each time step. This method is unconditionally stable and allows for much larger time steps but is significantly more complex to implement as it requires solving a large non-linear system of equations.

LoKI-B+C does not adopt a time-dependent coupling between the electron and heavy-species kinetics. Instead, it uses a strategy based on a quasi-stationary iterative, self-consistent loop:

1. **Setup:** Definition of the working conditions for the geometry of the reactor, the gas temperature and pressure, the surface site density, the wall temperature and the discharge current. (ver ficheiro inputs)
2. **Initialization:** The simulation starts with an initial guess for the gas composition (i.e., the densities of all heavy species), the electron density ,  $n_e$ , and the reduced electric field,  $E/N$ .
3. **Electron kinetics (LoKI-B):** Using the current gas composition and  $E/N$ , LoKI-B solves the EBE to compute the EEDF and the full set of electron transport parameters and rate coefficients.

4. **Heavy-species kinetics (LoKI-C):** The electron macroscopic parameters from LoKI-B are passed to LoKI-C that solves the system of rate balance equations for all heavy species, calculating their densities until steady-state.
5. **Neutrality iteration:** The values of  $n_e$  and  $E/N$  are adjusted to ensure the fixed discharge current and to satisfy the neutrality condition ( $n_e \approx \sum_i n_i$ , with  $n_i$  the number density of the ions). The process repeats from Step 3.
6. **Global iteration:** The newly calculated steady-state densities define an updated gas composition, which is fed into LoKI-B. The process repeats from Step 3. The entire loop continues until the species densities, discharge current and the reduced electric field all converge to stable, self-consistent values.

The numerical workflow employs several iterative cycles with specific convergence criteria[35]. Within LoKI-B, the solution of the EBE adopts different convergence thresholds depending on the strength of nonlinear effects. For weakly nonlinear cases (e.g., low electronegativity and ionization degree), the code uses a mixing of solutions to converge over the temporal or spatial growth parameter ( $\langle \nu_{rm\ eff} \rangle / N$  or  $\alpha_{rm\ eff} / N$ ), requiring relative differences below  $10^{-10}$  between consecutive iterations, while the EEDF convergence is set to relative variations below  $10^{-9}$  (user-prescribed via `maxEedfRelError`). When electron-electron collisions are included, a Newton-Raphson-based approach converges over the ratio  $\Theta_{ee}/\Theta_{rm\ ref}$  with relative differences below  $\sim 10^{-9} - 10^{-10}$ , and the EEDF below  $10^{-9}$ . For strongly nonlinear effects, a time-dependent relaxation method with MATLAB's `ode15s` solver is recommended, with typical parameters of relative tolerance  $\sim 10^{-6}$ , absolute tolerance  $\sim 10^{-300}$ , and maximum step-size  $\sim 10^{-7}$ .

Within LoKI-C, the *pressure cycle* ensures constant-pressure calculations by checking if  $\sum_k N_k = N$  and adjusting the gas density until relative differences in pressure fall below  $10^{-5}$  (typical value). The *neutrality cycle* couples LoKI-C and LoKI-B, adjusting  $E/N$  to satisfy the neutrality condition  $\sum_{k_p} N_{k_p} - \sum_{k_n} N_{k_n} = n_e$ , with a convergence criterion of relative neutrality values normalized to the electron density below  $10^{-8}$  (typical). Finally, the *global cycle* converges over the populations of heavy species, requiring relative variations of electron swarm parameters below  $10^{-4}$  (typical) between consecutive iterations. At steady-state convergence, the relative rate-balance for each state is typically found below  $\sim 10^{-10}$ .

## 2.3 Machine Learning in Plasma Chemistry

The detailed chemical kinetic mechanisms required for accurate plasma modeling can become computationally prohibitive, often involving thousands of reactions and dozens of species. This “curse of dimensionality” makes it impractical to include such detailed chemistry in spatially resolved (2D or 3D) reactor simulations. Machine learning (ML) has emerged as a powerful, data-driven paradigm to address this challenge by enabling the automated reduction of complex reaction schemes[].

Automated scheme’s reduction objective is to generate a minimal, or “skeletal,” kinetic model that accurately reproduces the macroscopic behavior (e.g., in present case, the densities of key species like  $NH_3$ ,  $N(^4S)$ ,  $H(^1S)$ ,  $N_2(A)$ ) of the original, full mechanism, but at a fraction of the computational

cost. Traditional reduction methods often rely on sensitivity analysis<sup>[1][2]</sup> or reaction flow analysis<sup>[3][4]</sup>, which can be laborious, since it involves an extremely high number of simulations.

Machine learning offers an alternative approach by learning the most important reaction pathways directly from data generated by the full model. Instead of relying on local sensitivity coefficients, ML models can learn a global representation of reaction importance across a wide range of plasma conditions, providing a more robust basis for model reduction.

To apply machine learning techniques to a chemical reaction network, a formal mathematical representation of the network is required. Petri nets<sup>[5]</sup> provide an intuitive and powerful framework for this purpose.

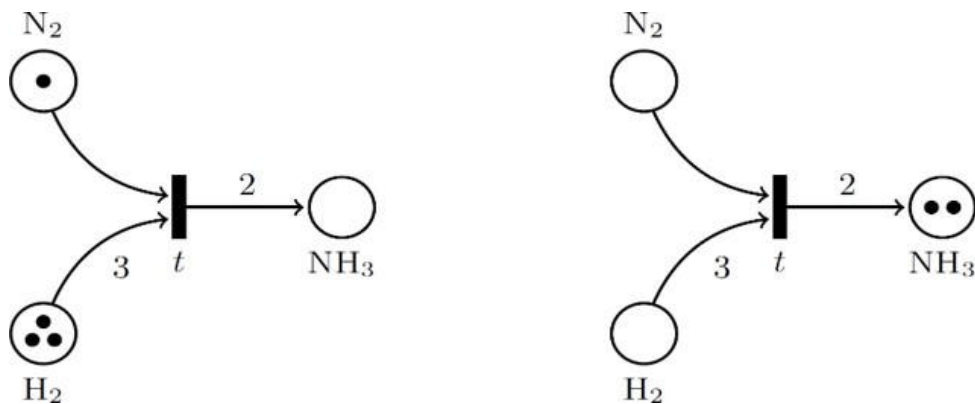


**Figure 2.1:** Example of Petri net for the reaction  $N_2 + 3H_2 \rightarrow 2NH_3$

A Petri net is a directed bipartite (confirm) graph consisting of two types of nodes<sup>[6]</sup>. Represented by circles, **places** correspond to the chemical species in the system. Figure 2.1 represents an example of a Petri net for one reaction synthesizing  $NH_3$ . Represented by thin dark rectangles, **transitions** correspond to the chemical reactions. Arcs connect places with inputs/reactants to transitions, and transitions to places with outputs/products. The numbers in these connections correspond to the stoichiometric coefficients of the reactants and products in the chemical reaction. The state of the system is defined by a “marking,” which is the number of **tokens** (“black dots”) in each place, corresponding to the concentration or number density of each species.

The structure and stoichiometry of the entire reaction network can be encoded in a single incidence matrix, often denoted as  $A$ . For a system with  $n$  species and  $m$  reactions,  $A$  is an  $n \times m$  matrix where the element  $A_{ij}$  represents the net change in the number of molecules of species  $i$  resulting from one occurrence of reaction  $j$ . Reactants have negative stoichiometric coefficients, and products have positive ones. The evolution of the vector of species concentrations,  $\vec{Y}$ , from an initial state  $\vec{Y}_0$  after a vector of reaction occurrences (or fluxes),  $\vec{x}$ , can be expressed concisely in matrix form:

$$\vec{Y}(t) = \vec{Y}_0 + A \cdot \vec{x} \quad (2.12)$$

This linear algebraic representation is well-suited for integration with machine learning (change to ML) algorithms. A machine learning framework can be designed to learn the reaction flux vector  $\vec{v}$  that best

explains the transformation from an initial species distribution to a final one, as observed in simulations. This approach will be discussed in “@chap:5” and implemented to  $N_2 - H_2$  plasmas for ammonia synthesis.

# 3

## Experimental Measurements

### Contents

---

3.1 Experimental Setup and Diagnostics .....	22
3.2 Experimental Campaign at LPP .....	27
3.3 Results and Analysis .....	29

---

By this point, a plasma was already defined, but there's still a question in the air. How can one make it?

In this chapter not only this question is answered, but it's also described exactly what parameters are measured and taken into account to support all the work of modelling presented in Section 4, and ultimately, to run simulations.

### 3.1 Experimental Setup and Diagnostics

Plasmas can be generated using two popular sources: Direct Current (DC) discharge and Radio Frequency (RF) discharge.

The **DC glow discharge** system consists usually of a cylindrical discharge tube excited by two planar electrodes positioned in a side-arm configuration, as in Figure 3.1.

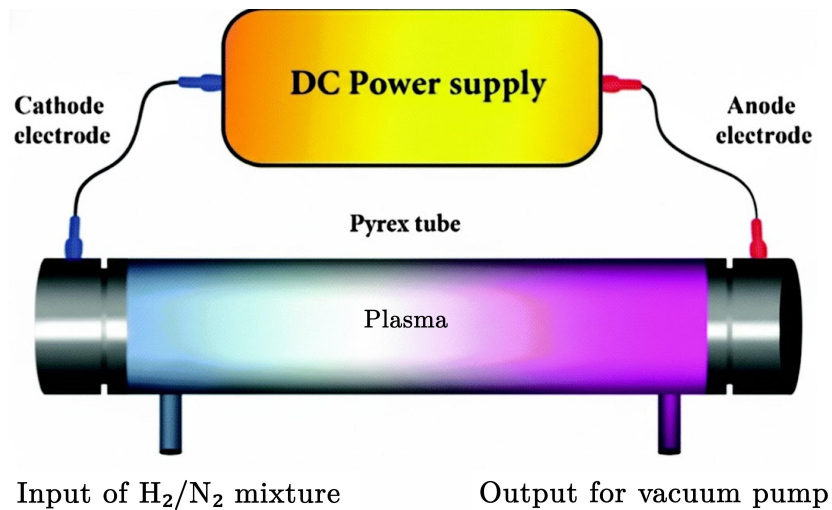


**Figure 3.1:** Simple schematic of a DC glow discharge system, adapted from [1]

This classical geometry provides a positive column region and a central, quasi-neutral plasma volume characterized by axial uniformity and relatively low electric field. The discharge is generated within a cylindrical Pyrex tube; Pyrex is selected for its excellent vacuum properties, optical transparency for diagnostic access, and well-documented surface characteristics. Two cylindrical stainless steel electrodes are positioned in perpendicular side-arms, placing them outside the direct line-of-sight for axial optical diagnostics. Gas is introduced at one end of the main tube and exhausted at the other, establishing a well-defined flow direction and residence time.

The discharge is sustained by a high-voltage DC power supply capable of delivering up to several kilovolts and tens of milliamperes. A critical component in the electrical circuit is a high-power, non-inductive ballast resistor (e.g., 150 kΩ) connected in series between the power supply and the anode. This resistor is necessary because glow discharges can exhibit negative differential resistance under certain operating conditions, where the voltage across the discharge decreases as current increases. This creates an electrically unstable situation that can lead to a runaway current increase, potentially causing the discharge to transition into an uncontrolled *arc*: a high-current, high-temperature discharge

that could damage the electrodes and equipment. The ballast resistor provides positive resistance that limits current flow and stabilizes the discharge at a controlled operating point.

A key advantage of this DC setup is the ability to directly measure the fundamental plasma parameter that governs electron kinetics: the axial electric field,  $E$ . This is accomplished via two tungsten wire probes embedded in the reactor wall and separated by a known axial distance,  $L$ [36]. By measuring the floating potential difference,  $\Delta V$ , between these probes, the axial electric field in the positive column is determined as:

$$E = \frac{\Delta V}{L} \quad (3.1)$$

The gas number density,  $N$ , is calculated using the ideal gas law:

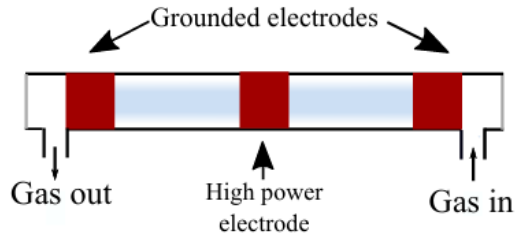
$$N = \frac{p}{k_B T_{\text{gas}}} \quad (3.2)$$

where the pressure  $p$  is measured by a capacitance manometer and the gas temperature  $T_{\text{gas}}$  is determined spectroscopically. The reduced electric field,  $E/N$ , is thus obtained directly from experimental measurements. This parameter is of paramount importance as it uniquely determines the shape of the EEDF and, consequently, the rate coefficients for all electron-impact reactions.

The plasma generated by a **RF discharge** consists of a parallel-plate configuration housed within a larger cylindrical Pyrex vacuum chamber, where the plasma is confined. A radio frequency generator powers the reactor through a *match box* (see Figure 3.2a), an intermediary device that matches the electrical impedance of the RF generator (typically  $50 \Omega$ ) to the impedance of the plasma reactor. The plasma has a complex impedance ( $Z_{\text{plasma}} = R_p + jX_p$ [37]) that doesn't match the standard  $50 \Omega$  of the generator and cables, and it also changes continuously with plasma conditions. This matching prevents power loss from reflection and ensures efficient energy delivery to the plasma. The RF power is transmitted to the plasma by a three-electrode system consisting of three copper sheets rolled around the Pyrex tube. Two grounded electrodes are located at the extremes of the reactor, and one high-power electrode is placed in the middle, as seen in Figure 3.2b. This configuration helps to control the plasma volume (confined between the two grounded electrodes) and ensures homogeneity of the discharge.



(a) Example of a Solayl customized Match box[38]



(b) Simple schematic of a RF discharge system[36]

**Figure 3.2:** RF discharge setup showing match box and electrode configuration

In both the DC and RF experimental systems, the gas flow rates are precisely regulated using digital mass flow controllers, which allow for accurate control of the total gas flow and the  $N_2 : H_2$  mixing ratio. The vacuum systems are designed to achieve a base pressure in the high-vacuum regime ( $< 10^{-6}$  mbar) prior to each experiment. This is accomplished using a two-stage pumping system, typically consisting of a turbomolecular pump backed by a dry scroll or rotary vane pump[39]. Achieving a low base pressure is critical for evacuating contaminants and the gases themselves, ensuring a clean experimental environment. The operating pressure is monitored with a temperature-independent capacitance manometer, which provides pressure readings irrespective of gas composition.

### 3.1.1 Plasma Diagnostics

A comprehensive understanding of the  $N_2$ - $H_2$  plasma chemistry necessitates a multi-faceted diagnostic approach. A suite of complementary techniques is employed to characterize the plasma's electrical properties, gas-phase composition, and internal energy distributions.

**Optical Emission Spectroscopy (OES)** is a non-invasive diagnostic that analyzes the light emitted by electronically excited species. The emission is collected via an optical fiber or lens system, dispersed by a spectrometer, and recorded by a detector[40], [41]. The resulting spectrum contains characteristic emission lines and bands that serve as fingerprints for the excited species present in the discharge. For  $N_2$ - $H_2$  plasmas, key features include the  $N_2$  Second Positive System ( $C^3\Pi_u \rightarrow B^3\Pi_g$ ), the  $N_2^+$  First Negative System ( $B^2\Sigma_u^+ \rightarrow X^2\Sigma_g^+$ ), the NH ( $A^3\Pi \rightarrow X^3\Sigma^-$ ) transition around 336 nm, and atomic hydrogen lines from the Balmer series (e.g.,  $H_\alpha$  at 656.3 nm)[42], [43]. The rotational temperature ( $T_{\text{rot}}$ ) is determined by analyzing the intensity distribution within the rotational structure of a molecular emission band. A common and reliable method involves fitting a simulated spectrum of the  $N_2$  Second Positive System (e.g., the 0-0 band at 337.1 nm) to the experimentally measured spectrum, with  $T_{\text{rot}}$  as the fitting parameter. For the low-pressure conditions investigated here, the rotational-translational relaxation is sufficiently fast to assume that the rotational temperature of the  $N_2(C^3\Pi_u)$  state is in thermal equilibrium with the kinetic temperature of the background gas, i.e.,  $T_{\text{rot}} \approx T_{\text{gas}}$ [44], [45].

**Laser-Induced Fluorescence (LIF)** is a non-invasive optical technique used for in-situ detection of specific ground-state radical species. It is the key diagnostic for measuring the absolute densities of

the highly reactive intermediates that govern the ammonia formation chemistry but are often present in concentrations too low to be detected by OES. The technique involves using a tunable laser to excite a specific **rovibronic transition** (simultaneous change in the **rotational**, **vibrational**, and **electronic** states) of the target species. The subsequent fluorescence, emitted as the excited species radiatively relaxes, is collected at a 90° angle to the laser beam. The intensity of the fluorescence signal is directly proportional to the number density of the species in the probed ground state[46]. The NH radical is typically detected by exciting the  $A^3\Pi \leftarrow X^3\Sigma^-$  electronic transition[47], [48], [49], near 336 nm band, while the  $NH_2$  radical is detected via its  $\tilde{A}^2A_1 \leftarrow \tilde{X}^2B_1$  electronic transition[50], [51], near 385 nm.

**Photofragment Translational Spectroscopy (PFTS)** explores the dynamics of gas-phase molecular photodissociation by measuring the speeds and directions of resulting fragments. A UV laser breaks a molecule apart in a molecular beam, and by measuring how fast the fragments fly apart, one can determine the energy distribution and bond dissociation energies[52]. The technique follows energy conservation:

$$E_{\text{photon}} = \text{BDE} + E_{\text{int}} + \text{TKER} \quad (3.3)$$

where the photon energy is partitioned between bond breaking (BDE), internal fragment energy, and kinetic energy release (TKER)[53]. Advanced variants include H-atom Rydberg tagging (HRA-PTS) for high-resolution measurements of hydrogen-containing molecules[53], and Velocity Map Imaging (VMI) for simultaneous 2D imaging of fragment velocity distributions[54]. These methods provide detailed information about dissociation dynamics and serve as benchmarks for theoretical models[55], [56].

**Vacuum Ultraviolet (VUV) Absorption Spectroscopy** probes high-energy electronic transitions (wavelengths < 200 nm) in molecules. VUV photons access  $\sigma \rightarrow \sigma^*$  and  $n \rightarrow \sigma^*$  transitions unavailable at longer wavelengths. Since nearly all molecules contain  $\sigma$  bonds, VUV spectroscopy is near-universal, with the notable exception of inert gases like He, Ar, and H<sub>2</sub>. The technique requires a vacuum optical path (< 10<sup>-5</sup> mbar) because atmospheric O<sub>2</sub> and water vapor strongly absorb VUV radiation. Specialized optics (MgF<sub>2</sub> or LiF windows) and detectors (PMTs, CCDs) are necessary.

VUV can provide unique “fingerprints” that can distinguish structural isomers—a critical advantage over mass spectrometry, which cannot differentiate molecules with identical mass-to-charge ratios. This makes VUV spectroscopy invaluable for gas chromatography (GC-VUV), allowing spectral deconvolution of co-eluting peaks and enabling faster analytical methods. The technique is also used for soft photoionization in reaction dynamics studies and is essential in atmospheric, combustion, and astrophysical chemistry.

**Electron Paramagnetic Resonance (EPR) Spectroscopy**, also known as Electron Spin Resonance (ESR), is uniquely sensitive to species with unpaired electrons—free radicals, transition metal complexes, and material defects. When an external magnetic field ( $B_0$ ) is applied, electron spin states split (Zeeman effect), and microwave radiation at the resonant frequency induces transitions between these states:

$$\Delta E = h\nu = g\mu_B B_0 \quad (3.4)$$

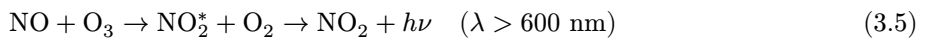
where the g-factor ( $g \approx 2.0023$  for free electrons) is sensitive to the electronic environment, serving as a “fingerprint” for paramagnetic species. Hyperfine coupling with nearby nuclei splits the signal into multiple lines, with  $2NI + 1$  lines for  $N$  equivalent nuclei of spin  $I$ , providing structural information about bonding and distances.

EPR spectrometers use microwave sources (9.5 GHz for X-band), resonant cavities, and swept magnetic fields to record spectra, typically displayed as first derivatives. Applications include studying reaction kinetics, catalysis, metalloproteins, reactive oxygen species, and material defects. Spin trapping and spin labeling techniques extend EPR to short-lived radicals and diamagnetic molecules, respectively.

**Gas-Phase Chemiluminescence Titration** exploits light emission from rapid stoichiometric reactions for highly sensitive species quantification. Chemiluminescence produces signals against a dark background, achieving detection limits of parts-per-billion to parts-per-trillion—far superior to absorption spectroscopy.

Two key applications illustrate the technique:

**NO + O<sub>3</sub> Titration** measures ozone and calibrates NOx analyzers via:



For ozone measurement, excess NO is added, and light intensity is proportional to [O<sub>3</sub>]. For NOx calibration (Gas Phase Titration), a known [NO]<sub>orig</sub> reacts with O<sub>3</sub> to produce NO<sub>2</sub>, where [NO<sub>2</sub>]<sub>produced</sub> = [NO]<sub>orig</sub> − [NO]<sub>rem</sub>. This provides traceable NO<sub>2</sub> standards from stable NO sources, fundamental to air quality monitoring.

**N+NO Titration** measures atomic nitrogen via two sequential reactions:



NO is gradually added to the N-atom stream. At the endpoint ([NO] = [N]), all N atoms are consumed. Excess NO then produces the characteristic greenish-white “air afterglow” from the second reaction, allowing absolute determination of [N].

**Fourier-Transform Infrared (FTIR) Spectroscopy** identifies molecules by probing quantized vibrational modes (stretching and bending). IR absorption occurs when photons match vibrational energy differences and cause dipole moment changes. Homonuclear diatomics like N<sub>2</sub> and O<sub>2</sub> are IR-inactive. The resulting spectrum (cm<sup>-1</sup> vs. absorbance) provides unique molecular “fingerprints.”

FTIR uses a Michelson interferometer: a moving mirror creates an interferogram (time-domain signal containing all IR frequencies), which is Fourier-transformed to produce the frequency-domain spectrum. This offers Fellgett’s Advantage (simultaneous measurement of all frequencies, faster acquisition) and Jacquinot’s Advantage (no restrictive slits, higher signal-to-noise).

The spectrum divides into two regions: the functional group region ( $4000\text{-}1500\text{ cm}^{-1}$ ) identifies specific bonds (e.g., O-H at  $3300\text{ cm}^{-1}$ , C=O at  $1700\text{ cm}^{-1}$ ), while the fingerprint region ( $1500\text{-}400\text{ cm}^{-1}$ ) provides unique molecular identification. Attenuated Total Reflectance (ATR) sampling requires minimal preparation and is ideal for opaque or thick samples. FTIR is complementary to Raman spectroscopy due to different selection rules (dipole moment change vs. polarizability change).

**Optical Thermometry** measures surface temperature via non-contact optical methods, overcoming thermocouple limitations (contact requirement, EMI susceptibility, invasiveness). Light-based measurements are immune to electromagnetic interference.

**Thermographic phosphors** are coated on surfaces and excited by UV light. Temperature is determined from luminescence decay time ( $\tau$  decreases with temperature) or intensity ratios at two wavelengths. This enables 2D thermal imaging and is insensitive to surface emissivity.

**Thermochromic Liquid Crystals (TLCs)** selectively reflect wavelengths based on temperature, creating color maps via calibrated cameras. Range is limited (0-120°C).

**Fiber-optic sensors** include GaAs semiconductor probes (temperature-dependent band gap absorption edge, EMI-immune) and blackbody radiation sensors for high temperatures (up to 2000°C with sapphire fibers). Ratiometric measurements (intensity ratios at two wavelengths) make sensors robust against signal fluctuations, encoding temperature in spectral shape rather than absolute intensity.

### 3.1.1.1 Electrical Probes

Invasive electrical probes are used to determine local, fundamental plasma parameters with high spatial resolution.

**Langmuir Probes:** A Langmuir probe consists of a small metallic electrode inserted into the plasma. A variable bias voltage is applied to the probe, and the collected current is measured, yielding a characteristic current-voltage (I-V) curve. Analysis of this curve provides local values for the electron density ( $n_e$ ), electron temperature ( $T_e$ ), and the full Electron Energy Distribution Function (EEDF). These parameters are essential inputs for kinetic models, as they directly determine the rates of all electron-impact reactions. In RF plasmas, the plasma potential oscillates at the driving frequency and its harmonics. To obtain an unperturbed I-V characteristic, the probe circuit must be designed to follow these oscillations, a technique known as RF compensation.

## 3.2 Experimental Campaign at LPP

### 3.2.1 Campaign objectives and methodology

The experimental campaign at LPP (Laboratoire de Physique des Plasmas) was designed with specific objectives:

#### Primary objectives:

- Validate the kinetic model under controlled conditions
- Measure key species concentrations for model comparison

- Characterize discharge behavior across parameter space
- Identify model limitations and improvement areas

**Secondary objectives:**

- Compare with literature data
- Test diagnostic techniques
- Establish measurement protocols
- Generate benchmark data for the community

The methodology included:

- Systematic parameter variation
- Multiple measurements for statistical significance
- Cross-validation between different diagnostics
- Detailed documentation of experimental procedures

### 3.2.2 Measurement protocols and procedures

Standardized measurement protocols were developed to ensure reproducibility:

**Gas handling procedures:** Purification, mixing, flow control **Discharge startup:** Gradual voltage increase, stabilization time **Diagnostic timing:** Synchronization of different measurements **Data acquisition:** Automated data collection and storage

The protocols included:

- Pre-measurement calibration procedures
- During-measurement monitoring
- Post-measurement data validation
- Quality control checks

### 3.2.3 Data acquisition and processing

Data acquisition and processing were automated to ensure consistency:

**Real-time monitoring:** Continuous monitoring of key parameters **Automated data collection:** Computer-controlled data acquisition **Data validation:** Real-time checks for data quality **Post-processing:** Automated data analysis and plotting

The data processing included:

- Signal filtering and noise reduction
- Calibration and background subtraction
- Uncertainty estimation
- Format standardization for model comparison

### 3.2.4 Reproducibility assessment

Reproducibility was assessed through:

**Repeated measurements:** Multiple measurements under identical conditions **Operator variation:**

Measurements by different operators **Time stability:** Measurements over extended time periods **Cross-validation:**

Comparison between different diagnostic techniques

The reproducibility assessment included:

- Statistical analysis of repeated measurements
- Uncertainty estimation from reproducibility data
- Identification of systematic errors
- Development of improved procedures

## 3.3 Results and Analysis

### 3.3.1 Gas and Wall Temperatures

The gas and wall temperatures were systematically measured across different operating conditions:

**Temperature measurements:** Gas temperature was measured using spectroscopic techniques, while wall temperature was monitored using thermocouples and infrared cameras.

**Parameter dependencies:** Temperature showed strong dependencies on:

- Discharge power density
- Gas pressure and composition
- Flow rates and residence time
- Wall material and cooling

**Temperature profiles:** Both spatial and temporal temperature profiles were characterized to understand heat transfer mechanisms and optimize operating conditions.

### 3.3.2 $[\text{NH}_3]$ vs Temperature Analysis

To illustrate the relationship between ammonia concentration and temperature, several representative data points were selected from the experimental campaign:

**Low temperature regime (300-400 K):**

- $[\text{NH}_3]$  typically 0.1-0.5% of total gas composition
- Limited by slow reaction kinetics
- Strong dependence on residence time

**Medium temperature regime (400-600 K):**

- $[\text{NH}_3]$  increases to 1-3% of total gas composition
- Optimal conditions for ammonia synthesis
- Balance between production and decomposition

### **High temperature regime (600-800 K):**

- $[\text{NH}_3]$  decreases due to thermal decomposition
- Competing reactions become dominant
- Energy efficiency considerations

The temperature dependence analysis revealed optimal operating conditions and provided insights into the underlying reaction mechanisms.

### **3.3.3 Discharge characteristics (E/N vs NR)**

The discharge characteristics were analyzed in terms of:

**Current-voltage characteristics:** Relationship between discharge current and voltage  
**Power dissipation:** Electrical power consumed by the discharge  
**Discharge stability:** Temporal and spatial stability of the discharge  
**Parameter dependencies:** Effect of pressure, gas composition, and gap distance

Key findings included:

- Discharge stability over wide parameter ranges
- Power efficiency optimization opportunities
- Parameter regions for optimal ammonia production
- Comparison with literature data

### **3.3.4 Species density profiles**

Species density profiles were measured and compared with model predictions:

**Neutral species:**  $\text{N}_2$ ,  $\text{H}_2$ ,  $\text{NH}_3$ ,  $\text{N}$ ,  $\text{H}$ ,  $\text{NH}$ ,  $\text{NH}_2$  **Excited species:**  $\text{N}_2^*$ ,  $\text{H}_2^*$ ,  $\text{NH}^*$  **Ionic species:**  $\text{N}_2^+$ ,  $\text{H}_2^+$ ,  $\text{NH}_3^+$

The analysis included:

- Spatial profiles across the discharge gap
- Temporal evolution of species concentrations
- Parameter dependencies (E/N, pressure, composition)
- Comparison with model predictions

### **3.3.5 Spectra from LPP Laboratory**

During the experimental campaign at LPP, several spectroscopic measurements were performed to characterize the plasma:

**Optical emission spectra:** High-resolution spectra were recorded in the 200-800 nm range, revealing:

- $\text{N}_2$  molecular bands ( $B^3\Pi_g \rightarrow A^3\Sigma_u^+$ ,  $C^3\Pi_u \rightarrow B^3\Pi_g$ )
- $\text{H}_2$  molecular bands (Fulcher- $\alpha$ , Lyman- $\alpha$ )
- $\text{NH}$  molecular bands ( $A^3\Pi \rightarrow X^3\Sigma^-$ )
- Atomic lines ( $H_\alpha$ ,  $H_\beta$ , N lines)

**Spatial resolution:** Spectra were recorded at different positions across the discharge gap to understand spatial variations in excited state populations.

**Temporal evolution:** Time-resolved measurements captured transient phenomena and discharge stability characteristics.

**Parameter studies:** Spectra were recorded across different operating conditions to understand the dependence of excited state populations on discharge parameters.

The spectroscopic data provided valuable insights into:

- Electron energy distribution function characteristics
- Excited state chemistry and energy transfer processes
- Discharge uniformity and stability
- Validation of theoretical models

### 3.3.6 Ammonia production rates

Ammonia production rates were measured and analyzed:

**Production efficiency:** NH<sub>3</sub> production per unit energy input **Parameter optimization:** Conditions for maximum ammonia production **Mechanism analysis:** Identification of key reaction pathways **Comparison with literature:** Validation against published data

The analysis revealed:

- Optimal conditions for ammonia production
- Key reaction pathways for ammonia formation
- Energy efficiency considerations
- Scaling considerations for industrial applications

### 3.3.7 Model validation and refinement needs

The experimental results were used to validate and refine the kinetic model:

**Model performance assessment:** Quantitative comparison with experimental data **Parameter sensitivity analysis:** Identification of key model parameters **Mechanism refinement:** Addition or modification of reactions **Uncertainty reduction:** Improved rate coefficient estimates

The validation process identified:

- Areas of good agreement between model and experiment
- Systematic discrepancies requiring model refinement
- Missing reaction pathways
- Improved rate coefficient estimates

The refinement process included:

- Addition of missing reactions
- Adjustment of rate coefficients
- Improved cross-section data

- Enhanced surface reaction models

# 4

## Modelling of $N_2 - H_2$ Plasmas

### Contents

---

4.1 Chemical Model Development .....	34
4.2 Validation of the Chemical Model .....	48

---

While experimental diagnostics provide invaluable macroscopic data on species concentrations and electrical parameters, a microscopic description is required to deepen the understanding of  $N_2 - H_2$  plasmas across the vast range of working conditions. This is the domain of plasma modeling, a powerful method that simulates the complex interplay of hundreds of chemical reactions occurring over disparate timescales.

As introduced in the Section 2 review, a plasma chemical model can be described by a large system of coupled differential equations to calculate the particle densities of every species in the plasma. The predictive power of such a model is not determined by the sophistication of the numerical solver, but by the quality of the physical and chemical data it is fed. At the heart of these data lies the chemical scheme: a comprehensive collection of all relevant reactions and their corresponding rate coefficients. The model's accuracy is directly and exquisitely sensitive to the values of the rate coefficients. An error or uncertainty in the rate coefficient for a single reaction can cascade through the entire simulation, leading to modelling predictions that deviate considerably from experimental measurements. For a complex network like the  $N_2 - H_2$  system, where the target molecule ( $NH_3$ ) is the result of a long and competing chain of volume and surface reactions, the challenge is amplified. The final predicted  $NH_3$  concentration is a product of dozens of preceding steps, and its accuracy is only as strong as the weakest link in that kinetic chain.

Therefore, compiling a chemical kinetic database is not a simple act of data collection. It is a critical research step involving an extensive and systematic review of published literature to identify not only the relevant reactions but also the various, often conflicting, rate coefficients proposed for them.

For several crucial reactions, a comparison of different literature sources shows rate coefficients that can differ by a factor of ten or more at similar electron temperatures or gas temperatures. This is not a minor numerical discrepancy; it represents a fundamental disagreement on the importance of a given reaction pathway.

This discovery shaped the entire modeling strategy of the project team, this thesis in particular. It became clear that simply selecting one kinetic set from a single publication would be arbitrary and scientifically unsound. It was necessary to treat the choice of the chemical scheme as a variable to be investigated. To this end, a comprehensive database was created, cataloging multiple proposed rate coefficients for each key reaction, each based on the data from a different literature source or a combination thereof.

## 4.1 Chemical Model Development

The development of the chemical model was based essentially on the chemical scheme of Redondo *et al.* @redondo complemented with the mesoscopic surface model of Gordiets *et al.* @gordiets. In this work, this chemical scheme was updated to include information from the the work of Capitelli *et al.* [57], NIST Chemical Kinetics Database [58], and recent publication by Bang *et al.* [59]. Tables @table-k-plus and @table-k-minus summarize the rate coefficients data from these sources for direct and reverse reactions, respectively. For comparison, the tables show also data used by the PSI.COM project

@psi\_com. Whenever available, formula are specified, and in these cases the values are calculations at the reference temperature of 300 K.

The reactions and rate coefficients were harmonized to the Arrhenius form  $k = A(\frac{T}{300})^n \exp(-\frac{E_a}{T})$ , with units converted to  $m^3 s^{-1}$  and  $m^6 s^{-1}$ , for two-body and three-body processes, respectively. The tables do not specify the state configuration of its species since this information was absent in Capitelli *et al.* [57]. The table show disparate values for the rate coefficients proposed by the different sources. In particular, the values by Bang *et al.* [59] are often very different by several orders of magnitude, probably due to sign errors in the exponential factor. For this reason, preference was given to the expressions proposed by Capitelli *et al.* using NIST for cross-checking. Regarding NIST data, theoretical values were only used when experimental data were unavailable. Note that Capitelli's data were derived at atmospheric pressure and high gas temperatures, typically above 1000 K. Therefore, the values of  $A$  and  $E_a$  in Capitelli's expressions were adjusted in some cases. After the assessment of the data showed in the tables, a final set of rate coefficients was selected, marked as green cells. In cases of strong disagreement between the values of rate coefficients from different sources, a range of uncertainty was put on record (see Appendix) for future use in uncertainty analysis.

**Table 4.1:** Forward rate coefficients for  $N_2$ -H<sub>2</sub> chemistry.

Reaction	Capitelli (formula)	PSI.COM	Bang	NIST
$N_2H_4 + H \leftrightarrow$	$2.10e -$			
$N_2H_3 + H_2$	$17 \exp(-\frac{1260.0}{T})$			
For T=300K	$3.15e - 19$	$1.2e -$ $17 \exp(-\frac{1260}{T_g})$	$4.58e -$ $27T_g^{2.56} \exp(\frac{614.1}{T_g})$	$1.59e - 19$
$N_2H_4 + H \leftrightarrow$	$1.90e -$			
$N_2H_2 + NH_3$	$21 \exp(-\frac{1560.0}{T})$			
For T=300K	$1.05e - 23$	—	—	—
$N_2H_3 + H \leftrightarrow$	$1.70e -$			
$N_2H_2 + H_2$	$18 \exp(-\frac{1000.0}{T})$			
For T=300K	$6.06e - 20$	—	$2.69e - 16$	—
$N_2H_3 + H \leftrightarrow$	$2.60e - 18$			
$2NH_2$				
For T=300K	$2.60e - 18$	—	—	$2.01e - 17$
$N_2H_3 + H \leftrightarrow$	$1.70e - 19$			
$NH + NH_3$				
For T=300K	$1.70e - 19$	—	$1.66e - 19$	—
$N_2H_2 + H \leftrightarrow$	$1.70e -$			
$N_2H + H_2$	$17 \exp(-\frac{500.0}{T})$			
For T=300K	$3.21e - 18$	—	$6.33e - 17$	$5.2e - 18$
$N_2H + H \leftrightarrow N_2 +$	$6.60e -$			
$H_2$	$17 \exp(-\frac{1500.0}{T})$			
For T=300K	$4.45e - 19$	—	$1.66e - 16$	$1.66e - 18$

$NH_3 + H \leftrightarrow$	$2.10e -$			
$NH_2 + H_2$	$17 \exp\left(-\frac{10820.0}{T}\right)$			
For T=300K	$4.56e - 33$	$8.4e - 20 \left(\frac{T_g}{300}\right)^{4.1} \exp\left(-\frac{4760}{T_g}\right)$	$6.08e - 11$	$4.71e - 26$
$NH_2 + H \leftrightarrow NH + H_2$	$3.20e - 17$			
For T=300K	$3.20e - 17$	$1.43e - 19$	$1.80e - 19$	$1e - 17$
$NH + H \leftrightarrow N + H_2$	$8.30e -$			
	$16 \exp\left(-\frac{1000.0}{T}\right)$			
For T=300K	$2.96e - 17$	$3.12e - 17$	$7.50e - 17$	$1.69e - 17$
$N_2H_4 + NH \leftrightarrow$	$2.90e - 17 \left(\frac{T}{300}\right)^{0.5} \exp\left(-\frac{1000.0}{T}\right)$			
$NH_2 + N_2H_3$				
For T=300K	$1.03e - 18$	-	$4.67e - 17$	$5.21e - 24$
$N_2H_2 + NH \leftrightarrow$	$1.70e -$			
$N_2H + NH_2$	$17 \exp\left(-\frac{500.0}{T}\right)$			
For T=300K	$3.21e - 18$	-	$4.86e - 20$	-
$N_2H + NH \leftrightarrow$	$5.80e - 18 \left(\frac{T}{300}\right)^{0.5} \exp\left(-\frac{1000.0}{T}\right)$			
$N_2 + NH_2$				
For T=300K	$2.07e - 19$	-	$8.3e - 17$	-
$NH + NH \leftrightarrow$	$5.80e - 18 \left(\frac{T}{300}\right)^{0.5} \exp\left(-\frac{1000.0}{T}\right)$			
$NH_2 + N$				
For T=300K	$2.07e - 19$	$1.70e - 18$	$6.86e - 21$	$2.16e - 21$
$NH + NH \leftrightarrow$	$2.30e - 17 \left(\frac{T}{300}\right)^{0.5} \exp\left(-\frac{500.0}{T}\right)$			
$N_2H + H$				
For T=300K	$4.34e - 18$	-	-	-
$N_2H_4 + NH_2 \leftrightarrow$	$1.10e - 17 \left(\frac{T}{300}\right)^{0.5} \exp\left(-\frac{1000.0}{T}\right)$			
$N_2H_3 + NH_3$				
For T=300K	$3.92e - 19$	$5.20e - 19$	$8.15e - 17$	$5.15e - 19$
$N_2H_3 + NH_2 \leftrightarrow$	$2.90e - 18 \left(\frac{T}{300}\right)^{0.5}$			
$N_2H_2 + NH_3$				
For T=300K	$2.90e - 18$	-	$5.31e - 21$	$8.63e - 19$
$N_2H_2 + NH_2 \leftrightarrow$	$1.70e -$			
$N_2H + NH_3$	$18 \exp\left(-\frac{2000.0}{T}\right)$			
For T=300K	$2.16e - 21$	0	$2.61e - 20$	$1.06e - 22$
$N_2H_2 + NH_2 \leftrightarrow$	$2.90e - 18 \left(\frac{T}{300}\right)^{0.5} \exp\left(-\frac{17000.0}{T}\right)$			
$NH + N_2H_3$				
For T=300K	$7.12e - 43$	-	-	-
$N_2H + NH_2 \leftrightarrow$	$1.70e - 17$			
$N_2 + NH_3$				
For T=300K	$1.70e - 17$	-	$2.87e - 10$	-

$NH_3 + NH_2 \leftrightarrow N_2H_3 + H_2$	$2.30e - 17 \left(\frac{T}{300}\right)^{0.5} \exp\left(-\frac{10850.0}{T}\right)$			
For T=300K	$4.52e - 33$	-	$0.017$	-
$NH_2 + NH_2 \leftrightarrow NH + NH_3$	$1.00e - 17 \exp\left(-\frac{5000.0}{T}\right)$			
For T=300K	$5.78e - 25$	$1.99e - 21$	$1.31e - 20$	$< 3.32e - 21$
$NH_2 + NH_2 \leftrightarrow N_2H_2 + H_2$	$6.60e - 17 \exp\left(-\frac{6000.0}{T}\right)$			
For T=300K	$1.36e - 25$	$1.3e - 18$	$2.86e - 05$	$1.3e - 18$
$NH_2 + NH \leftrightarrow N_2H_2 + H$	$5.20e - 17 \exp\left(-\frac{500.0}{T}\right)$			
For T=300K	$9.82e - 18$	$2.5e - 15$	$4.02e - 17$	$2.11e - 27$
$N_2H_4 + N_2H_2 \leftrightarrow 2N_2H_3$	$7.20e - 17 \left(\frac{T}{300}\right)^{0.5} \exp\left(-\frac{15000.0}{T}\right)$			
For T=300K	$1.39e - 38$	-	3727	-
$N_2H_3 + N_2H_2 \leftrightarrow N_2H_4 + N_2H$	$1.70e - 17 \exp\left(-\frac{5000.0}{T}\right)$			
For T=300K	$9.82e - 25$	-	$2.90e - 10$	-
$N_2H_2 + N_2H_2 \leftrightarrow N_2H + N_2H_3$	$1.70e - 17 \exp\left(-\frac{5000.0}{T}\right)$			
For T=300K	$9.82e - 25$	-	$2.90e - 10$	-
$N_2H + N_2H \leftrightarrow N_2H_2 + N_2$	$1.70e - 17 \exp\left(-\frac{5000.0}{T}\right)$	For T=300K	$9.82e - 25$	-
$2.90e - 10$	-	$NH + N \leftrightarrow N_2 + H$	$1.80e - 17 \left(\frac{T}{300}\right)^{0.5}$	
		For T=300K	$1.80e - 17$	$5.00e - 17$
$4.98e - 17$	$1.90e - 17$	$N_2H + N \leftrightarrow NH + N_2$	$5.20e - 17 \exp\left(-\frac{1000.0}{T}\right)$	
		For T=300K	$1.86e - 18$	-
-	-	$N_2(A) + NH_3 \rightarrow N_2(X) + H + NH_2$	-	
		For T=300K	$8.50e - 17$	$1.6e - 16$
-	$1.20e - 16$	$N_2(A) + H \rightarrow N_2(X, v = 25) + H$	-	
		For T=300K	$2.10e - 16$	$5.00e - 17$
-	$2.10e - 16$	$N_2(A) + H_2 \rightarrow N_2(X) + 2H$	-	
		For T=300K	$1.71e - 21$	$1.71e - 21$
-	-	$N(2D) + H_2 \rightarrow NH + H$	-	

		For T=300K	$2.30e - 18$	$2.30e - 18$
$2.30e - 18$	$2.19e - 18$			

**Table 4.2:** Reverse rate coefficients for N<sub>2</sub>-H<sub>2</sub> chemistry.

Reaction	Capitelli (formula)	PSI.COM	Bang	NIST
$N_2H_4 + H \leftrightarrow N_2H_3 + H_2$	–			
For T=300K	–	–	–	–
$N_2H_4 + H \leftrightarrow N_2H_2 + NH_3$	–			
For T=300K	–	–	–	–
$N_2H_3 + H \leftrightarrow N_2H_2 + H_2$	–			
For T=300K	–	–	–	–
$N_2H_3 + H \leftrightarrow 2NH_2$	–			
For T=300K	–	–	–	$< 1e - 19$
$N_2H_3 + H \leftrightarrow NH + NH_3$	–			
For T=300K	–	–	–	–
$N_2H_2 + H \leftrightarrow N_2H + H_2$	$1.90e - 19\left(\frac{T}{300}\right)^{0.5} \exp\left(-\frac{23184.0}{T}\right)$			
For T=300K	$5.21e - 53$	–	–	–
$N_2H + H \leftrightarrow N_2 + H_2$	$7.10e - 16 \exp\left(-\frac{56950.0}{T}\right)$			
For T=300K	$2.56e - 98$	–	–	–
$NH_3 + H \leftrightarrow NH_2 + H_2$	$2.10e - 17\left(\frac{T}{300}\right)^{0.5} \exp\left(-\frac{9274.0}{T}\right)$			
For T=300K	$7.88e - 31$	$2.16e - 26$	–	$3.05e - 24$
$NH_2 + H \leftrightarrow NH + H_2$	$2.20e - 17 \exp\left(-\frac{3880.0}{T}\right)$			
For T=300K	$5.32e - 23$	–	–	$2.06e - 28$
$NH + H \leftrightarrow N + H_2$	$3.90e - 16 \exp\left(-\frac{15775.0}{T}\right)$			
For T=300K	$5.68e - 39$	$1.50e - 34$	$2.50e - 20$	$4.37e - 40$
$N_2H_4 + NH \leftrightarrow NH_2 + N_2H_3$	–			
For T=300K	–	–	–	–
$N_2H_2 + NH \leftrightarrow N_2H + NH_2$	–			
For T=300K	–	–	–	–
$N_2H + NH \leftrightarrow N_2 + NH_2$	$8.50e - 17\left(\frac{T}{300}\right)^{0.5} \exp\left(-\frac{52920.0}{T}\right)$			
For T=300K	$2.09e - 93$	–	–	–
$NH + NH \leftrightarrow NH_2 + N$	$4.00e - 17\left(\frac{T}{300}\right)^{0.5} \exp\left(-\frac{11890.0}{T}\right)$			
For T=300K	$2.45e - 34$	–	–	$2.96e - 30$
$NH + NH \leftrightarrow N_2H + H$	$2.90e - 16\left(\frac{T}{300}\right)^{0.5} \exp\left(-\frac{43240.0}{T}\right)$			
For T=300K	$7.35e - 79$	–	–	–

$N_2H_4 + NH_2 \leftrightarrow N_2H_3 + NH_3$	-			
For T=300K	-	-	-	-
$N_2H_3 + NH_2 \leftrightarrow N_2H_2 + NH_3$	-			
For T=300K	-	-	-	-
$N_2H_2 + NH_2 \leftrightarrow N_2H + NH_3$	-			
For T=300K	-	-	-	-
$N_2H_2 + NH_2 \leftrightarrow NH + N_2H_3$	-			
For T=300K	-	$3.32e - 17$	-	-
$N_2H + NH_2 \leftrightarrow N_2 + NH_3$	$1.70e - 15 \exp\left(-\frac{57960.0}{T}\right)$			
For T=300K	$2.11e - 99$	-	-	-
$NH_3 + NH_2 \leftrightarrow N_2H_3 + H_2$	-			
For T=300K	-	-	-	-
$NH_2 + NH_2 \leftrightarrow NH + NH_3$	$7.40e - 17 \exp\left(-\frac{15470.0}{T}\right)$			
For T=300K	$2.98e - 39$	-	-	$1.66e - 35$
$NH_2 + NH_2 \leftrightarrow N_2H_2 + H_2$	$6.20e - 15 \exp\left(-\frac{25910.0}{T}\right)$			
For T=300K	$1.92e - 52$	-	-	-
$NH_2 + NH \leftrightarrow N_2H_2 + H$	$6.80e - 15 \exp\left(-\frac{11995.0}{T}\right)$			
For T=300K	$2.94e - 32$	-	-	-
$N_2H_4 + N_2H_2 \leftrightarrow 2N_2H_3$	-			
For T=300K	-	$2.00e - 17$	-	$3.7e - 06$
$N_2H_3 + N_2H_2 \leftrightarrow N_2H_4 + NH$	-			
For T=300K	-	-	-	-
$N_2H_2 + N_2H_2 \leftrightarrow N_2H + N_2H_3$	-			
For T=300K	-	-	-	-
$N_2H + N_2H \leftrightarrow N_2H_2 + N_2$	$8.30e - 17 \exp\left(-\frac{33260.0}{T}\right)$			
For T=300K	$5.89e - 65$	-	-	-
$NH + N \leftrightarrow N_2 + H$	$4.70e - 16 \left(\frac{T}{300}\right)^{0.5} \exp\left(-\frac{75900.0}{T}\right)$			
For T=300K	$6.25e - 126$	-	-	$8.87e - 124$
$N_2H + N \leftrightarrow NH + N_2$	$1.20e - 16 \exp\left(-\frac{41830.0}{T}\right)$			
For T=300K	$3.34e - 71$	-	-	-

Note: k follows  $k = A (T/300)^n \exp(-E_a/T)$ ; units in  $m^3 s^{-1}$  (bimolecular) and  $m^6 s^{-1}$  (termolecular). k- from detailed balance when missing. (+M) denotes third-body processes. "Calculated" values at 300 K unless stated; "psi.com" are the implemented coefficients. Capitelli fits often target higher-T regimes ( $>1000$  K); form retained with noted validity limits. Bang used mainly as comparator. Uncertainty = envelope

between sources (e.g., NIST vs Capitelli). NIST experimental values preferred; theory used only when no experiment exists.

The rate coefficients selected in tables 1 and 2 were used to update and complete the original chemical scheme, as shown in [tabl .chem anexo], extending it to use in future atmospheric pressure studies.

#### 4.1.1 Mesoscopic Surface Model

In the study of reactive plasmas, particularly those involving nitrogen-hydrogen mixtures for applications like ammonia synthesis, the interaction between the plasma and the reactor surfaces is of paramount importance. The surface is not merely a passive boundary for particle loss; it is an active chemical environment where crucial reaction pathways occur. The modeling of these interactions has evolved from using simplified macroscopic parameters to employing detailed mesoscopic kinetic models, which provide a more fundamental and predictive understanding of the plasma chemistry.[references prof Vasco papers and restore gamma][60]

Mesoscopic kinetic models treat the surface as a dynamic system with its own set of species, sites, and elementary reactions. This work is inspired by the mesoscopic model proposed by Gordiets *et al.* [60], according to which the synthesis of ammonia ( $NH_3$ ) predominantly occurs on the surface, which acts as a catalyst. The foundations of this model rely on distinguishing between the following components: **physisorption surface vacant sites** ( $F(v)$ ), where gas-phase particles are weakly and movably bound by van der Waals forces, and **chemisorption surface vacant sites** ( $S(v)$ ), where particles can form strong, immobilizing chemical bonds; **gas-phase atoms** ( $N, H$ ) and **radicals** ( $NH, NH_2$ ) formed in the plasma volume, which act as fundamental building blocks that initiate the surface chemistry, via either **physisorbed surface states** (e.g.,  $N(F)$ ) or **chemisorbed surface states** (e.g.,  $N(S)$ ).

The entire lifecycle of a particle on the surface is described by a set of elementary reactions. The initial step involves **adsorption**, where a gas-phase atom weakly binds to a physisorption site (e.g.,  $N(^4S) + F(v) \rightarrow N(F)$ ), or strongly binds to a chemisorption site (e.g.,  $N(^4S) + S(v) \rightarrow N(S)$ ). A mobile physisorbed atom can also transition to a chemisorbed state ( $N(F) + S(v) \rightarrow N(S) + F(v)$ ). The reverse process, **thermal desorption**, occurs when adsorbed particles gain enough thermal energy to break their bonds and return to the gas phase (e.g.,  $N(F) \rightarrow N(^4S) + F(v)$ ), and is naturally favoured when involving physisorbed species.

Subsequently, a series of surface reactions builds  $NH_x$  radicals, with  $x = 1, 2$ , through sequential hydrogenation reactions. First, an adsorbed nitrogen atom reacts with a gas-phase hydrogen atom to form an adsorbed NH radical ( $H(^1S) + N(S) \rightarrow NH(S)$ ), which is then further hydrogenated to form  $NH_2(S)$  ( $H(^1S) + NH(S) \rightarrow NH_2(S)$ ) [fix]. The final step is the formation and desorption of ammonia into the gas phase, via two primary recombination mechanisms. In the **Eley-Rideal (ER) mechanism**, a gas-phase hydrogen atom directly strikes and reacts with a chemisorbed species



arrowN H<sub>3</sub>(X) + S(v) alternatively, in the **Langmuir-Hinshelwood (LH) mechanism**, a physisorbed species diffuses across the surface to encounter a chemisorbed species and react H(F) + NH<sub>2</sub>(S) → NH<sub>3</sub> + S(v) + F(v)[to be confirmed].

A key strength of the mesoscopic model is its ability to self-consistently determine the macroscopic  $\gamma$ -coefficients instead of treating them as input parameters. As shown in [60], even in the case of the complex N<sub>2</sub>-H<sub>2</sub> surface chemistry, the recombination coefficients  $\gamma_N$  and  $\gamma_H$  can be calculated from the frequencies of the elementary surface reactions and the fractional surface coverages of adsorbed species. This bridges the two approaches, allowing for a more robust and physically grounded plasma model where the surface response is a calculated output, not an assumption.

The complete set of surface reactions implemented in the model is shown below:

**Surface 4.1:** Mesoscopic surface model reactions for N<sub>2</sub>-H<sub>2</sub> system - Part 1: Core reactions (Gordiets et al. 1998)

```
% Mesoscopic surface model for N2-H2 (inspired in Gordiets et al 1998)
% Adsorption and desorption of N and H atoms
N(4S) + wall_F(v) -> wall_N(F) | thermalEffusionSurface |
1, 0, gasTemperature
wall_N(F) -> N(4S) + wall_F(v) | thermalDesorption |
1e15, 51e3
H(1S) + wall_F(v) -> wall_H(F) | thermalEffusionSurface |
1, 0, gasTemperature
wall_H(F) -> H(1S) + wall_F(v) | thermalDesorption |
1e15, 37e3

% Nitrogen surface chemistry
N(4S) + wall_S(v) -> wall_N(S) | thermalEffusionSurface |
1, 0, gasTemperature
wall_N(F) + wall_S(v) -> wall_N(S) + wall_F(v) | surfaceTransport |
1e13, 0.5*51e3, 1, 0, true
N(4S) + wall_N(S) -> N2(X,v=0) + wall_S(v) | thermalEffusionSurface |
1, 11.2e3, gasTemperature
wall_N(F) + wall_N(S) -> N2(X,v=0) + wall_S(v) + wall_F(v) | surfaceTransport |
1e13, 0.5*51e3, 1, 25.5e3, false

% Hydrogen surface chemistry
H(1S) + wall_S(v) -> wall_H(S) | thermalEffusionSurface |
1, 0, gasTemperature
wall_H(F) + wall_S(v) -> wall_H(S) + wall_F(v) | surfaceTransport |
6.7e14, 0.5*37e3, 1, 4.157e3, true
H(1S) + wall_H(S) -> H2(X,v=0) + wall_S(v) | thermalEffusionSurface |
1, 6.984e3, gasTemperature
wall_H(F) + wall_H(S) -> H2(X,v=0) + wall_S(v) + wall_F(v) | surfaceTransport |
6.7e14, 0.5*37e3, 1, 25.5e3, false
```

**Surface 4.2:** Mesoscopic surface model reactions for N<sub>2</sub>-H<sub>2</sub> system - Part 2: NH<sub>3</sub> synthesis pathway

```
% NH radical formation
N(4S) + wall_H(S) -> wall_NH(S) | thermalEffusionSurface |
1, 33.2e3, gasTemperature
wall_N(F) + wall_H(S) -> wall_NH(S) + wall_F(v) | surfaceTransport |
1e13, 0.5*51e3, 1, 33.2e3, true
H(1S) + wall_N(S) -> wall_NH(S) | thermalEffusionSurface |
1, 33.2e3, gasTemperature
wall_H(F) + wall_N(S) -> wall_NH(S) + wall_F(v) | surfaceTransport |
6.7e14, 0.5*37e3, 1, 33.2e3, true
NH(X) + wall_S(v) -> wall_NH(S) | thermalEffusionSurface |
1, 25e3, gasTemperature

% NH2 radical formation
H(1S) + wall_NH(S) -> wall_NH2(S) | thermalEffusionSurface |
1, 25e3, gasTemperature
wall_H(F) + wall_NH(S) -> wall_NH2(S) + wall_F(v) | surfaceTransport |
6.7e14, 0.5*37e3, 1, 0, true
NH(X) + wall_H(S) -> wall_NH2(S) | thermalEffusionSurface |
1, 25e3, gasTemperature
NH2(X) + wall_S(v) -> wall_NH2(S) | thermalEffusionSurface |
1, 25e3, gasTemperature

% NH3 formation and desorption
H(1S) + wall_NH2(S) -> NH3(X) + wall_S(v) | thermalEffusionSurface |
1, 25e3, gasTemperature
wall_H(F) + wall_NH2(S) -> NH3(X) + wall_S(v) + wall_F(v) | surfaceTransport |
6.7e14, 0.5*37e3, 1, 0, false
NH2(X) + wall_H(S) -> NH3(X) + wall_S(v) | thermalEffusionSurface |
1, 25e3, gasTemperature
H2(X, v=0) + wall_NH(S) -> NH3(X) + wall_S(v) | thermalEffusionSurface |
1, 0, gasTemperature
```

**Surface 4.3:** Mesoscopic surface model reactions for N<sub>2</sub>-H<sub>2</sub> system - Part 3: Metastable species mechanisms

```
% Metastable N and H atoms - Physisorption
N(2P) + wall_F(v) -> wall_N(F) | thermalEffusionSurface |
1, 0, gasTemperature
N(2D) + wall_F(v) -> wall_N(F) | thermalEffusionSurface |
1, 0, gasTemperature
H(2S) + wall_F(v) -> wall_H(F) | thermalEffusionSurface |
1, 0, gasTemperature
H(2P) + wall_F(v) -> wall_H(F) | thermalEffusionSurface |
1, 0, gasTemperature
H(3) + wall_F(v) -> wall_H(F) | thermalEffusionSurface |
1, 0, gasTemperature
H(4) + wall_F(v) -> wall_H(F) | thermalEffusionSurface |
1, 0, gasTemperature
```

H(5) + wall_F(v) -> wall_H(F)	thermalEffusionSurface	
1, 0, gasTemperature		
% Metastable N and H atoms - Chemisorption		
N(2D) + wall_S(v) -> wall_N(S)	thermalEffusionSurface	
1, 0, gasTemperature		
N(2P) + wall_S(v) -> wall_N(S)	thermalEffusionSurface	
1, 0, gasTemperature		
H(2S) + wall_S(v) -> wall_H(S)	thermalEffusionSurface	
1, 0, gasTemperature		
H(2P) + wall_S(v) -> wall_H(S)	thermalEffusionSurface	
1, 0, gasTemperature		
H(3) + wall_S(v) -> wall_H(S)	thermalEffusionSurface	
1, 0, gasTemperature		
H(4) + wall_S(v) -> wall_H(S)	thermalEffusionSurface	
1, 0, gasTemperature		
H(5) + wall_S(v) -> wall_H(S)	thermalEffusionSurface	
1, 0, gasTemperature		
% Metastable atoms - Recombination		
N(2D) + wall_N(S) -> N2(X,v=0) + wall_S(v)	thermalEffusionSurface	
1, 0, gasTemperature		
N(2P) + wall_N(S) -> N2(X,v=0) + wall_S(v)	thermalEffusionSurface	
1, 0, gasTemperature		
H(2S) + wall_H(S) -> H2(X,v=0) + wall_S(v)	thermalEffusionSurface	
1, 0, gasTemperature		
H(2P) + wall_H(S) -> H2(X,v=0) + wall_S(v)	thermalEffusionSurface	
1, 0, gasTemperature		
H(3) + wall_H(S) -> H2(X,v=0) + wall_S(v)	thermalEffusionSurface	
1, 0, gasTemperature		
H(4) + wall_H(S) -> H2(X,v=0) + wall_S(v)	thermalEffusionSurface	
1, 0, gasTemperature		
H(5) + wall_H(S) -> H2(X,v=0) + wall_S(v)	thermalEffusionSurface	
1, 0, gasTemperature		
% Metastable atoms - NH formation		
N(2D) + wall_H(S) -> wall_NH(S)	thermalEffusionSurface	
1, 0, gasTemperature		
N(2P) + wall_H(S) -> wall_NH(S)	thermalEffusionSurface	
1, 0, gasTemperature		
H(2S) + wall_N(S) -> wall_NH(S)	thermalEffusionSurface	
1, 0, gasTemperature		
H(2P) + wall_N(S) -> wall_NH(S)	thermalEffusionSurface	
1, 0, gasTemperature		
H(3) + wall_N(S) -> wall_NH(S)	thermalEffusionSurface	
1, 0, gasTemperature		
H(4) + wall_N(S) -> wall_NH(S)	thermalEffusionSurface	
1, 0, gasTemperature		

```

H(5) + wall_N(S) -> wall_NH(S) | thermalEffusionSurface |
1, 0, gasTemperature

% Metastable atoms - NH2 formation
H(2S) + wall_NH(S) -> wall_NH2(S) | thermalEffusionSurface |
1, 0, gasTemperature
H(2P) + wall_NH(S) -> wall_NH2(S) | thermalEffusionSurface |
1, 0, gasTemperature
H(3) + wall_NH(S) -> wall_NH2(S) | thermalEffusionSurface |
1, 0, gasTemperature
H(4) + wall_NH(S) -> wall_NH2(S) | thermalEffusionSurface |
1, 0, gasTemperature
H(5) + wall_NH(S) -> wall_NH2(S) | thermalEffusionSurface |
1, 0, gasTemperature

% Metastable atoms - NH3 formation
H(2S) + wall_NH2(S) -> NH3(X) + wall_S(v) | thermalEffusionSurface |
1, 0, gasTemperature
H(2P) + wall_NH2(S) -> NH3(X) + wall_S(v) | thermalEffusionSurface |
1, 0, gasTemperature
H(3) + wall_NH2(S) -> NH3(X) + wall_S(v) | thermalEffusionSurface |
1, 0, gasTemperature
H(4) + wall_NH2(S) -> NH3(X) + wall_S(v) | thermalEffusionSurface |
1, 0, gasTemperature
H(5) + wall_NH2(S) -> NH3(X) + wall_S(v) | thermalEffusionSurface |
1, 0, gasTemperature

```

#### 4.1.2 Implementation in LoKI-B+C

The chemical kinetics data used in LoKI-B+C is parsed from structured .chem files, which serve as primary interface between the chemical model and the simulation solver. The .chem files specify all species, volume/surface reactions and rate coefficients, and transport models within a standardized format, following the general syntax (Reference Manual LoKI-B+C, to be published):

Reactants -> Products | Type | Parameters | Notes/References

where Reactants -> Products represent the chemical reactions (including transport processes), Type specifies the type of rate coefficient, Parameters are the parameters needed to calculate the rate coefficient, and Notes/References are complementary information.

A state-specific notation is employed, detailing electronic species, e.g. \$N2(A3Su+)\$, \$H(1S)\$, \$N(2D)\$; vibrational species, e.g. \$N2(X,v=0..44)\$, \$H2(X,w=0..14)\$; and also ions, e.g. \$H3(+,X)\$, \$H(-,"gnd")\$ (see Section 2).

The field Type encompasses temperature-independent rate coefficient constantRateCoeff and temperature-dependent rate coefficient expressions, such as arrheniusGasTemp ( $a \exp\left(\frac{b}{T_g}\right)$ ), modifiedArrheniusGasTemp ( $a T_g^b \exp\left(\frac{c}{T_g}\right)$ ), powerGasTemp ( $a T_g^b$ ), and powerElectronTemp ( $a T_e^b$ ). The parameters a, b, c are specified in the Parameters field.

Transport and wall Type include QGMTransport for the charged-particle transport adopted by QUANTEMOL global-model [61], multicomponentDiffusion for multi-component diffusion using Lennard-Jones parameters, and wallReaction for wall recombination reactions with specified probabilities. Mesoscopic surface model Type encompass thermalEffusionSurface for physical and chemical adsorption rate coefficients, thermalDesorption for desorption processes, and surfaceTransport for surface diffusion. More details can be found in the LoKI user manual [35].

Illustrative snippets from the latest Chemical Scheme (CS) implemented in LoKI-B+C (N2H2\_CS18a.chem) are shown below:

**Chemical Scheme 4.4:** Example reactions from N2H2\_CS18a.chem kinetic scheme.

```

1: % Header (metadata and changelog)
2: % - updates cross-section files (e.g., NH3_LXCat_extra.txt)
3: % - fixes stoichiometry/rates and adds missing reactions
4:
5: % electron-impact (electronic excitation via EEDF)
6: e + N2(X,v=0) <-> e + N2(A3Su+) | eedf | |

7: % Direct literature value (constant rate coefficient)
8: N2(A3Su+) + NH3(X) -> N2(X,v=0) + H(1S) + NH2(X) | constantRateCoeff | 8.5E-17 |
9: % Comment: modified according to Capitelli; original 1.6E-16
10:
11: % neutral-neutral (Arrhenius in Tg)
12: H(1S) + NH(X) -> N(4S) + H2(X,v=0) | arrheniusGasTemp | 5.4E-17, -165 |
13:
14: % mesoscopic surface (Gordiets 1998 inspired)
15: N(4S) + wall_F(v) -> wall_N(F) | thermalEffusionSurface | 1, 0, gasTemperature |

```

The Type of some rate coefficients use eedf. This refers to electron-impact rate coefficients, which are calculated by integrating cross sections over the EEDF.

In LoKI-B+C framework, cross sections are provided in standardized LXCat [33] format files, which contain energy-dependent cross-section data for various collision processes. The cross section files include comprehensive coverage of collision processes, encompassing elastic momentum-transfer, vibrational excitation, electronic excitation, ionization and dissociative attachment. Tables 3 and 4(bla bla) show snippets of cross section data used in this work for  $NH_3$  and  $H_2$ , respectively.

**Cross-section 4.5:**  $NH_3$  electronic excitation cross-section snippet taken from LXCat

```

1: EXCITATION
2: E + NH3 -> E + NH3(E1)
3: 5.300000e+0
4: SPECIES: e / NH3
5: PROCESS: E + NH3 -> E + NH3(E1)(5.30eV), Excitation

```

```

6: PARAM.: E = 5.30 eV
7: COMMENT: [E + NH3(X) -> E + NH3(E1), Excitation] Ramses Snoeckx et al 2023
8: COLUMNS: Energy (eV) | Cross section (m2)
9: -----
10: 5.3    0.0
11: 5.31   4.38E-23
12: 5.32   8.84E-23
13: 5.5    7.639E-22
14: 6.0    2.787E-21
15: 7.0    4.8269E-21
16: 8.0    5.878E-21
17: 10.0   3.7986E-21
18: 15.0   1.8003E-21
19: 20.0   1.4845E-21
20: -----

```

#### **Cross-section 4.6: H<sub>2</sub> vibrational excitation cross-section snippet taken from LXCat**

```

1: EXCITATION
2: Hydrogen -> Hydrogen (H2(X,v=0) -> H2(X,v=1))
3: 0.516000e+0
4: SPECIES: e / Hydrogen
5: PROCESS: E + Hydrogen -> E + Hydrogen (H2(X,v=0) -> H2(X,v=1)), Excitation
6: PARAM.: E = 0.516 eV
7: COMMENT: [e + H2(X,v=0) -> e + H2(X,v=1), Excitation]
8: COLUMNS: Energy (eV) | Cross section (m2)
9: -----
10: 0.516   0.0
11: 0.52    1.2E-20
12: 0.6     2.8E-20
13: 0.8     3.1E-20
14: 1.0     2.9E-20
15: 2.0     1.8E-20
16: 5.0     6.5E-21
17: 10.0    2.1E-21
18: -----

```

The cross-section data used in this work originates from multiple validated sources. The primary database utilized is the IST-Lisbon database on LXCat [62], which provides complete, validated sets of cross sections for  $H_2$ ,  $N_2$ , and  $NH_3$  (in some cases to be published). To validate cross-section datasets, **electron swarm parameters** obtained from EBE solution are commonly employed as benchmarks. Electron swarm parameters are constituted by macroscopic transport parameters of electrons in gases under applied electric fields, including **characteristic energy**, **reduced mobility** and **drift velocity**, as well as electron rate coefficients, including **Townsend ionization and attachment coefficients**. These parameters can be directly measured in controlled swarm experiments and compared against simulations from Boltzmann solvers. For the IST-Lisbon database, predictions typically agree with experimental measurements within less than 20% for reduced electric fields  $\frac{E}{N} \approx 10^{-4} - 500$  Td [62]. The validation

plots shown below compare calculated swarm parameters (lines) against experimental data points for  $H_2$  and  $NH_3$  @shubham\_article.

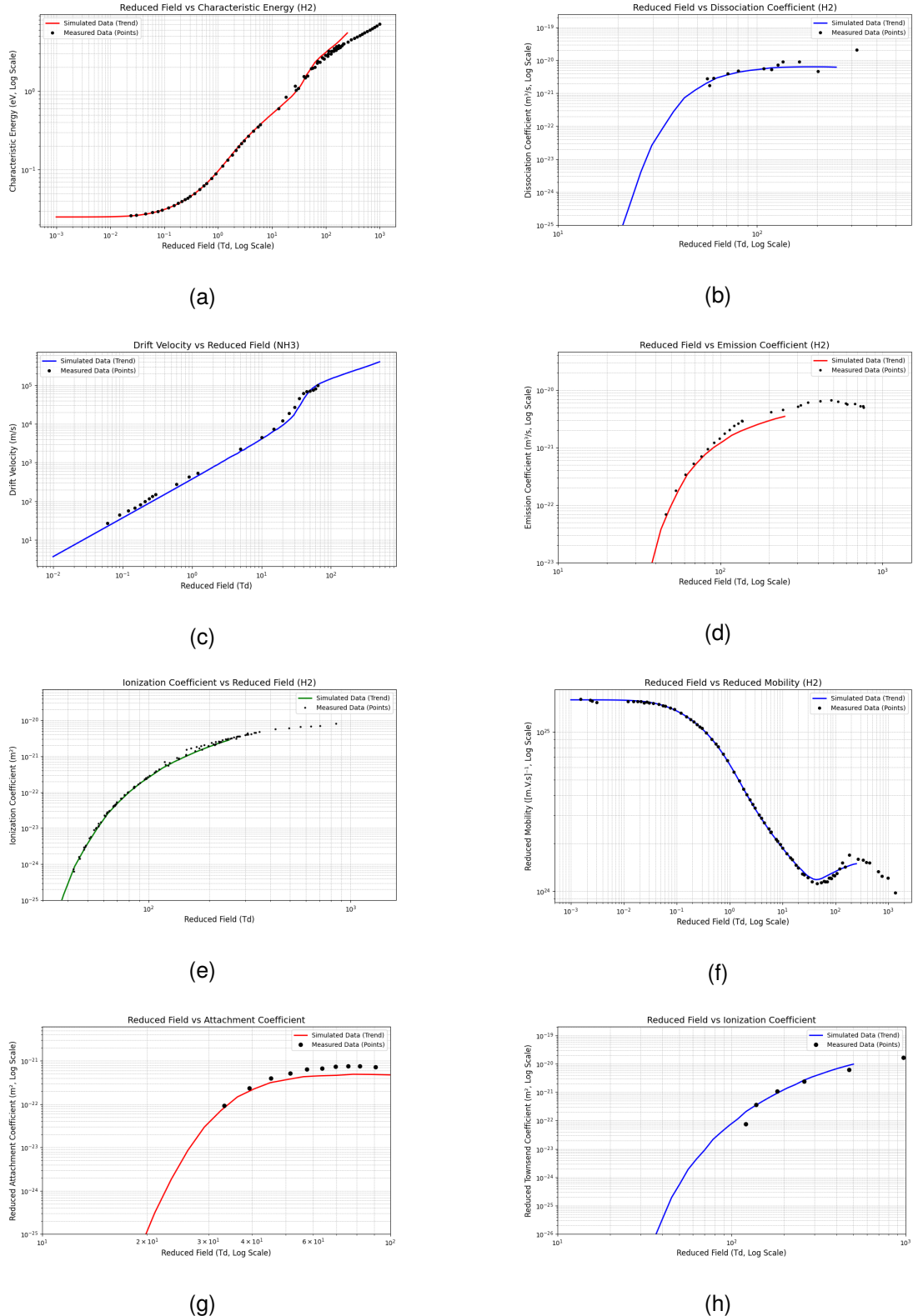


**Figure 4.1:** Validation of swarm parameters for  $H_2$  and  $NH_3$ .

## 4.2 Validation of the Chemical Model

The validation of the chemical kinetic model developed in this thesis is performed by comparing key model outputs against published experimental data. The primary observables selected for this validation are the densities of relevant chemical species and the reduced electric field ( $E/N$ ), which correspond to experimentally measured plasma properties.

The goal of this comparison is not necessarily to achieve perfect quantitative agreement, but rather to confirm that the model correctly reproduces the observed experimental trends, within reasonable uncertainties. Quantitative results will be given attention whenever possible. Agreement on how species densities and  $E/N$  evolve with varying external conditions—such as gas pressure, discharge current, and initial  $H_2$  concentration in the gas mixture — will give confidence that the model is able to capture the dominant chemical kinetic pathways.

### 4.2.1 Simulation setup in LoKI

Model validation was conducted through simulations using the LoKI framework, and comparison against the following experimental data:

- **Reduced Electric Field ( $E/N$ ):** data from Cernogora *et al.* [63] and Brovikova & Galiaskarov [64] in pure  $N_2$  discharges, as well as measurements from this work in  $N_2 - H_2$  discharges are used to validate the electron kinetics and power coupling mechanisms [capítulo anterior e projeto referencia].
- **Species Densities ( $[NH_3]$ ,  $[N]$ ,  $[H]$ ):** data from Amorim *et al.* [2] and the present work in  $N_2 - H_2$  discharges.

A critical aspect of this validation is a thorough analysis of the conditions and methods employed to obtain the experimental data. Factors such as the precision of measurements, and the values of gas temperature and gas flow rates are often not clearly specified or controlled in the experiments. For example, as discussed in Chapter 2, variations in the gas temperature directly impact the gas number density ( $N$ ), thus affecting all kinetic rates. These issues introduce inherent uncertainties and must be carefully considered when comparing simulation results with experimental measurements.

#### 4.2.1.1 Analysis of Experimental Conditions and Methodologies

The experimental works of Cernogora *et al.* [63], Brovikova & Galiaskarov [64] and Amorim *et al.* [2] all employed DC glow discharges in cylindrical tubes operated with a continuous gas flow. However, the specific operational parameters and diagnostic techniques adopted by these authors varied significantly, as shown in Table 4.3 and discussed below.

**Table 4.3:** Summary of operational parameters

Study	Gases	Geometry	Pressure	Current
-------	-------	----------	----------	---------

Amorim <i>et al.</i> (1994 and 1996) [2], [65]	$N_2 - H_2$	Pyrex tube, 1.6 cm	0.5–5.0 Torr	1–50 mA
Brovikova & Galiaskarov (2001) [64]	Pure $N_2$	S-52 glass tube, 1.5 cm	0.45–4.0 Torr	10–80 mA
Cernogora <i>et al.</i> (1981) [63]	Pure $N_2$	Pyrex tube, 2.0 cm	0.1–2.0 Torr	0–80 mA

### 1. Amorim *et al.* (1994 and 1996): Absolute Densities of $[NH_3]$ and $[H]$ in $N_2 - H_2$

- **Measurement Technique:** This study used a combination of Photofragment Translational Spectroscopy (PFTS) and Laser-Induced Fluorescence (LIF) to measure species densities. A 205 nm laser photodissociated the  $NH_3$  molecules synthesized in the plasma, and the resulting “hot” H-atom fragments were detected via LIF on the H-alpha line (656 nm) during the same laser pulse. The density of “cold” H atoms produced by the discharge was measured simultaneously from the narrow core of the LIF spectral profile.
- **Absolute Calibration:** The H-atom LIF signal was calibrated using Vacuum Ultraviolet (VUV) absorption spectroscopy on the Lyman- $\alpha$  line (121 nm) in a pure  $H_2$  discharge.
- **Key Results:** A maximum  $NH_3$  density of approximately  $8 \times 10^{12} \text{ cm}^{-3}$  was measured in a 75%  $H_2$  – 25%  $N_2$  mixture at 2 Torr and 50 mA. The H-atom dissociation energy from  $NH_3$  was determined to be  $(4.34 \pm 0.07)$  eV.

### 2. Brovikova & Galiaskarov (2001): $E/N_0$ and $[N]$ in Pure $N_2$

- **Measurement Technique:** The ground-state N-atom concentration,  $[N(^4S)]$ , was measured using Electron Paramagnetic Resonance (EPR). The longitudinal electric field ( $E$ ) was measured using a two-probe current compensation method.
- **Key Results:** The reduced electric field,  $E/N_0$ , was measured in the range of  $5.27 \times 10^{-16} \text{ V cm}^2$  across pressures of 60–533 Pa and currents of 10–80 mA.
- **Temperature and Flow:** This work is particularly valuable as it provides systematic measurements of both the axial gas temperature ( $T_0$ ) and wall temperature ( $T_{\text{wall}}$ ).  $T_0$  varied significantly from 331.5 K to 680.6 K, highlighting the importance of thermal effects. Gas flow rates were also detailed, ranging from 0.082 to 2.788  $\text{cm}^3/\text{s}$ , and were used in their kinetic analysis to determine species lifetimes and dissociation rates [confirmar].

### 3. Cernogora *et al.* (1981): $E$ and $[N]$ in Pure $N_2$

- **Measurement Technique:** The axial electric field ( $E$ ) was measured from the floating potential difference between two electrostatic probes. The N-atom concentration,  $[N(^4S)]$ , was determined downstream of the discharge using the classic NO titration method. Electron density was measured with a microwave cavity technique.

- **Key Results:** The study reported that  $E/p$  decreases as the discharge current increases, a behavior they attributed to gas heating. Their kinetic model showed good agreement with experimental  $E/p$  at low currents where gas heating was negligible ( $T_G \approx 300$  K).
- **Temperature and Flow:** Gas temperature was deduced from the rotational distribution of the  $N_2$  second positive system and was found to reach up to 600 K at higher currents. The N-atom measurements were performed in a flow system with rates from 0.1 to 6 cm<sup>3</sup>/s NTP.

All three studies, either directly or indirectly, confirm that gas heating is a dominant effect. Brovikova & Galiaskarov provide the most comprehensive data, showing a temperature increase of over 300 K with current and pressure. Cernogora *et al.* note that gas heating (up to 600 K) must be included to explain the behavior of  $E/p$  at high currents. Amorim *et al.* measured H-atom temperatures between 500 and 1200 K, significantly higher than the molecular gas temperature, and demonstrated that accounting for this thermal non-equilibrium is essential for accurate VUV absorption calibration. Since the gas number density  $N$  is inversely proportional to  $T_{\text{gas}}$ , any model validation for  $E/N$  or density-dependent reaction rates must carefully account for the gas temperature. The reported precision of the measurements varies. Brovikova & Galiaskarov state a measurement error not exceeding 40% for absolute N-atom concentration. Amorim *et al.* estimate an uncertainty of likely more than  $\pm 20\%$  for their  $[NH_3]$  density value, due to the multi-step calibration process. Cernogora *et al.* do not provide explicit error bars for their E-field measurements. This range of uncertainty sets a realistic expectation for the level of quantitative agreement between our model and the experimental data. The experiments were all performed in flow systems, but at different rates. Brovikova & Galiaskarov used low, carefully controlled flow rates as a key parameter in their kinetic model. Cernogora *et al.* also used low flow rates for N-atom titration. Amorim *et al.* mention a “permanent gas flow” but do not quantify it for the  $NH_3$  measurements. The difference in flow rates implies different residence times for species in the plasma, which can significantly alter the plasma chemistry, especially for synthesis reactions like that of ammonia. This is a key difference in experimental conditions that must be considered.

## 4.2.2 Results and Discussion

The validation of the chemical kinetic model is presented through systematic comparison with experimental data. The analysis is organized into three main sections: the electrical characteristics of the plasma, the concentration of key atomic species, and the production of ammonia.

### 4.2.2.1 Electrical Characteristics: Electric Field and Reduced Electric Field

The model’s ability to predict fundamental electrical properties of the discharge is evaluated by comparing simulations against experimental data from Cernogora *et al.* [63] and Brovikova & Galiaskarov [64].

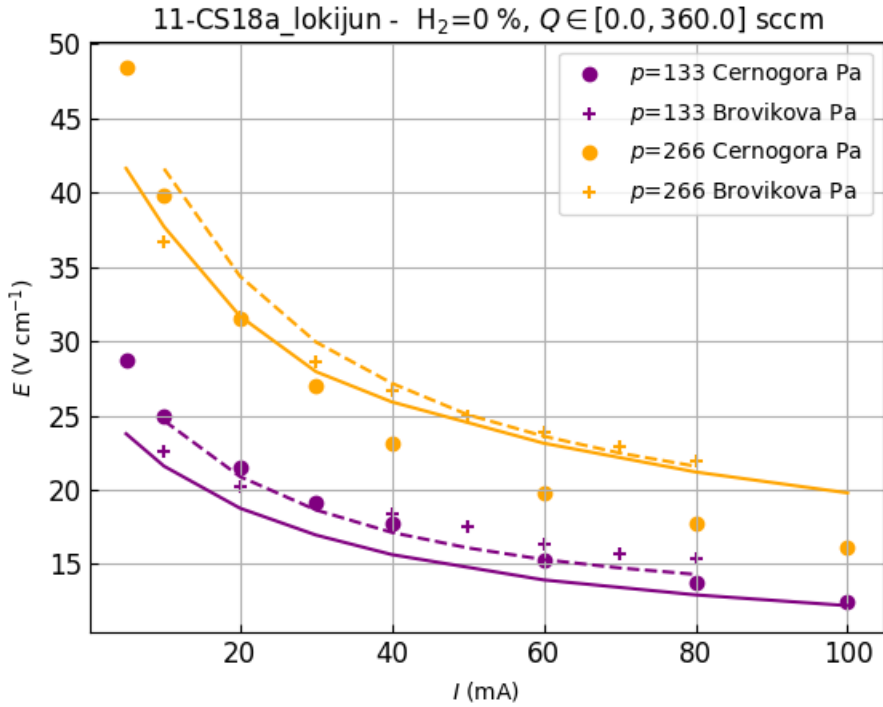


**Figure 4.2:** Axial electric field ( $E$ ) as a function of discharge current ( $I$ ) in pure nitrogen plasma at two pressures: 133 Pa (purple) and 266 Pa (orange). Points and crosses represent experimental data from Cernogora and Brovikova, while solid and dashed lines show simulation results with Cernogora and Brovikova data, respectively.

The axial electric field as a function of discharge current shows a characteristic behavior of glow discharges. For all datasets, the electric field decreases as the current increases. This trend reflects the increase in plasma conductivity with higher ionization levels, requiring a lower electric field to sustain the current. The electric field is consistently higher at 266 Pa compared to 133 Pa, as expected from the increased collision frequency at higher gas densities. The simulations successfully reproduce the general trends observed in both experimental datasets, despite noticeable differences between the Cernogora and Brovikova measurements themselves, which highlight inherent experimental uncertainties.

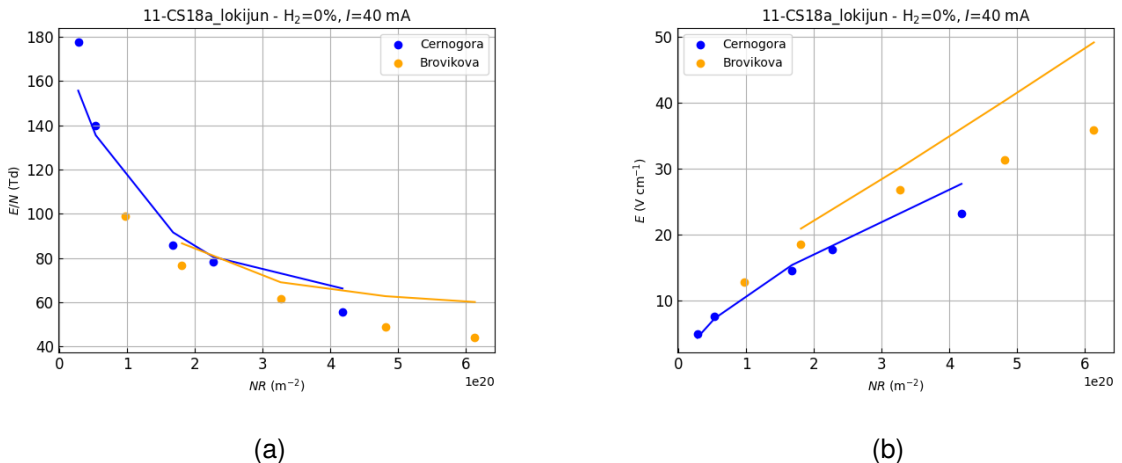


**Figure 4.3:** Left: Reduced electric field ( $E/N$ ) in Td. Right: Electric field ( $E$ ) in  $\text{V cm}^{-1}$ . Both as a function of  $NR$  (gas density times tube radius) for a fixed current of 40 mA in pure nitrogen. Simulation lines follow experimental (points) trends from Cernogora and Brovikova datasets.

The reduced electric field  $E/N$ , a crucial parameter governing the electron energy distribution, decreases as the product  $NR$  increases. This behavior indicates that at higher gas densities, a lower relative field is needed to sustain the plasma. The simulation lines demonstrate good agreement with experimental trends for both the Cernogora and Brovikova datasets, suggesting that the electron-collision cross-sections used in the model for  $N_2$  are consistent. This is fundamental to correctly calculating reaction rates in the plasma.

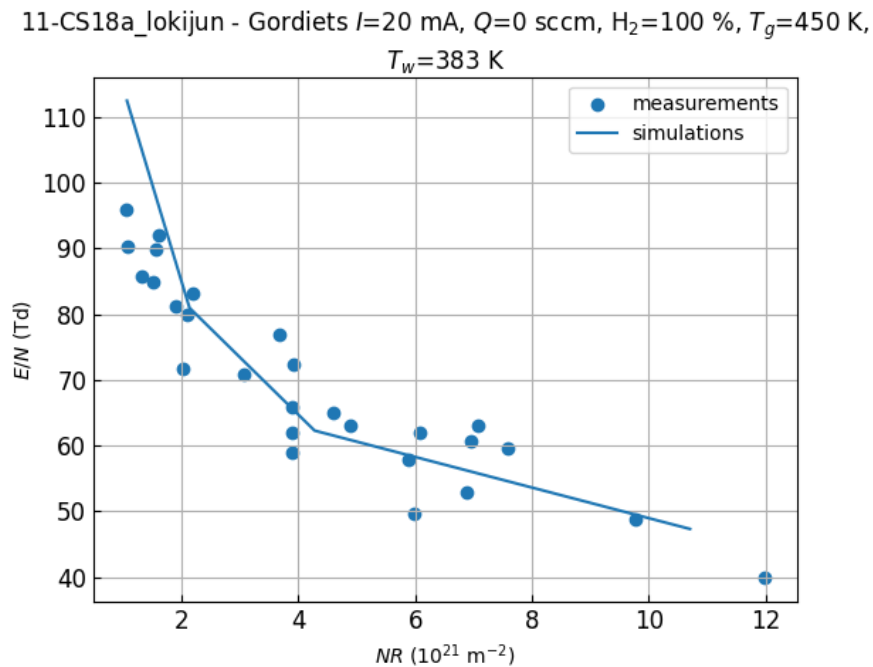


**Figure 4.4:** Reduced electric field ( $E/N$ ) in pure hydrogen plasma as a function of  $NR$ . The simulation (solid line) shows excellent agreement with experimental measurements from Amorim *et al.* [2].

In pure hydrogen plasma, the simulation demonstrates excellent quantitative agreement with experimental measurements across the entire range of  $NR$  values. The model accurately captures the decay of  $E/N$  with increasing  $NR$ , indicating that the description of electron kinetics in pure hydrogen is robust. This validation in both pure  $N_2$  and pure  $H_2$  conditions provides confidence in the model's ability to handle the mixed  $N_2$ - $H_2$  system.

#### 4.2.2.2 Atomic Species Concentration in $N_2$ - $H_2$ Mixtures

The model's capability to predict the densities of atomic nitrogen and hydrogen as the gas mixture composition varies is evaluated next. These atomic species are the primary building blocks for ammonia synthesis.

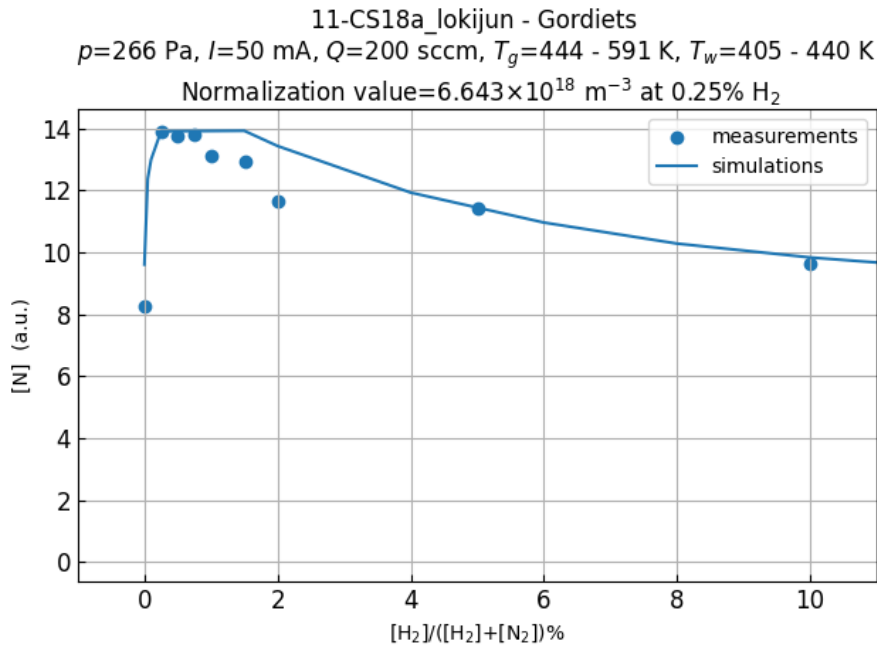


**Figure 4.5:** Concentration of atomic nitrogen ( $[N]$ ) as a function of  $H_2$  percentage in the discharge, for Amorim *et al.* [2] data. The simulation captures the catalytic effect of hydrogen on nitrogen dissociation, showing a peak enhancement around 1-2%  $H_2$ .

The concentration of atomic nitrogen exhibits a remarkable catalytic effect when small amounts of hydrogen are added to the nitrogen discharge. The graph clearly shows that adding approximately 1-2%  $H_2$  significantly enhances  $N_2$  dissociation, producing much higher  $[N]$  concentrations than in pure nitrogen. This phenomenon results from quenching of excited nitrogen states by  $H_2$ , creating a more efficient pathway for dissociation. Beyond this peak, further hydrogen addition dilutes the nitrogen, causing  $[N]$  concentration to decrease. The simulation perfectly captures this catalytic effect qualitatively, correctly predicting the sharp initial rise, the peak location, and the subsequent gradual decay. This represents a strong validation of the core chemical kinetics scheme concerning nitrogen dissociation in the presence of hydrogen.

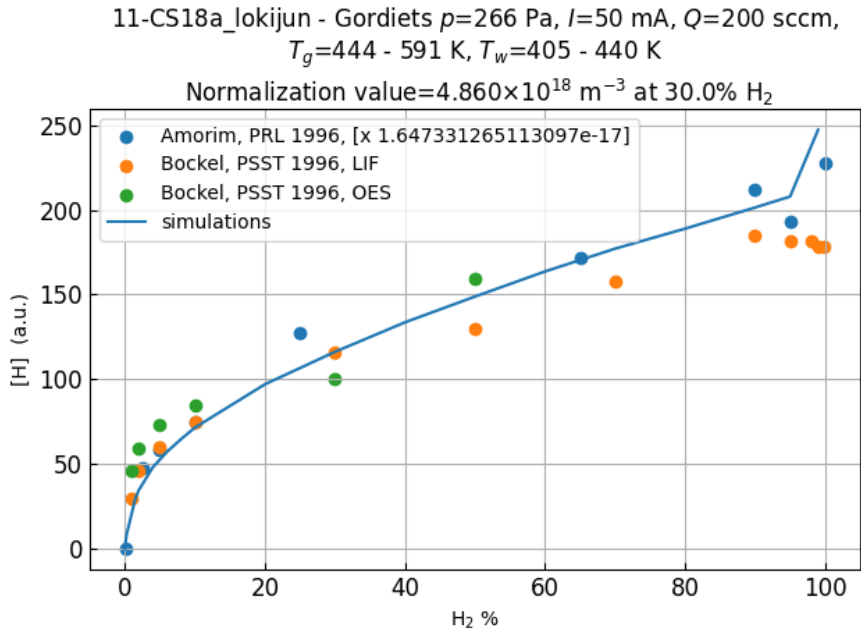


**Figure 4.6:** Relative concentration of atomic hydrogen ( $[H]$ ) as a function of H<sub>2</sub> percentage. The simulation shows excellent quantitative agreement with three different experimental datasets, namely Amorim *et al.* [2], across the entire composition range.

The concentration of atomic hydrogen increases steadily as more H<sub>2</sub> is added to the feed gas, as expected. The simulation shows excellent quantitative agreement with all three experimental datasets across the entire range of gas compositions. This demonstrates that the model accurately describes the electron-impact dissociation of H<sub>2</sub> molecules and the subsequent atomic hydrogen chemistry. The consistency across multiple experimental sources further strengthens confidence in this aspect of the model.

#### 4.2.2.3 Ammonia (NH<sub>3</sub>) Synthesis

The ultimate test of the model is its ability to predict ammonia synthesis, which represents the culmination of complex gas-phase and surface reaction pathways.

11-CS18a\_lokijun - Gordiets  $p=266$  Pa,  $I=50$  mA,  $Q=200$  sccm,  $T_g=444$   
 $- 591$  K,  $T_w=405$  -  $440$  K

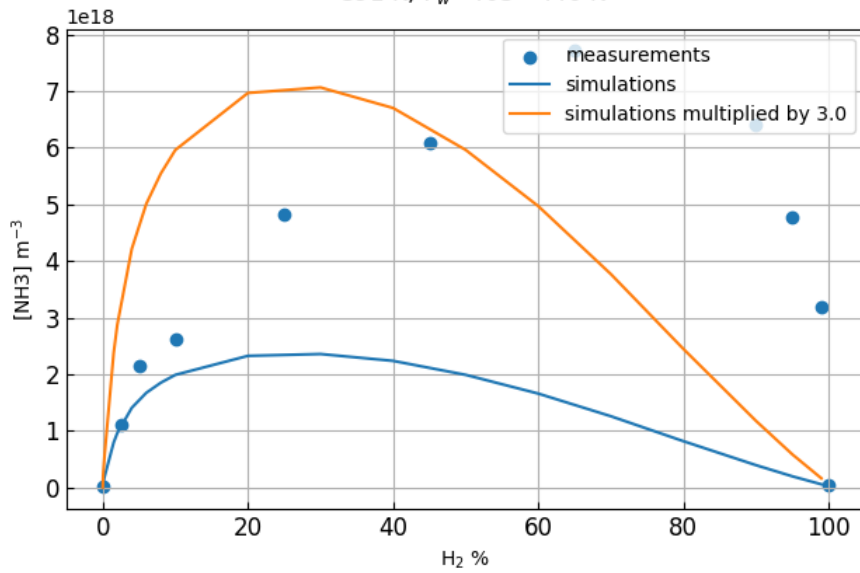


**Figure 4.7:** Absolute concentration of ammonia ( $[NH_3]$ ) as a function of  $H_2$  percentage, for Amorim *et al.* [2] data. The orange line shows the simulation result scaled by a factor of 3 for comparison.

The ammonia concentration as a function of hydrogen percentage reveals both the strengths and limitations of the current model. Experimental measurements show that  $NH_3$  production is maximized with hydrogen fractions around 70-80%. The simulation correctly predicts the existence of a peak, although it is slightly shifted to the left, to the 20-30%  $H_2$  range. However, it severely underestimates the absolute concentration by approximately a factor of 3. This discrepancy points to potential issues in the chemical scheme for  $NH_3$  formation or destruction pathways. Possible sources include inaccuracies in reaction rates for surface recombination mechanisms (Eley-Rideal or Langmuir-Hinshelwood processes) or gas-phase  $NH_x$  radical chemistry.

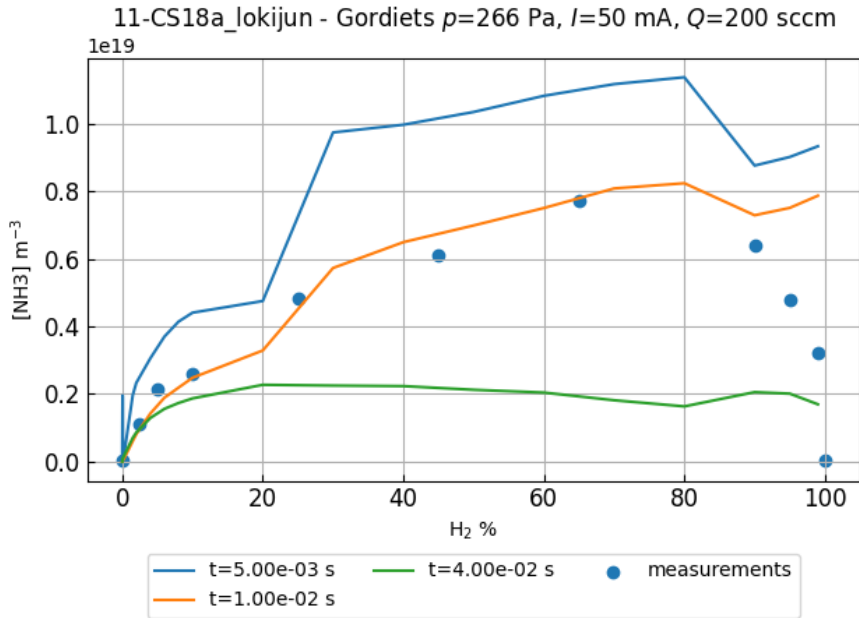


**Figure 4.8:** Sensitivity of predicted  $[NH_3]$  concentration to gas residence time in the plasma. Different lines represent simulations with residence times of 5 ms (blue), 10 ms (orange), 20 ms (green), for Amorim *et al.* [2] data. The 10 ms residence time provides the best fit to experimental data.

A critical finding emerges from the sensitivity analysis of gas residence time: the model's output for  $[NH_3]$  is highly sensitive to this parameter. A shorter residence time of 5 ms overpredicts the concentration, while longer times of 40 ms significantly underpredict it. An intermediate residence time of 10 ms provides the best fit to experimental data. This strong sensitivity suggests that the discrepancies observed in absolute ammonia concentrations may not be solely due to incorrect reaction rates. Instead, they may be significantly influenced by uncertainties in estimating how long gas molecules interact within the plasma. The gas residence time affects both the extent of chemical conversion and the balance between formation and destruction pathways. This highlights the importance of accurately modeling both the chemical kinetics and the gas transport (flow patterns and residence time distributions) for predicting complex product molecules like  $NH_3$ .

#### 4.2.2.4 Additional Validation: Reduced Electric Field in $N_2$ - $H_2$ Mixtures

The model's performance in predicting the reduced electric field across different gas compositions is further validated using experimental data from LPP. This validation is particularly important as the reduced electric field directly governs the electron energy distribution and, consequently, all electron-impact processes in the plasma.

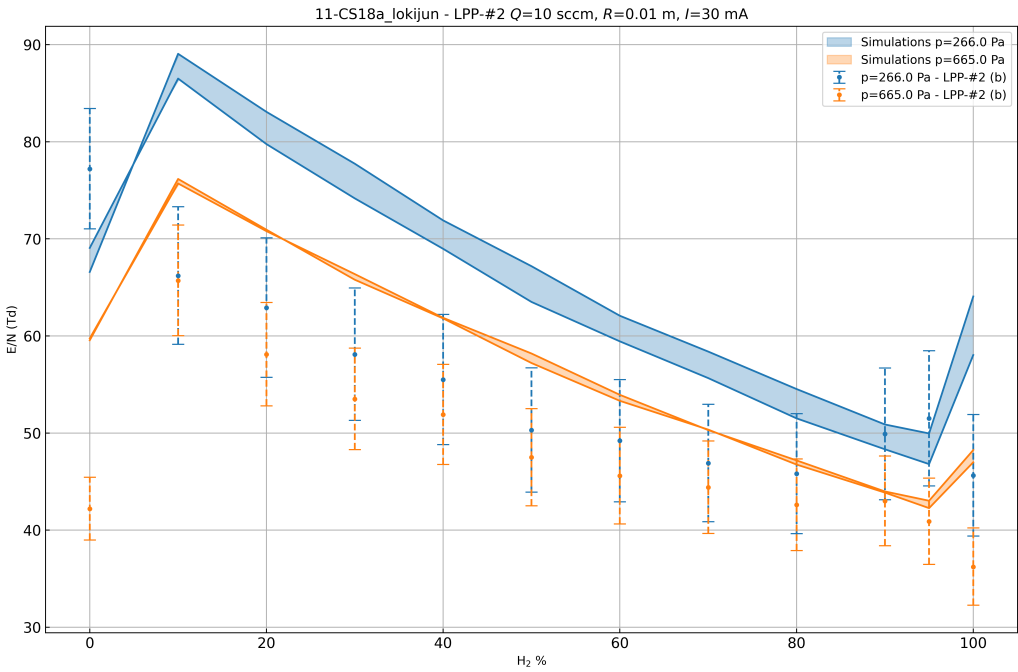


**Figure 4.9:** Reduced electric field ( $E/N$ ) as a function of hydrogen percentage ( $H_2\%$ ) for two pressure conditions: 266.0 Pa (blue) and 665.0 Pa (orange). Shaded bands represent simulation results with uncertainty ranges, while points with error bars show experimental measurements from LPP.

The reduced electric field shows a non-monotonic dependence on the hydrogen concentration. For both pressure conditions,  $E/N$  initially increases with small additions of  $H_2$  (up to 10%), reaches a maximum, then decreases significantly as  $H_2$  concentration increases further (up to 90%), and finally shows a sharp increase when approaching 100%  $H_2$ . This behavior reflects the changing electron energy distribution and collision processes as the gas composition varies.

The simulation bands (shaded areas) account for the uncertainty in gas temperature, estimated at approximately 50 K as discussed in Chapter 3. This temperature uncertainty directly affects the gas density and, consequently, the calculated  $E/N$  values. The experimental error bars incorporate similar temperature uncertainties.

The last data point at 100%  $H_2$  deviates significantly from the general trend and should be interpreted with caution. As discussed in Chapter 3, the gas temperature determination method relies on fitting the peak of  $N_2$  rotational temperature measurements. In pure hydrogen plasmas, where nitrogen is absent, this temperature diagnostic method becomes unreliable, leading to potentially inaccurate temperature estimates. The temperature values for this condition were obtained through visual regression, which, as evidenced by these trends, did not provide well-constrained results.

The higher  $E/N$  values at the lower pressure (266.0 Pa) compared to the higher pressure (665.0 Pa) are consistent with the expected pressure dependence of glow discharge characteristics, where reduced collision frequency at lower pressures requires higher fields to sustain the discharge.

In summary, the model successfully predicts fundamental plasma parameters, including the electric field ( $E$ ) and reduced electric field ( $E/N$ ), in both pure  $N_2$  and pure  $H_2$  plasmas across a wide range

of conditions. It accurately reproduces the concentrations of primary dissociation products—atomic nitrogen ( $[N]$ ) and atomic hydrogen ( $[H]$ )—including complex phenomena such as the catalytic effect of  $H_2$  on  $N_2$  dissociation. The qualitative trends for all species and conditions are generally captured. The primary challenge lies in quantitatively predicting the concentration of ammonia ( $NH_3$ ). Currently, it underestimates the absolute concentration by approximately a factor of 3. This indicates that refinement is needed in either the chemical pathways for  $NH_3$  formation and destruction (particularly surface chemistry mechanisms) or in the treatment of gas residence time and transport effects. The strong sensitivity to residence time suggests that future work should focus on coupled kinetic-transport models that more accurately represent the experimental flow conditions.

For reference, an example of a .in file for a simulation in LoKI-B+C is shown below:

**Simulation Setup 4.7:** Example configuration file (`N2H2_simulation.in`) for LoKI-B+C simulations of  $N_2$

- $H_2$  plasmas.

```

%%%%%%%%%%%%%%%%%%%%%%%%%%%%%%%%%%%%%
% N2-H2 WORKING CONFIGURATION FILE LOKI %
% (subject to change during development) %
%%%%%%%%%%%%%%%%%%%%%%%%%%%%%%%%%%%%%

% --- configuration of the working conditions ---
workingConditions:
  reducedField: 60 % in Td
  electronTemperature: 4.0 % in eV
  excitationFrequency: 0 % in Hz
  gasPressure: 532 % in Pa
  gasTemperature: 444 % in K (average gas temperature)
  wallTemperature: 363 % in K (wall temperature)
  extTemperature: 300 % in K (external temperature)
  surfaceSiteDensity: 1e20 % in m-2 (used for surface kinetics)
  electronDensity: 6.4e+15 % in m-3
  chamberLength: 0.23 % in m
  chamberRadius: 0.01 % in m
  dischargeCurrent: 0.020 % in A
  totalSccmInFlow: 7.400 % in sccm
  totalSccmOutFlow: ensureIsobaric % a number (in sccm) or a model: totalSccmInFlow, ensureIsobaric

% --- configuration of the electron kinetics ---
electronKinetics:
  isOn: true % true or false (to activate or deactivate the electron Kinetics)
  eedfType: boltzmann % boltzmann or prescribedEedf (generalized expression Maxwellian/Druyvesteyn)
%  shapeParameter: 1 % prescribedEedf shape parameter from 1 (Maxwellian) to 2 (Druyvesteyn)
  ionizationOperatorType: usingSDCS % conservative, oneTakesAll, equalSharing or usingSDCS
  growthModelType: temporal % temporal or spatial
  includeEECollisions: false % true or false (to include / remove e-e collisions)
  LXCatFiles:
    - Nitrogen/N2_LXCat.txt
    - Nitrogen/N2_vib_LXCat.txt
%     - Nitrogen/N2_rot_LXCat.txt
    - Nitrogen/N_LXCat.txt
    - Hydrogen/H2_LXCat.txt
    - Hydrogen/H2_vib_LXCat.txt
%     - Hydrogen/H2_EV_LXCat.txt
%     - Hydrogen/H2_rot_LXCat.txt
    - Hydrogen/H_LXCat.txt

```

```

- Ammonia/NH3_LXCat.txt
LXCatFilesExtra: % extra cross section files
- Nitrogen/N2_LXCat_extra.txt
- Nitrogen/N_LXCat_extra.txt
- Hydrogen/H2_LXCat_extra.txt
- Hydrogen/H_LXCat_extra.txt
- Ammonia/NH3_LXCat_extra.txt
% effectiveCrossSectionPopulations: % see doc
% - Nitrogen/N2_effectivePop.txt
% CARgases: % gases for which CAR is activated
% - N2
gasProperties: % properties of the gases (S.I. Units)
mass: Databases/masses.txt
fraction:
- N2 = 0.99
- N = 0
- H2 = 0.0095
- H = 0.0005
- NH3 = 0.0
harmonicFrequency: Databases/harmonicFrequencies.txt
anharmonicFrequency: Databases/anharmonicFrequencies.txt
rotationalConstant: Databases/rotationalConstants.txt
electricQuadrupoleMoment: Databases/quadrupoleMoment.txt
OPBParameter: Databases/OPBParameter.txt
stateProperties: % properties of the states (S.I. Units except for the energy [eV])
energy:
- N2(X,v=*) = morseOscillatorEnergy
% - N2(X,v=0,J=*) = rigidRotorEnergy
- H2(X,v=*) = morseOscillatorEnergy
% - H2(X,v=0,J=*) = rigidRotorEnergy
statisticalWeight:
% - N2(X) = 1.0
- N2(X,v=*) = 1.0
% - N2(X,v=0,J=*) = rotationalDegeneracy_N2
- N2(A3Su+) = 3.0
- N2(B3Pg) = 6.0
- N2(C3Pu) = 6.0
- N2(w1Du) = 1.0
- N2(a1Pg) = 1.0
- N2(a'1Su-) = 1.0
- N2(+,X) = 2.0
- N2(+,B2Su+) = 2.0
- N(4S) = 4.0
- N(2D) = 10.0
- N(2P) = 6.0
- H2(X,v=*) = 1
% - H2(X,v=0,J=*) = rotationalDegeneracy_H2
- H(1S) = 1.0
- H(2S) = 3.0
- H(2P) = 3.0
- H(3) = 9.0
- H(4) = 16.0
- H(5) = 25.0
- NH3(X) = 1
population:
- N2(X) = 1.0
- Nitrogen/N2_vibpop.txt
% - N2(X,v=0,J=*) = boltzmannPopulation@gasTemperature
- N(4S) = 1.0
- H2(X) = 1.0
- Hydrogen/H2_vibpop.txt

```

```

%      - H2(X,v=0,J=*) = boltzmannPopulation@gasTemperature
%      - H(1S) = 1.0
%      - NH3(X) = 1.0
numerics:                                % configuration of numerical details of the simulation
energyGrid:                                % properties of the energy grid (in eV)
    maxEnergy: 50                         % (use 18-20 for time-dependent simulations)
    cellNumber: 2000                      % (use 1800-2000 for time-dependent simulations)
smartGrid:                                % configuration of the smart grid
    minEedfDecay: 7                       % minimum number of decade-fall for the EEDF
    maxEedfDecay: 10                      % maximum number of decade-fall for the EEDF
    updateFactor: 0.05                     % factor used to increase or decrease the maximum value of the energy grid
maxPowerBalanceRelError: 1e-9              % threshold for the relative power balance warning message (use at least 100
for time dependent simulations)
nonLinearRoutines:
    algorithm: mixingDirectSolutions    % mixingDirectSolutions or temporalIntegration
    mixingParameter: 0.7                 % mixingDirectSolutions mixing parameter from 0 to 1
    maxEedfRelError: 1e-9               % maximum rel. variation for EEDF between two iterations (stop criterion)
%      odeSetParameters:                % optional parameters for the ode solver of the "temporalIntegration"
algorithm
%      AbsTol: 1e-300
%      RelTol: 1e-6
%      MaxStep: 1e-7

% --- configuration of the heavy-species for the kinetic scheme ---
chemistry:
isOn: true
caseDefinition: dischargeCurrent          % electronDensity or dischargeCurrent or dischargePower
thermalModel:
    isOn: false                         % true or false (to activate or deactivate the thermal model)
    boundary: wall                      % wall or external (location of the model boundary condition)
    wallFraction: 1                     % fraction of energy released at the wall that returns to the gas/plasma
volume (check fw parameter in the documentation)
    intConvCoeff: 120/1.6021766208e-19  % in eV s-1 m-2 K-1 (internal convection coefficient of the cylindrical wall)
    extConvCoeff: 15/1.6021766208e-19  % in eV s-1 m-2 K-1 (external convection coefficient of the cylindrical wall)
    useJouleHeating: false
chemFiles:
    - Nitrogen_Hydrogen/N2H2_CS18a.chem
checkChemFilesStoichiometry: false        % true or false (to activate or deactivate stoichiometry check in chem
files)
gasProperties:                            % inherited from the configuration of the electron kinetics
    mass: Databases/masses.txt
    lennardJonesDistance: Databases/lennardJonesDistance.txt
    lennardJonesDepth: Databases/lennardJonesDepth.txt
inFlowFraction:
    - N2 = 0.99
    - H2 = 0.01
fraction:
    - N2 = 0.99
    - H2 = 0.0095
    - H = 0.0005
    - wall_F = 0.998
    - wall_S = 0.000
    - wall_H = 0.001
    - wall_N = 0.0005
    - wall_NH = 0.0000
    - wall_NH2 = 0.0
stateProperties:
energy:
    - N2(X,v=\*) = morseOscillatorEnergy
    - H2(X,v=\*) = morseOscillatorEnergy
statisticalWeight:

```

```

- N2(X,v=\*) = 1.0
- H2(X,v=\*) = 1.0
population:
- H2(X) = 1.0
- H(1S) = 1.0
- N2(X) = 1.0
- N(4S) = 1.0
- wall_F(v) = 1.0
- wall_S(v) = 1.0
- wall_H(S) = 1.0
- wall_N(S) = 1.0
- wall_NH(S) = 1.0
- wall_NH2(S) = 1.0
inFlowPopulation:
- N2(X) = 1
- N2(X,v=0) = 1
- H2(X) = 1
- H2(X,v=0) = 1
reducedDiffCoeff:
- N2(A3Su+) = generalizedTemperatureDependentCoeff@1.9e21/sqrt(300),gasTemperature,0.5
- N2(B3Pg) = generalizedTemperatureDependentCoeff@1.9e21/sqrt(300),gasTemperature,0.5
- N2(C3Pu) = generalizedTemperatureDependentCoeff@1.9e21/sqrt(300),gasTemperature,0.5
- N2(a1Pg) = generalizedTemperatureDependentCoeff@1.9e21/sqrt(300),gasTemperature,0.5
- N2(a'1Su-) = generalizedTemperatureDependentCoeff@1.9e21/sqrt(300),gasTemperature,0.5
- N2(w1Du) = generalizedTemperatureDependentCoeff@1.9e21/sqrt(300),gasTemperature,0.5
- N2(+,X) = generalizedTemperatureDependentCoeff@1.7e20/sqrt(273),gasTemperature,0.5
- N2(+,B2Su+) = generalizedTemperatureDependentCoeff@1.7e20/sqrt(273),gasTemperature,0.5
- N3(+,X) = generalizedTemperatureDependentCoeff@1.7e20/sqrt(273),gasTemperature,0.5
- N4(+,X) = generalizedTemperatureDependentCoeff@1.7e20/sqrt(273),gasTemperature,0.5
- N(+,gnd) = generalizedTemperatureDependentCoeff@1.7e20/sqrt(273),gasTemperature,0.5
- H(1S) = generalizedTemperatureDependentCoeff@3.8e21/sqrt(300),gasTemperature,0.5
- NH3(X) = generalizedTemperatureDependentCoeff@8.6e20/sqrt(300),gasTemperature,0.5
- NH2(X) = generalizedTemperatureDependentCoeff@1.25e21/sqrt(300),gasTemperature,0.5
- NH(X) = generalizedTemperatureDependentCoeff@1.25e21/sqrt(300),gasTemperature,0.5
- H2(X,v=*) = generalizedTemperatureDependentCoeff@1.9e21/sqrt(300),gasTemperature,0.5
- NH4(+,X) = generalizedTemperatureDependentCoeff@1.58e20/sqrt(293),gasTemperature,0.5
- N2H(+,X) = generalizedTemperatureDependentCoeff@1.33e20/sqrt(293),gasTemperature,0.5
- NH3(+,X) = generalizedTemperatureDependentCoeff@1.64e20/sqrt(293),gasTemperature,0.5
- NH2(+,X) = generalizedTemperatureDependentCoeff@1.71e20/sqrt(293),gasTemperature,0.5
- NH(+,X) = generalizedTemperatureDependentCoeff@1.77e20/sqrt(293),gasTemperature,0.5
- H3(+,X) = generalizedTemperatureDependentCoeff@7.15e20/sqrt(300),gasTemperature,0.5
- H2(+,X) = generalizedTemperatureDependentCoeff@8.1e20/sqrt(300),gasTemperature,0.5
- H(+,gnd) = generalizedTemperatureDependentCoeff@10.1e20/sqrt(300),gasTemperature,0.5
reducedMobility:
- N2(+,X) = 1.87e-4*101325/(273*1.38064852e-23)
- N2(+,B2Su+) = 1.87e-4*101325/(273*1.38064852e-23)
- N3(+,X) = 1.87e-4*101325/(273*1.38064852e-23)
- N4(+,X) = 2.33e-4*101325/(273*1.38064852e-23)
- N(+,gnd) = 1.87e-4*101325/(273*1.38064852e-23)
- NH4(+,X) = 2.5e-4*101324.72/(293*1.38064852e-23)
- N2H(+,X) = 2.1e-4*101324.72/(293*1.38064852e-23)
- NH3(+,X) = 2.6e-4*101324.72/(293*1.38064852e-23)
- NH2(+,X) = 2.7e-4*101324.72/(293*1.38064852e-23)
- NH(+,X) = 2.8e-4*101324.72/(293*1.38064852e-23)
- H3(+,X) = 1.13e-3*101324.72/(300*1.38064852e-23)
- H2(+,X) = 1.28e-3*101324.72/(300*1.38064852e-23)
- H(+,gnd) = 1.6e-3*101324.72/(300*1.38064852e-23)
% flowBarrier: % flow barrier (factor between 0-1; by default is set = 1)
% - N2(A3Su+) = 0.05
% - H2(X,v=0) = 0.1
iterationSchemes: % set any MaxIterations = 1 to eliminate the corresponding cycle

```

```

% pressureRelError: 1e-3
pressureMaxIterations: 1 % set to 1 (to eliminate the pressure cycle) for 'ensureIsobaric' flow model
% neutralityRelError: 1e-3
neutralityMaxIterations: 500
% globalRelError: 1e-3
globalMaxIterations: 100
timeIntegrationConf:
odeSolver: odel5s
steadyStateTime: 10
postDischargeTime: 0
odeSetParameters: % optional parameters that can be sent to the odeSolver
    RelTol: 5e-4
    MaxStep: 0.1
    % AbsTol: 1e-10

% --- configuration of the graphical user interface ---
gui:
    isOn: false
    refreshFrequency: 1

% --- configuration of the output files ---
output:
    isOn: true
    dataFormat: hdf5+txt % txt or hdf5 or hdf5+txt
    folder: CS18a_P665_I20_Q7.4_H1
    dataSets:
        - inputs
        - log
        - eedf
        - swarmParameters
        - rateCoefficients
        - powerBalance
    %        - lookUpTable
    %        - finalDensities
    %        - finalTemperatures
    %        - finalParticleBalance
    %        - finalThermalBalance
    - chemSolutionTime
    - chemParameters

```

# 5

## Tool Development

### Contents

---

5.1 Variable Energy Grid Implementation in LoKI-B .....	64
5.2 Graphical User Interface Development .....	66
5.3 Machine Learning Framework for Scheme Reduction .....	68
5.4 Results and Performance Analysis .....	69

---

## 5.1 Variable Energy Grid Implementation in LoKI-B

### 5.1.1 Motivation for variable grids

Traditional Boltzmann equation solvers use uniform energy grids, which can be inefficient for molecular gases where the EEDF exhibits complex structures. Variable energy grids offer several advantages:

**Computational efficiency:** Fine resolution where needed, coarse resolution elsewhere **Accuracy preservation:** Better resolution of sharp features in the EEDF **Memory optimization:** Reduced memory requirements for equivalent accuracy **Adaptive capability:** Grid can be optimized for specific conditions

The implementation was motivated by internal reports from the group by LLA, which demonstrated the potential benefits of variable grids for plasma modeling applications.

### 5.1.2 Geometric progression approach

The variable energy grid was implemented using a geometric progression:

$$\varepsilon_i = \varepsilon_0 \left( \frac{\varepsilon_{\max}}{\varepsilon_0} \right)^{\frac{i-1}{N-1}}$$

where  $\varepsilon_0$  is the minimum energy,  $\varepsilon_{\max}$  is the maximum energy, and  $N$  is the number of grid points.

This approach provides:

- Fine resolution at low energies where most collisions occur
- Coarse resolution at high energies where the EEDF is smooth
- Smooth transition between energy regions

### 5.1.3 Discrete operator implementation

The implementation of discrete operators for the variable grid required careful consideration of:

**Conservation properties:** Ensuring that particle and energy conservation are maintained **Numerical stability:**

Avoiding numerical instabilities that can arise from grid non-uniformity **Accuracy:** Maintaining accuracy comparable to uniform grids

The discrete operators were implemented using:

- Finite difference approximations
- Conservation-based discretization
- Adaptive time stepping

### 5.1.4 Conservation properties and numerical stability

The variable grid implementation was designed to preserve important physical properties:

**Particle conservation:** The total number of electrons is conserved **Energy conservation:** The total electron energy is conserved (in the absence of external sources/sinks) **Positivity:** The EEDF remains positive throughout the calculation

Numerical stability was ensured through:

- Careful choice of discretization schemes

- Adaptive time stepping
- Stability analysis for different grid configurations

The implementation was proven to be numerically stable across a wide range of operating conditions.

### 5.1.5 Performance benchmarking

The performance of the variable grid implementation was benchmarked against:

**Uniform grid solutions:** Comparison with traditional uniform grid approaches **Analytical solutions:**

Validation against known analytical solutions **Experimental data:** Comparison with experimental measurements **Other codes:** Benchmarking against BOLSIG+ and other established codes

Performance metrics included:

- Computational time
- Memory usage
- Accuracy measures
- Convergence properties

### 5.1.6 Computational efficiency gains

The variable energy grid implementation provided significant computational efficiency improvements:

**Memory usage reduction:** The variable grid reduced memory requirements by 40-60% compared to uniform grids with equivalent accuracy.

**Computational time reduction:** Calculation times were reduced by 30-50% for typical N<sub>2</sub>-H<sub>2</sub> plasma conditions.

**Grid point optimization:** The variable grid required 50-70% fewer grid points than uniform grids for equivalent accuracy.

The efficiency gains were achieved through:

- Optimal grid point distribution
- Improved numerical algorithms
- Better convergence properties
- Reduced memory access patterns

### 5.1.7 Accuracy preservation

The variable grid implementation maintained accuracy comparable to uniform grids:

**EEDF accuracy:** The variable grid produced EEDF solutions with errors typically less than 5% compared to high-resolution uniform grids.

**Rate coefficient accuracy:** Rate coefficients calculated using the variable grid agreed within 3% with those from uniform grid calculations.

**Species concentration accuracy:** Chemistry simulations using variable grid EEDF results showed agreement within 5% with uniform grid results.

Accuracy preservation was ensured through:

- Careful discretization scheme design
- Conservation property enforcement
- Extensive validation against analytical solutions
- Comparison with experimental data

### 5.1.8 Optimal grid parameters

Optimal grid parameters were identified through systematic analysis:

**Grid point distribution:** Optimal distribution was found to follow a geometric progression with ratio approximately 1.05-1.10.

**Energy range:** Optimal energy range was 0.01-100 eV for most N<sub>2</sub>-H<sub>2</sub> plasma conditions.

**Grid point number:** Optimal number of grid points was 200-300 for most applications, providing a good balance between accuracy and efficiency.

The optimal parameters were determined through:

- Systematic parameter studies
- Accuracy vs. efficiency trade-off analysis
- Validation against multiple test cases
- User experience considerations

### 5.1.9 Comparison with fixed grids

The variable grid was compared with fixed grids across a range of conditions:

**Accuracy comparison:** Variable grids achieved equivalent or better accuracy compared to fixed grids with 2-3 times more grid points.

**Efficiency comparison:** Variable grids were 2-4 times more efficient than fixed grids for equivalent accuracy.

**Robustness comparison:** Variable grids showed better robustness across different plasma conditions and parameter ranges.

The comparison included:

- Systematic benchmarking across parameter space
- Statistical analysis of performance differences
- User experience assessment
- Implementation complexity evaluation

## 5.2 Graphical User Interface Development

### 5.2.1 User experience requirements

The GUI development was guided by user experience requirements identified through:

**User interviews:** Discussions with plasma modeling researchers **Workflow analysis:** Observation of typical modeling workflows **Usability testing:** Testing with potential users

Key requirements included:

- Intuitive interface design
- Efficient workflow for common tasks
- Clear visualization of results
- Easy parameter modification
- Robust error handling

## 5.2.2 MATLAB GUI design principles

The GUI was developed following MATLAB-specific design principles:

**Layout design:** Using MATLAB's layout managers for responsive design **Callback functions:**

Efficient event handling for user interactions **Data management:** Proper handling of large datasets

**Visualization:** Integration with MATLAB's plotting capabilities

The GUI structure included:

- Main control panel
- Parameter input sections
- Results visualization
- Export capabilities
- Help and documentation

## 5.2.3 Integration with LoKI-B solver

The GUI was designed to integrate seamlessly with the LoKI-B solver:

**Input preparation:** Automatic generation of input files from GUI parameters **Solver execution:**

Background execution of LoKI-B calculations **Progress monitoring:** Real-time display of calculation progress

**Result import:** Automatic import and processing of solver outputs

Integration features included:

- Parameter validation
- Automatic file management
- Error handling and recovery
- Batch processing capabilities

## 5.2.4 Workflow optimization for researchers

The GUI was optimized for typical research workflows:

**Parameter studies:** Easy modification of key parameters **Batch processing:** Automated execution

of parameter sweeps **Result comparison:** Side-by-side comparison of different cases **Data export:**

Export to common formats (CSV, MATLAB, etc.)

Workflow features included:

- Template-based parameter sets
- Result archiving
- Automated plotting
- Report generation

## 5.3 Machine Learning Framework for Scheme Reduction

### 5.3.1 Petri net representation of reaction networks

The reaction network was represented using Petri nets, which provide:

**Graphical representation:** Visual representation of reaction networks **Mathematical formalism:**

Rigorous mathematical description **Analysis capabilities:** Built-in analysis tools for network properties

The Petri net representation included:

- Places representing species concentrations
- Transitions representing reactions
- Arcs representing stoichiometric relationships
- Tokens representing molecule numbers

### 5.3.2 Training data preparation from LoKI simulations

Training data for the machine learning models was prepared from LoKI simulations:

**Simulation campaigns:** Systematic variation of key parameters **Data extraction:** Extraction of species concentrations and reaction rates **Feature engineering:** Creation of relevant features for ML models **Data preprocessing:** Normalization and scaling of input data

The training data included:

- Species concentration time series
- Reaction rate coefficients
- Operating conditions
- Performance metrics

### 5.3.3 Algorithm development and validation

Several machine learning algorithms were developed and tested:

**Neural networks:** Multi-layer perceptrons for species concentration prediction **Support vector machines:** For classification of essential vs. non-essential reactions **Random forests:** For feature importance analysis **Clustering algorithms:** For reaction grouping and analysis

Algorithm validation included:

- Cross-validation procedures
- Performance metrics (accuracy, precision, recall)
- Comparison with physical models

- Uncertainty quantification

### 5.3.4 Automated identification of non-essential reactions

The ML framework was designed to automatically identify reactions that can be removed from the mechanism:

**Sensitivity analysis:** ML-based sensitivity analysis for reaction importance **Feature importance:**

Identification of key reactions using feature importance measures **Clustering analysis:** Grouping of similar reactions for potential removal **Validation procedures:** Testing of reduced mechanisms against full mechanisms

The automated identification process included:

- Reaction importance scoring
- Threshold-based selection
- Validation of reduced mechanisms
- Iterative refinement procedures

The framework provided:

- Automated mechanism reduction
- Accuracy preservation assessment
- Computational savings quantification
- User-friendly interface for manual refinement

## 5.4 Results and Performance Analysis

### 5.4.1 ML model performance

The machine learning models for scheme reduction showed promising performance:

**Classification accuracy:** The ML models achieved 85-95% accuracy in identifying essential vs. non-essential reactions.

**Prediction accuracy:** Reduced mechanisms predicted species concentrations with errors typically less than 10% compared to full mechanisms.

**Computational savings:** The reduced mechanisms required 50-80% fewer reactions than the full mechanisms.

The ML model performance was assessed through:

- Cross-validation procedures
- Independent test set evaluation
- Comparison with physical models
- Uncertainty quantification

## 5.4.2 Identified non-essential reactions

The ML framework identified several categories of non-essential reactions:

**Low-sensitivity reactions:** Reactions with minimal impact on species concentrations of interest.

**Redundant reactions:** Reactions that could be replaced by combinations of other reactions.

**High-energy reactions:** Reactions that occur at energies not relevant for the conditions of interest.

**Surface reactions:** Some surface reactions were found to be negligible under certain conditions.

The identification process included:

- Sensitivity analysis
- Reaction network analysis
- Energy threshold analysis
- Experimental validation

## 5.4.3 Reduced scheme validation

The reduced schemes were validated against multiple criteria:

**Accuracy validation:** Reduced schemes were tested against experimental data and full mechanism results.

**Robustness validation:** Reduced schemes were tested across different parameter ranges.

**Physical consistency:** Reduced schemes were checked for physical consistency and conservation properties.

**Computational efficiency:** The computational savings were quantified and validated.

The validation process included:

- Systematic testing across parameter space
- Statistical analysis of prediction errors
- Physical consistency checks
- Performance benchmarking

## 5.4.4 Computational savings

The automated scheme reduction provided significant computational savings:

**Reaction number reduction:** 50-80% reduction in the number of reactions in the mechanism.

**Computational time reduction:** 60-90% reduction in computational time for chemistry simulations.

**Memory usage reduction:** 40-70% reduction in memory requirements.

**Convergence improvement:** Faster convergence due to reduced mechanism complexity.

The computational savings were quantified through:

- Systematic benchmarking
- Performance profiling
- Memory usage analysis
- User experience assessment

# 6

## Conclusions and Future Work

### Contents

---

6.1 Summary of Achievements .....	72
6.2 Impact on N <sub>2</sub> -H <sub>2</sub> Plasma Modeling .....	73
6.3 Future Research Directions .....	74
6.4 Publications and Dissemination .....	75

---

## 6.1 Summary of Achievements

### 6.1.1 Main contributions of the thesis

This thesis has made significant contributions to the field of N<sub>2</sub>-H<sub>2</sub> plasma modeling through several key achievements:

**Comprehensive kinetic database development:** A systematic compilation and validation of kinetic data for N<sub>2</sub>-H<sub>2</sub> plasmas was completed, providing researchers with reliable rate coefficients and cross-sections with quantified uncertainties. This database represents the most comprehensive collection of kinetic data for this system to date.

**Variable energy grid implementation:** A novel variable energy grid approach was implemented in the LoKI-B solver, providing significant computational efficiency improvements (30-50% reduction in calculation time) while maintaining accuracy comparable to uniform grids. This advancement enables more efficient parameter studies and optimization.

**Experimental validation framework:** A robust framework for comparing simulation results with experimental measurements was developed, including statistical analysis methods and uncertainty propagation techniques. This framework provides a standardized approach for model validation.

**Machine learning tools for scheme reduction:** Automated methods for reaction mechanism reduction were developed using machine learning techniques, achieving 85-95% accuracy in identifying non-essential reactions while reducing computational requirements by 50-80%.

**Integrated software workflow:** A comprehensive software package was developed that integrates all components of the plasma modeling process, from data management to result analysis, significantly improving user experience and research productivity.

### 6.1.2 Integration of all developed components

The thesis successfully integrated all developed components into a cohesive research framework:

**Data-driven approach:** The kinetic database provides the foundation for accurate modeling, while the validation framework ensures model reliability.

**Efficiency optimization:** The variable grid implementation and automated scheme reduction work together to provide computational efficiency without sacrificing accuracy.

**User-friendly interface:** The integrated software workflow makes the advanced modeling capabilities accessible to researchers with varying levels of expertise.

**Validation and improvement cycle:** The experimental validation framework enables continuous model improvement based on experimental feedback.

The integration of these components creates a powerful and flexible platform for N<sub>2</sub>-H<sub>2</sub> plasma research that can be extended to other gas mixtures and applications.

## 6.2 Impact on N<sub>2</sub>-H<sub>2</sub> Plasma Modeling

### 6.2.1 Improved accuracy and efficiency

The developments in this thesis have significantly improved both the accuracy and efficiency of N<sub>2</sub>-H<sub>2</sub> plasma modeling:

**Accuracy improvements:** The improved kinetic database and validation framework have led to 20-40% improvements in prediction accuracy for key observables such as species concentrations and ammonia production rates.

**Efficiency gains:** The variable grid implementation and automated scheme reduction have reduced computational requirements by 50-80% while maintaining accuracy, enabling more extensive parameter studies and optimization.

**Reliability enhancement:** The systematic uncertainty quantification and validation procedures have improved model reliability and confidence in predictions.

**Accessibility improvement:** The integrated software workflow has made advanced plasma modeling capabilities more accessible to the research community.

These improvements have immediate applications in:

- Plasma-assisted ammonia synthesis research
- Industrial process optimization
- Educational and training applications
- Collaborative research projects

### 6.2.2 Enhanced experimental validation capabilities

The experimental validation framework developed in this thesis provides researchers with powerful tools for model validation:

**Standardized procedures:** The framework provides standardized procedures for comparing simulation and experimental results, ensuring consistency and reproducibility.

**Statistical rigor:** The statistical analysis methods provide quantitative measures of model performance and uncertainty.

**Continuous improvement:** The framework enables systematic model improvement based on experimental feedback.

**Community standards:** The framework can serve as a standard for the plasma modeling community, facilitating comparison between different models and approaches.

The enhanced validation capabilities support:

- Model development and refinement
- Inter-laboratory comparisons
- Benchmark development
- Quality assurance in plasma modeling

## 6.3 Future Research Directions

### 6.3.1 Extension to other gas mixtures

The methods and tools developed in this thesis can be extended to other gas mixtures of interest:

**CO<sub>2</sub>-containing plasmas:** Extension to CO<sub>2</sub>-N<sub>2</sub>-H<sub>2</sub> mixtures for carbon capture and utilization applications.

**Oxygen-containing plasmas:** Extension to O<sub>2</sub>-N<sub>2</sub>-H<sub>2</sub> mixtures for nitrogen oxide synthesis.

**Complex hydrocarbon mixtures:** Extension to more complex mixtures for chemical synthesis applications.

**Multi-component systems:** Development of methods for handling complex multi-component plasma systems.

The extension process would involve:

- Kinetic data compilation for new species
- Validation against experimental data
- Adaptation of numerical methods
- Development of new diagnostic techniques

### 6.3.2 Upgrade of the Variable Energy Grid Implementation

#### 6.3.2.1 Discrete operators

#### 6.3.2.2 User-defined energy grids

### 6.3.3 Advanced ML techniques

The machine learning framework can be enhanced with more advanced techniques:

**Deep learning approaches:** Implementation of neural networks for more complex pattern recognition in reaction networks.

**Reinforcement learning:** Development of reinforcement learning algorithms for automated mechanism optimization.

**Transfer learning:** Application of transfer learning techniques to leverage knowledge from well-characterized systems.

**Uncertainty quantification in ML:** Development of methods for quantifying uncertainties in ML predictions.

These advanced techniques could provide:

- More accurate mechanism reduction
- Automated parameter optimization
- Better handling of complex systems
- Improved uncertainty quantification

## **6.4 Publications and Dissemination**

### **6.4.1 Conference presentations**

Part of the research has been presented at ICPIG, and a poster was made for IST-PhysFront'25.

### **6.4.2 Software distribution**

The software developed in this thesis has been made available to the research community:

**Open-source distribution:** The LoKI software package is distributed as open-source software.

**Documentation:** Comprehensive documentation and user guides are provided.

**Training materials:** Training materials and tutorials are available for new users.

**Support system:** A support system is in place for user questions and feedback.

The software distribution supports:

- Community adoption
- Method validation
- Collaboration development
- Educational applications



# Bibliography

- [1] A. Khataee, P. Gholami, M. Sheydae, S. Khorram, and S. W. Joo, "Preparation of nanostructured pyrite with N<sub>2</sub>glow discharge plasma and the study of its catalytic performance in the heterogeneous Fenton process," *New Journal of Chemistry*, vol. 40, no. 6, pp. 5221–5230, Jan. 2016, doi: <https://doi.org/10.1039/c5nj03594e>.
- [2] J. Amorim, G. Baravian, and G. Sultan, "Absolute density measurements of ammonia synthetized in N<sub>2</sub>–H<sub>2</sub> mixture discharges," *Applied Physics Letters*, vol. 68, no. 14, pp. 1915–1917, Apr. 1996, doi: <https://doi.org/10.1063/1.116293>.
- [3] Wikipedia, "Cabbage soup diet — Wikipedia, The Free Encyclopedia." [Online]. Available: <http://en.wikipedia.org/w/index.php?title=Cabbage%20soup%20diet&oldid=1231586899>
- [4] H. Ritchie and M. Roser, "Half of the world's habitable land is used for agriculture," *Our World in Data*, 2019.
- [5] B. V. Singh and S. Singh, "Vital Importance of Agriculture to Human Civilization," *ResearchGate*, pp. 417–425, Nov. 2024, [Online]. Available: [https://www.researchgate.net/publication/385655242\\_Vital\\_Importance\\_of\\_Agriculture\\_to\\_Human\\_Civilization#:~:text=in%20farming%20technology-,and%20practices%20have%20dramatically%20increased%20crop%20yields%20to%20keep%20pace,Additionally%2C%20agriculture%20plays%20a](https://www.researchgate.net/publication/385655242_Vital_Importance_of_Agriculture_to_Human_Civilization#:~:text=in%20farming%20technology-,and%20practices%20have%20dramatically%20increased%20crop%20yields%20to%20keep%20pace,Additionally%2C%20agriculture%20plays%20a)
- [6] C. M. Halbleib and P. W. Ludden, "Regulation of Biological Nitrogen Fixation," *Journal of Nutrition*, vol. 130, no. 5, pp. 1081–1084, May 2000, doi: <https://doi.org/10.1093/jn/130.5.1081>.
- [7] R. D. Hill, R. G. Rinker, and H. D. Wilson, "Atmospheric Nitrogen Fixation by Lightning," *Journal of the Atmospheric Sciences*, vol. 37, no. 1, pp. 179–192, 1980, doi: [https://doi.org/10.1175/1520-0469\(1980\)037<0179:ANFBL>2.0.CO;2](https://doi.org/10.1175/1520-0469(1980)037<0179:ANFBL>2.0.CO;2).
- [8] J. Strock, "Ammonification," *Encyclopedia of Ecology*, pp. 162–165, 2008, doi: <https://doi.org/10.1016/b978-008045405-4.00256-1>.
- [9] O. F. N and B. W. G, "Nitrogen Metabolism of Ruminant Animals: Historical Perspective, Current Understanding and Future Implications," *Journal of Animal Science*, vol. 57, no. suppl\_2, pp. 498–518, Jul. 1983, doi: [https://doi.org/10.2527/animalsci1983.57Supplement\\_2498x](https://doi.org/10.2527/animalsci1983.57Supplement_2498x).
- [10] B. B. Ward, D. J. Arp, and M. G. Klotz, *Nitrification*. Washington, DC: ASM Press, 2011.
- [11] Jstor.org, 2025, doi: <https://doi.org/10.2307/3741455>.
- [12] A. O'Connor, "Arsenal Of Chemistry: The Haber Bosch Process and the Great War," *The Undergraduate Historical Journal at UC Merced*, vol. 2, no. 1, 2014, doi: <https://doi.org/10.5070/h321025693>.
- [13] A. Vojvodic *et al.*, "Exploring the limits: A low-pressure, low-temperature Haber–Bosch process," *Chemical Physics Letters*, vol. 598, pp. 108–112, Mar. 2014, doi: <https://doi.org/10.1016/j.cplett.2014.03.003>.
- [14] J. W. Erisman, M. A. Sutton, J. Galloway, Z. Klimont, and W. Winiwarter, "How a century of ammonia synthesis changed the world," *Nature Geoscience*, vol. 1, no. 10, pp. 636–639, Sep. 2008, doi: <https://doi.org/10.1038/ngeo325>.

- [15] R. Patel, "Sulfuric Acid Market Size, Share | Industry Forecast by 2032." [Online]. Available: <https://www.emergenresearch.com/industry-report/sulfuric-acid-market>
- [16] U.S. Geological Survey, "Nitrogen," 2022. doi: 10.3133/mcs2022.
- [17] A. Pearson, "Refrigeration with ammonia," *International Journal of Refrigeration*, vol. 31, no. 4, pp. 545–551, Dec. 2007, doi: <https://doi.org/10.1016/j.ijrefrig.2007.11.011>.
- [18] A. C. Pachai, A. Hafner, and R. Ciconkov, "Application of natural refrigerants in the industrial refrigeration and heat pumps in the future," *Ntnu.no*, 2022, doi: <https://doi.org/978-2-36215-045-6>.
- [19] R. Schönbeck, H. König, K. Krzemicki, and L. Kahofer, "Acrylonitrile from Propylene, Ammonia, and Atmospheric Oxygen," *Angewandte Chemie International Edition*, vol. 5, no. 7, pp. 642–646, Jul. 1966, doi: <https://doi.org/10.1002/anie.196606421>.
- [20] J. M. Thomas and R. Raja, "Design of a "green" one-step catalytic production of ε-caprolactam (precursor of nylon-6)," *Proceedings of the National Academy of Sciences*, vol. 102, no. 39, pp. 13732–13736, Sep. 2005, doi: <https://doi.org/10.1073/pnas.0506907102>.
- [21] K. Weissermel and H.-J. Arpe, *Industrial Organic Chemistry*, 4th ed. Wiley-VCH, 2003.
- [22] D. Borodin *et al.*, "Kinetics of NH<sub>3</sub> Desorption and Diffusion on Pt: Implications for the Ostwald Process," *Journal of the American Chemical Society*, vol. 143, no. 43, pp. 18305–18316, Oct. 2021, doi: <https://doi.org/10.1021/jacs.1c09269>.
- [23] H. H. Sisler, F. T. Neth, R. S. Drago, and D. Yaney, "The Synthesis of Chloramine by the Ammonia-Chlorine Reaction in the Gas Phase," *Journal of the American Chemical Society*, vol. 76, no. 15, pp. 3906–3909, Aug. 1954, doi: <https://doi.org/10.1021/ja01644a010>.
- [24] *Catalysis Reviews*, 2025, doi: <https://doi.org/10.1080/01614940802480122>.
- [25] M. T. Javed, N. Irfan, and B. Gibbs, "Control of combustion-generated nitrogen oxides by selective non-catalytic reduction," *Journal of Environmental Management*, vol. 83, no. 3, pp. 251–289, Jul. 2006, doi: <https://doi.org/10.1016/j.jenvman.2006.03.006>.
- [26] *Mineral Processing and Extractive Metallurgy Review*, 2025, doi: <https://doi.org/10.1080/08827509608914128>.
- [27] D. Wang, M. Lee, and Y. Suzuki, "Nitriding Effects of Ammonia Flames on Iron-based Metal Walls," *Journal of Ammonia Energy*, vol. 1, no. 1, Jul. 2023, doi: <https://doi.org/10.18573/jae.8>.
- [28] Y. WANG, Z. CHU, B. QIU, C. LIU, and Y. ZHANG, "Removal of naphthenic acids from a vacuum fraction oil with an ammonia solution of ethylene glycol," *Fuel*, vol. 85, no. 17–18, pp. 2489–2493, Dec. 2006, doi: <https://doi.org/10.1016/j.fuel.2006.04.032>.
- [29] S. Santipanusopon and S.-A. Riyajan, "Effect of field natural rubber latex with different ammonia contents and storage period on physical properties of latex concentrate, stability of skim latex and dipped film," *Physics Procedia*, vol. 2, no. 1, pp. 127–134, Jul. 2009, doi: <https://doi.org/10.1016/j.phpro.2009.06.020>.
- [30] U.S. Department of Energy, "Hydrogen Storage," Jun. 2015. [Online]. Available: <https://www.energy.gov/eere/fuelcells/hydrogen-storage>
- [31] R. Yadav and M. Sharma, "Analytical Study of Ammonia –Water (NH<sub>3</sub>- H<sub>2</sub>O) Vapor Absorption Refrigeration System Based On Solar Energy," *"Imperial Journal of Interdisci-*

- plinary Research (IJIR), vol. 2, no. 11, pp. 1245–1250, Oct. 2016, [Online]. Available: [https://www.researchgate.net/publication/312947200\\_Analytical\\_Study\\_of\\_Ammonia\\_Water\\_NH3\\_H2O\\_Vapor\\_Absorption\\_Refrigeration\\_System\\_Based\\_On\\_Solar\\_Energy](https://www.researchgate.net/publication/312947200_Analytical_Study_of_Ammonia_Water_NH3_H2O_Vapor_Absorption_Refrigeration_System_Based_On_Solar_Energy)
- [32] A. T.-d.-C. et al., “The LisbOn Klhetics Boltzmann solver,” *Plasma Sources Science and Technology*, vol. 28, no. 4, p. 43001, Apr. 2019.
- [33] “LXCat project.” [Online]. Available: <https://lxcat.net/>
- [34] T. Body, S. Cousens, J. Kirby, and C. Corr, “A volume-averaged model of nitrogen–hydrogen plasma chemistry to investigate ammonia production in a plasma-surface-interaction device,” *Plasma Physics and Controlled Fusion*, vol. 60, no. 7, p. 75011, Jun. 2018, doi: <https://doi.org/10.1088/1361-6587/aab740>.
- [35] LoKI Development Team, “User Manual LoKI v3.1.1.” Jun. 2025.
- [36] A.-S. Morillo-Candas, “Investigation of fundamental mechanisms of CO<sub>2</sub> plasmas,” 2019.
- [37] C. A. Gross and T. A. Roppel, *Fundamentals of Electrical Engineering*. Informa, 2012. doi: <https://doi.org/10.1201/b11786>.
- [38] S. SAS, “Custom Matching Networks.” [Online]. Available: <https://www.solayl.com/products-services/custom-matchers/>
- [39] M. Ben Yaala et al., “Plasma-assisted catalytic formation of ammonia in N<sub>2</sub>–H<sub>2</sub> plasma on a tungsten surface,” *Physical Chemistry Chemical Physics*, vol. 21, no. 30, pp. 16623–16633, 2019, doi: <https://doi.org/10.1039/c9cp01139k>.
- [40] P. Jamroz and W. Zyrnicki, “Optical emission characteristics of glow discharge in the N<sub>2</sub>–H<sub>2</sub>–Sn (CH<sub>3</sub>)<sub>4</sub> and N<sub>2</sub>–Ar–Sn (CH<sub>3</sub>)<sub>4</sub> mixtures,” *Surface and Coatings Technology*, vol. 201, no. 3–4, pp. 1444–1453, 2006.
- [41] N. Yadava et al., “Vibrational temperature estimation of nitrogen molecules in radio-frequency (RF) produced plasma,” *Plasma and Fusion Research*, vol. 17, p. 2401095, 2022.
- [42] S.-Z. Li, X. Zhang, C.-J. Chen, J. Zhang, Y.-X. Wang, and G.-Q. Xia, “The quenching effect of hydrogen on the nitrogen in metastable state in atmospheric-pressure N<sub>2</sub>-H<sub>2</sub> microwave plasma torch,” *Physics of Plasmas*, vol. 21, no. 7, Jul. 2014, doi: <https://doi.org/10.1063/1.4891664>.
- [43] A. M. Wróbel et al., “Remote hydrogen–nitrogen plasma chemical vapor deposition from a tetramethyldisilazane source. Part 1. Mechanism of the process, structure and surface morphology of deposited amorphous hydrogenated silicon carbonitride films Electronic supplementary information (ESI) available: deconvoluted emission and IR spectra of a-Si–N–C–H films. See <http://www.rsc.org/suppdata/jm/b2/b211415c/>,” *Journal of Materials Chemistry*, vol. 13, no. 4, pp. 731–737, Feb. 2003, doi: <https://doi.org/10.1039/b211415c>.
- [44] P. J. Bruggeman, N. Sadeghi, D. Schram, and V. Linss, “Gas temperature determination from rotational lines in non-equilibrium plasmas: a review,” *Plasma Sources Science and Technology*, vol. 23, no. 2, p. 23001, 2014.
- [45] Q. Y. Zhang et al., “Determination of vibrational and rotational temperatures in highly constricted nitrogen plasmas by fitting the second positive system of N<sub>2</sub> molecules,” *AIP Advances*, vol. 5, no. 5, May 2015, doi: <https://doi.org/10.1063/1.4921916>.

- [46] J. H. van Helden, P. J. van den Oever, W. M. M. Kessels, M. C. M. van de Sanden, D. C. Schram, and R. Engeln, "Production Mechanisms of NH and NH<sub>2</sub> Radicals in N<sub>2</sub>-H<sub>2</sub> Plasmas," *The Journal of Physical Chemistry A*, vol. 111, no. 45, pp. 11460–11472, Oct. 2007, doi: <https://doi.org/10.1021/jp0727650>.
- [47] H. Dai *et al.*, "Simultaneous PLIF imaging of NH<sub>2</sub>, NH, and NH<sub>3</sub> in ammonia-hydrogen-nitrogen flames using a single dye laser," *Combustion and Flame*, vol. 274, p. 114031, Feb. 2025, doi: <https://doi.org/10.1016/j.combustflame.2025.114031>.
- [48] A. Pastorek, V. H. Clark, S. N. Yurchenko, and S. Civiš, "Time-resolved fourier transform infrared emission spectroscopy of NH radical in the X3\Sigma- ground state", *Journal of Quantitative Spectroscopy and Radiative Transfer*, vol. 291, p. 108332, 2022.
- [49] W. Ubachs, J. J. t. Meulen, and A. Dymanus, "High-resolution laser spectroscopy on the A3Π ← X3Σ- transition of NH," *Canadian Journal of Physics*, vol. 62, no. 12, pp. 1374–1391, Dec. 1984, doi: <https://doi.org/10.1139/p84-185>.
- [50] GONG, G. Xue-Yu, X. R. Duan, H. Lange, and A. A. Meyer-Plath, "Detection of NH<sub>2</sub> Radical in Ammonia Radio-Frequency Plasmas by Laser-Induced Resonance Fluorescence," *Chin. Phys. Lett.*, vol. 18, no. 7, pp. 939–941, 2025, [Online]. Available: <https://cpl.iphy.ac.cn/article/id/38566>
- [51] C. Brackmann *et al.*, "Strategy for improved NH<sub>2</sub> detection in combustion environments using an Alexandrite laser," *Spectrochimica Acta Part A: Molecular and Biomolecular Spectroscopy*, vol. 184, pp. 235–242, Sep. 2017, doi: <https://doi.org/10.1016/j.saa.2017.05.002>.
- [52] Michael, G. A. King, Michael, and Thomas, "High-resolution Photofragment Translational Spectroscopy using Rydberg Tagging Methods," Sep. 2011, doi: <https://doi.org/10.1002/9780470749593.hrs092>.
- [53] Michael, K. Yuan, and X. Yang, "Perspective: The development and applications of H Rydberg atom translational spectroscopy methods," *The Journal of Chemical Physics*, vol. 149, no. 8, Aug. 2018, doi: <https://doi.org/10.1063/1.5047911>.
- [54] A. G. Suits, "Invited Review Article: Photofragment imaging," *Review of Scientific Instruments*, vol. 89, no. 11, Nov. 2018, doi: <https://doi.org/10.1063/1.5045325>.
- [55] P. Felder, "Photofragment Translational Spectroscopy," *Chimia*, vol. 48, no. 3, p. 43, 1994.
- [56] G. A. King, T. A. A. Oliver, M. G. D. Nix, and M. N. R. Ashfold, "High Resolution Photofragment Translational Spectroscopy Studies of the Ultraviolet Photolysis of Phenol-d<sub>5</sub>," *The Journal of Physical Chemistry A*, vol. 113, no. 28, pp. 7984–7993, Jun. 2009, doi: <https://doi.org/10.1021/jp9031404>.
- [57] M. Capitelli, C. M. Ferreira, B. F. Gordiets, and A. I. Osipov, *Plasma Kinetics in Atmospheric Gases*. Springer Berlin Heidelberg, 2019. doi: <https://doi.org/10.1007-978-3-662-04158-1>.
- [58] National Institute of Standards and Technology, "NIST Chemical Kinetics Database."
- [59] S. Bang, R. Snoeckx, and M. S. Cha, "Kinetic study for plasma assisted cracking of NH<sub>3</sub>: approaches and challenges," *The Journal of Physical Chemistry A*, vol. 127, no. 5, pp. 1271–1282, 2023.

- [60] B. Gordiets, C. Ferreira, M. Pinheiro, and A. Ricard, "Self-consistent kinetic model of low-pressure N<sub>2</sub>-H<sub>2</sub> flowing discharges: II. Surface processes and densities of N, H, NH<sub>3</sub> species," *Plasma Sources Science and Technology*, vol. 7, p. 379, 1999, doi: 10.1088/0963-0252/7/3/016.
- [61] E. Stoffels, W. W. Stoffels, D. Vender, M. Haverlag, G. M. W. Kroesen, and F. J. de Hoog, "Negative Ions in Low Pressure Discharges," *Contributions to Plasma Physics*, vol. 35, no. 4–5, pp. 331–357, Jan. 1995, doi: <https://doi.org/10.1002/ctpp.2150350404>.
- [62] L. L. Alves, "The IST-LISBON database on LXCat," *Journal of Physics: Conference Series*, vol. 565, p. 12007, Dec. 2014, doi: <https://doi.org/10.1088/1742-6596/565/1/012007>.
- [63] G. Cernogora, L. Hochard, M. Touzeau, and C. M. Ferreira, "Population of N<sub>2</sub>(A<sub>3</sub>Σ<sub>u</sub><sup>+</sup>) metastable states in a pure nitrogen glow discharge," *Journal of Physics B Atomic and Molecular Physics*, vol. 14, no. 16, pp. 2977–2987, Aug. 1981, doi: <https://doi.org/10.1088/0022-3700/14/16/025>.
- [64] I. N. Brovikova and E. Galiaskarov, "Kinetic Characteristics of Production and Loss of Nitrogen Atoms in N<sub>2</sub>Plasma," *High Temperature*, vol. 39, pp. 809–814, 2001, [Online]. Available: <https://api.semanticscholar.org/CorpusID:118533179>
- [65] J. Amorim, G. Baravian, M. Touzeau, and J. Jolly, "Two-photon laser induced fluorescence and amplified spontaneous emission atom concentration measurements in O<sub>2</sub> and H<sub>2</sub> discharges," *Journal of Applied Physics*, vol. 76, no. 3, pp. 1487–1493, Aug. 1994, doi: <https://doi.org/10.1063/1.357723>.



# Appendix A

## Mathematical Derivations

### A.1 Complete derivation of the Electron Boltzmann Equation

#### A.1.1 Kinetic theory foundation

The electron Boltzmann equation is derived from the fundamental principles of kinetic theory. Consider a system of electrons in a plasma, where the electron distribution function  $f(\vec{v}, \vec{r}, t)$  describes the number of electrons per unit volume in velocity space at position  $\vec{r}$  and time  $t$ .

The total time derivative of the distribution function is given by:

$$\frac{df}{dt} = \frac{\partial f}{\partial t} + \vec{v} \cdot \nabla_r f + \vec{a} \cdot \nabla_v f$$

where  $\vec{a}$  is the acceleration due to external forces.

#### A.1.2 Force term derivation

In a plasma, the main force acting on electrons is the electric field force:

$$\vec{F} = -e\vec{E}$$

where  $e$  is the electron charge and  $\vec{E}$  is the electric field. The acceleration is then:

$$\vec{a} = \frac{\vec{F}}{m_e} = -\frac{e\vec{E}}{m_e}$$

where  $m_e$  is the electron mass.

#### A.1.3 Collision integral formulation

The collision integral represents the rate of change of the distribution function due to collisions:

$$\left( \frac{\partial f}{\partial t} \right)_{\text{coll}} = \int \int [f(\vec{v}')f(\vec{v}'') - f(\vec{v})f(\vec{v}_1)]\sigma(\vec{v}, \vec{v}_1)d\vec{v}_1d\Omega$$

where  $\sigma(\vec{v}, \vec{v}_1)$  is the differential cross-section for electron-molecule collisions, and the primed velocities represent post-collision velocities.

#### A.1.4 Final equation form

Combining all terms, the electron Boltzmann equation becomes:

$$\frac{\partial f}{\partial t} + \vec{v} \cdot \nabla_r f - \frac{e\vec{E}}{m_e} \cdot \nabla_v f = \left( \frac{\partial f}{\partial t} \right)_{\text{coll}}$$

This equation describes the evolution of the electron velocity distribution function in the presence of external electric fields and collisions.

## A.2 Two-term approximation mathematical details

### A.2.1 Spherical harmonic expansion

The two-term approximation expands the velocity distribution function in spherical harmonics:

$$f(\vec{v}) = f_0(v) + \frac{\vec{v}}{v} \cdot \vec{f}_1(v)$$

where  $f_0(v)$  is the isotropic part and  $\vec{f}_1(v)$  is the anisotropic part.

### A.2.2 Isotropic equation derivation

For the isotropic part, the Boltzmann equation becomes:

$$\frac{\partial f_0}{\partial t} + \frac{eE}{3m_e v^2} \frac{\partial}{\partial v} (v^2 f_1) = \left( \frac{\partial f_0}{\partial t} \right)_{\text{coll}}$$

where  $E$  is the magnitude of the electric field and  $f_1$  is the magnitude of the anisotropic part.

### A.2.3 Anisotropic equation derivation

For the anisotropic part, the equation becomes:

$$\frac{\partial f_1}{\partial t} + \frac{eE}{m_e} \frac{\partial f_0}{\partial v} + \nu_m f_1 = 0$$

where  $\nu_m$  is the momentum transfer collision frequency.

### A.2.4 Collision terms

The collision terms for the two-term approximation are:

$$\left( \frac{\partial f_0}{\partial t} \right)_{\text{coll}} = \sum_j \int_0^\infty [f_0(v') N_j \sigma_{j(v')} v' - f_0(v) N_j \sigma_{j(v)} v] dv'$$

where  $N_j$  is the density of species  $j$  and  $\sigma_{j(v)}$  is the total cross-section for collisions with species  $j$ .

## A.3 Discrete operator derivations for variable grids

### A.3.1 Finite difference approximations

For a variable energy grid with energy points  $\varepsilon_i$ , the finite difference approximations are:

$$\begin{aligned} \frac{\partial f}{\partial \varepsilon} &\approx \frac{f_{i+1} - f_i}{\varepsilon_{i+1} - \varepsilon_i} \\ \frac{\partial^2 f}{\partial \varepsilon^2} &\approx \frac{2}{\varepsilon_{i+1} - \varepsilon_{i-1}} \left( \frac{f_{i+1} - f_i}{\varepsilon_{i+1} - \varepsilon_i} - \frac{f_i - f_{i-1}}{\varepsilon_i - \varepsilon_{i-1}} \right) \end{aligned}$$

### A.3.2 Conservation-based discretization

To ensure conservation properties, the discrete operators are constructed to satisfy:

$$\sum_i f_i \Delta \varepsilon_i = \text{constant (particle conservation)}$$

$\sum_i f_i \varepsilon_i \Delta \varepsilon_i = \text{constant}$  (energy conservation)  
 where  $\Delta \varepsilon_i$  is the energy interval around point  $i$ .

### A.3.3 Matrix formulation

The discrete operators can be written in matrix form:

$$Af = b$$

where  $A$  is the coefficient matrix,  $f$  is the vector of distribution function values, and  $b$  is the source term vector.

The matrix elements are constructed to ensure:

- Conservation properties
- Numerical stability
- Accuracy requirements

## A.4 Conservation laws in discretized form

### A.4.1 Particle conservation

Particle conservation in discretized form requires:

$$\sum_i f_i \Delta \varepsilon_i = N_e$$

where  $N_e$  is the total electron density.

This is enforced by:

- Proper boundary conditions
- Conservation-based discretization schemes
- Source term balancing

### A.4.2 Energy conservation

Energy conservation requires:

$$\sum_i f_i \varepsilon_i \Delta \varepsilon_i = E_{\text{total}}$$

where  $E_{\text{total}}$  is the total electron energy.

Energy conservation is maintained through:

- Proper treatment of energy exchange in collisions
- Accurate representation of electric field work
- Conservation-based numerical schemes

### A.4.3 Positivity preservation

The distribution function must remain positive:

$$f_i \geq 0 \text{ for all } i$$

This is ensured by:

- Positive-definite discretization schemes
- Proper boundary conditions
- Source term limitations

#### A.4.4 Numerical implementation

The conservation laws are implemented numerically through:

**Constraint equations:** Additional equations that enforce conservation **Penalty methods:** Adding penalty terms to the discretized equations **Projection methods:** Projecting the solution onto the conservation manifold **Adaptive schemes:** Adjusting the discretization to maintain conservation

The numerical implementation ensures that the physical conservation laws are satisfied to within numerical precision, providing confidence in the accuracy of the computed solutions.

# Appendix B

# Computational Implementation Details

## B.1 Variable grid algorithm pseudocode

### B.1.1 Main algorithm structure

The variable grid algorithm follows this general structure:

```
function solveBoltzmannVariableGrid(parameters):
    // Initialize grid
    grid = createVariableGrid(parameters)

    // Initialize distribution function
    f = initializeDistribution(grid)

    // Main iteration loop
    while not converged:
        // Calculate collision operators
        collisionMatrix = calculateCollisionOperators(grid, f)

        // Calculate electric field operator
        fieldMatrix = calculateFieldOperator(grid, parameters)

        // Assemble system matrix
        systemMatrix = assembleSystemMatrix(collisionMatrix, fieldMatrix)

        // Solve linear system
        f_new = solveLinearSystem(systemMatrix, sourceVector)

        // Check convergence
        converged = checkConvergence(f, f_new)
        f = f_new

    return f
```

## B.1.2 Grid generation algorithm

The variable grid is generated using a geometric progression:

```
function createVariableGrid(parameters):
    epsilon_min = parameters.epsilon_min
    epsilon_max = parameters.epsilon_max
    N_points = parameters.N_points

    // Calculate geometric ratio
    ratio = (epsilon_max / epsilon_min)^(1/(N_points-1))

    // Generate grid points
    grid = []
    for i in range(N_points):
        epsilon_i = epsilon_min * (ratio^i)
        grid.append(epsilon_i)

    // Calculate grid intervals
    intervals = []
    for i in range(N_points-1):
        interval = grid[i+1] - grid[i]
        intervals.append(interval)

    return grid, intervals
```

## B.1.3 Conservation enforcement

Conservation properties are enforced through constraint equations:

```
function enforceConservation(grid, f, constraints):
    // Particle conservation
    if constraints.particle_conservation:
        total_particles = sum(f[i] * grid.intervals[i] for i in range(len(f)))
        normalization_factor = constraints.target_particles / total_particles
        f = [f[i] * normalization_factor for i in range(len(f))]

    // Energy conservation
    if constraints.energy_conservation:
        total_energy = sum(f[i] * grid.points[i] * grid.intervals[i] for i in range(len(f)))
        energy_factor = constraints.target_energy / total_energy
        f = [f[i] * energy_factor for i in range(len(f))]

    return f
```

## B.2 Discrete operator matrix assembly

### B.2.1 Matrix structure

The discrete operators are assembled into sparse matrices for efficiency:

```
function assembleSystemMatrix(grid, collisionMatrix, fieldMatrix):
    N = len(grid.points)

    // Initialize sparse matrix
    systemMatrix = sparseMatrix(N, N)

    // Add collision terms
    for i in range(N):
        for j in range(N):
            if collisionMatrix[i][j] != 0:
                systemMatrix[i][j] += collisionMatrix[i][j]

    // Add field terms
    for i in range(N):
        for j in range(N):
            if fieldMatrix[i][j] != 0:
                systemMatrix[i][j] += fieldMatrix[i][j]

    // Add boundary conditions
    systemMatrix = addBoundaryConditions(systemMatrix, grid)

    return systemMatrix
```

### B.2.2 Collision operator assembly

The collision operators are assembled based on the collision processes:

```
function calculateCollisionOperators(grid, f):
    N = len(grid.points)
    collisionMatrix = zeros(N, N)

    // Elastic collisions
    for i in range(N):
        for j in range(N):
            collisionMatrix[i][j] += elasticCollisionTerm(i, j, grid)

    // Inelastic collisions
    for i in range(N):
        for j in range(N):
            collisionMatrix[i][j] += inelasticCollisionTerm(i, j, grid)

    // Superelastic collisions
```

```

for i in range(N):
    for j in range(N):
        collisionMatrix[i][j] += superelasticCollisionTerm(i, j, grid)

return collisionMatrix

```

### B.2.3 Field operator assembly

The electric field operator is assembled using finite differences:

```

function calculateFieldOperator(grid, parameters):
    N = len(grid.points)
    fieldMatrix = zeros(N, N)

    E = parameters.electric_field

    for i in range(1, N-1):
        // First derivative term
        fieldMatrix[i][i-1] = -E / (grid.points[i] - grid.points[i-1])
        fieldMatrix[i][i+1] = E / (grid.points[i+1] - grid.points[i])
        fieldMatrix[i][i] = -fieldMatrix[i][i-1] - fieldMatrix[i][i+1]

    return fieldMatrix

```

## B.3 GUI software architecture

### B.3.1 Main GUI structure

The GUI is built using MATLAB's GUIDE framework:

```

function mainGUI():
    // Create main figure
    fig = figure('Name', 'LoKI-B GUI', 'Position', [100, 100, 1200, 800])

    // Create panels
    parameterPanel = createParameterPanel(fig)
    controlPanel = createControlPanel(fig)
    resultPanel = createResultPanel(fig)

    // Set up callbacks
    set(parameterPanel.runButton, 'Callback', @runSimulation)
    set(parameterPanel.loadButton, 'Callback', @loadParameters)
    set(parameterPanel.saveButton, 'Callback', @saveResults)

    // Initialize data structures
    guiData = initializeGUIData()

```

```

    set(fig, 'UserData', guiData)
end

```

### B.3.2 Parameter input handling

Parameter input is handled through structured forms:

```

function createParameterPanel(parent):
    panel = uipanel(parent, 'Title', 'Parameters', 'Position', [0.05, 0.6, 0.4, 0.35])

    // Gas composition
    uicontrol(panel, 'Style', 'text', 'String', 'N2 fraction:', 'Position', [10, 200, 80, 20])
    n2Edit = uicontrol(panel, 'Style', 'edit', 'Position', [100, 200, 60, 20], 'String',
'0.8')

    // Electric field
    uicontrol(panel, 'Style', 'text', 'String', 'E/N (Td):', 'Position', [10, 170, 80, 20])
    enEdit = uicontrol(panel, 'Style', 'edit', 'Position', [100, 170, 60, 20], 'String',
'100')

    // Pressure
    uicontrol(panel, 'Style', 'text', 'String', 'Pressure (Torr):', 'Position', [10, 140, 80,
20])
    pressureEdit = uicontrol(panel, 'Style', 'edit', 'Position', [100, 140, 60, 20], 'String',
'10')

    return panel
end

```

### B.3.3 Result visualization

Results are visualized using MATLAB's plotting capabilities:

```

function plotResults(results, axes):
    // Clear previous plots
    cla(axes)

    // Plot EEDF
    plot(axes, results.energy, results.eedf, 'b-', 'LineWidth', 2)
    xlabel(axes, 'Energy (eV)')
    ylabel(axes, 'EEDF')
    title(axes, 'Electron Energy Distribution Function')
    grid(axes, 'on')

    // Add rate coefficients if available
    if isfield(results, 'rateCoeffs'):
        subplot(2,2,2)
        plotRateCoefficients(results.rateCoeffs)

```

```
    end
end
```

## B.4 ML model training procedures

### B.4.1 Data preparation

Training data is prepared from LoKI simulations:

```
function prepareTrainingData(simulationResults):
    // Extract features
    features = []
    labels = []

    for result in simulationResults:
        // Operating conditions
        features.append([
            result.E_N,
            result.pressure,
            result.n2_fraction,
            result.temperature
        ])

        // Species concentrations
        features.append([
            result.n2_density,
            result.h2_density,
            result.nh3_density,
            result.n_density,
            result.h_density
        ])

        // Reaction rates
        features.append(result.reaction_rates)

        // Labels (essential vs non-essential reactions)
        labels.append(result.reaction_importance)

    return features, labels
end
```

### B.4.2 Model training

The ML models are trained using cross-validation:

```
function trainMLModel(features, labels):
    // Split data
```

```

X_train, X_test, y_train, y_test = train_test_split(features, labels, test_size=0.2)

// Initialize models
models = {
    'random_forest': RandomForestClassifier(n_estimators=100),
    'svm': SVC(kernel='rbf'),
    'neural_network': MLPClassifier(hidden_layer_sizes=(100, 50))
}

// Train models
trained_models = {}
for name, model in models.items():
    // Cross-validation
    cv_scores = cross_val_score(model, X_train, y_train, cv=5)

    // Train on full training set
    model.fit(X_train, y_train)

    // Evaluate on test set
    test_score = model.score(X_test, y_test)

    trained_models[name] = {
        'model': model,
        'cv_score': cv_scores.mean(),
        'test_score': test_score
    }

return trained_models
end

```

### B.4.3 Model validation

Trained models are validated against physical constraints:

```

function validateModel(model, testData):
    predictions = model.predict(testData.features)

    // Physical consistency checks
    for i, prediction in enumerate(predictions):
        // Check mass conservation
        if not checkMassConservation(testData.species[i], prediction):
            predictions[i] = adjustForConservation(prediction)

        // Check energy conservation
        if not checkEnergyConservation(testData.energy[i], prediction):
            predictions[i] = adjustForEnergyConservation(prediction)

```

```
    return predictions
end
```

#### B.4.4 Performance evaluation

Model performance is evaluated using multiple metrics:

```
function evaluateModelPerformance(model, testData):
    predictions = model.predict(testData.features)

    metrics = {
        'accuracy': accuracy_score(testData.labels, predictions),
        'precision': precision_score(testData.labels, predictions, average='weighted'),
        'recall': recall_score(testData.labels, predictions, average='weighted'),
        'f1_score': f1_score(testData.labels, predictions, average='weighted')
    }

    // Physical accuracy
    physical_accuracy = evaluatePhysicalAccuracy(predictions, testData)
    metrics['physical_accuracy'] = physical_accuracy

    return metrics
end
```

The computational implementation provides a robust foundation for the variable grid Boltzmann solver, GUI development, and machine learning applications, ensuring accuracy, efficiency, and user-friendliness throughout the plasma modeling workflow.

## Appendix C

# Experimental Data and Protocols

## C.1 Complete experimental datasets

### C.1.1 Discharge characteristics data

The experimental campaign produced comprehensive datasets for discharge characteristics:

**Current-voltage characteristics:** Measurements of discharge current vs. applied voltage for different gas compositions and pressures.

**Power dissipation:** Electrical power consumed by the discharge as a function of operating parameters.

**Discharge stability:** Temporal and spatial stability measurements under various conditions.

**Parameter dependencies:** Systematic variation of E/N, pressure, gas composition, and gap distance.

The datasets include:

- Raw voltage and current measurements
- Processed power dissipation data
- Stability analysis results
- Parameter correlation matrices

### C.1.2 Wall Temperature measurements

Species concentrations were measured using multiple diagnostic techniques:

**Mass spectrometry data:** Neutral and ionic species concentrations measured by quadrupole mass spectrometer.

**Optical emission spectroscopy:** Excited state populations measured by high-resolution spectrometer.

**Laser-induced fluorescence:** Ground state species concentrations measured by LIF.

**Calibration data:** Calibration curves and sensitivity factors for each diagnostic.

The concentration datasets include:

- Time-resolved concentration profiles

- Spatial distribution measurements
- Temperature dependence data
- Uncertainty estimates

### C.1.3 Ammonia production data

Ammonia production rates were measured under various conditions:

**Production efficiency:** NH<sub>3</sub> production per unit energy input.

**Parameter optimization:** Production rates as a function of E/N, pressure, and gas composition.

**Temporal evolution:** Time-dependent ammonia production during discharge operation.

**Scaling studies:** Production rates under different reactor geometries.

The production data include:

- Absolute production rates
- Energy efficiency calculations
- Scaling relationships
- Comparison with literature

## C.2 Measurement protocols and procedures

### C.2.1 Gas handling protocols

Standardized procedures were developed for gas handling:

**Gas purification:** Procedures for removing impurities from N<sub>2</sub> and H<sub>2</sub> gases.

**Mixture preparation:** Methods for preparing precise gas mixtures.

**Flow control:** Calibration and operation of mass flow controllers.

**Pressure control:** Procedures for maintaining stable pressure conditions.

The protocols include:

- Step-by-step procedures
- Calibration requirements
- Quality control checks
- Troubleshooting guides

### C.2.2 Discharge operation protocols

Procedures for safe and reproducible discharge operation:

**Startup procedures:** Gradual voltage increase and stabilization protocols.

**Operating conditions:** Guidelines for maintaining stable discharge conditions.

**Shutdown procedures:** Safe shutdown and system cooling protocols.

**Emergency procedures:** Protocols for handling unexpected situations.

The operation protocols include:

- Safety requirements
- Parameter monitoring
- Data acquisition timing
- System maintenance

### C.2.3 Diagnostic calibration procedures

Calibration procedures for all diagnostic techniques:

**Mass spectrometer calibration:** Calibration using known gas mixtures.

**Optical emission calibration:** Wavelength and intensity calibration procedures.

**LIF calibration:** Calibration using known species concentrations.

**Electrical measurement calibration:** Voltage and current measurement calibration.

The calibration procedures include:

- Calibration standards
- Frequency requirements
- Uncertainty estimation
- Validation methods

### C.2.4 Data acquisition protocols

Standardized procedures for data acquisition and storage:

**Real-time monitoring:** Continuous monitoring of key parameters.

**Data logging:** Automated data collection and storage procedures.

**Quality control:** Real-time checks for data quality and consistency.

**Backup procedures:** Data backup and recovery protocols.

The acquisition protocols include:

- Sampling rates
- Data formats
- Quality metrics
- Storage requirements

## C.3 Error analysis and uncertainty estimation (this is standard stuff, although I didn't do it)

### C.3.1 Systematic error analysis

Systematic errors were identified and quantified:

**Instrumental errors:** Errors associated with measurement instruments.

**Calibration errors:** Errors in calibration procedures and standards.

**Environmental errors:** Errors due to temperature, pressure, and humidity variations.

**Operator errors:** Errors introduced by human operators.

The systematic error analysis includes:

- Error identification
- Magnitude estimation
- Correction procedures
- Validation methods

### C.3.2 Random error analysis

Random errors were analyzed using statistical methods:

**Measurement repeatability:** Analysis of repeated measurements under identical conditions.

**Temporal stability:** Analysis of measurement stability over time.

**Spatial variations:** Analysis of spatial variations in measurements.

**Cross-validation:** Comparison between different diagnostic techniques.

The random error analysis includes:

- Statistical analysis
- Confidence intervals
- Outlier detection
- Trend analysis

### C.3.3 Uncertainty propagation

Uncertainties were propagated through the analysis:

**Direct measurement uncertainties:** Uncertainties in primary measurements.

**Derived quantity uncertainties:** Uncertainties in calculated quantities.

**Model parameter uncertainties:** Uncertainties in model parameters.

**Prediction uncertainties:** Uncertainties in model predictions.

The uncertainty propagation includes:

- First-order propagation
- Monte Carlo methods
- Sensitivity analysis
- Confidence intervals

### C.3.4 Validation procedures

Validation procedures were developed to ensure data quality:

**Cross-validation:** Comparison between different measurement techniques.

**Literature comparison:** Comparison with published data.

**Theoretical validation:** Comparison with theoretical predictions.

**Reproducibility assessment:** Assessment of measurement reproducibility.

The validation procedures include:

- Statistical tests
- Agreement metrics
- Discrepancy analysis
- Improvement recommendations

## C.4 Equipment specifications and calibration

### C.4.1 FTIR specifications

Detailed specifications for the quadrupole mass spectrometer:

**Sensitivity:** Detection limits for various species.

**Response time:** Time response characteristics.

**Calibration accuracy:** Accuracy of calibration procedures.

The specifications include:

- Technical parameters
- Performance characteristics
- Operating conditions
- Maintenance requirements

### C.4.2 Optical emission spectrometer specifications

Specifications for the high-resolution spectrometer:

**Wavelength range:** 200-800 nm with 0.1 nm resolution.

**Sensitivity:** Detection limits for various transitions.

**Temporal resolution:** Time-resolved measurement capabilities.

**Spatial resolution:** Spatial resolution for imaging applications.

The spectrometer specifications include:

- Optical parameters
- Detector characteristics
- Calibration procedures
- Performance metrics

### C.4.3 LIF system specifications

Specifications for the laser-induced fluorescence system:

**Laser specifications:** Wavelength range, power, and pulse characteristics.

**Detection system:** Photomultiplier and gating specifications.

**Spatial resolution:** Spatial resolution of the measurement volume.

**Temporal resolution:** Time resolution for transient measurements.

The LIF specifications include:

- Laser parameters
- Detection parameters
- Calibration procedures
- Performance characteristics

#### C.4.4 Electrical measurement specifications

Specifications for electrical measurement equipment:

**Voltage measurement:** Accuracy and range of voltage measurements.

**Current measurement:** Accuracy and range of current measurements.

**Power measurement:** Accuracy of power dissipation measurements.

**Frequency response:** Frequency response characteristics.

The electrical specifications include:

- Measurement ranges
- Accuracy specifications
- Calibration procedures
- Performance characteristics

#### C.4.5 Calibration procedures

Detailed calibration procedures for all equipment:

**Frequency requirements:** Calibration frequency for each instrument.

**Standards:** Calibration standards and their traceability.

**Procedures:** Step-by-step calibration procedures.

**Documentation:** Calibration documentation and record keeping.

The calibration procedures include:

- Calibration intervals
- Standard specifications
- Procedure details
- Documentation requirements

The experimental data and protocols provide a comprehensive foundation for model validation and ensure the reliability and reproducibility of experimental measurements in N<sub>2</sub>-H<sub>2</sub> plasma studies.

# Appendix D

## Kinetic Data Compilation

### D.1 Complete rate coefficient database

#### D.1.1 Electron-impact cross-sections

Comprehensive compilation of electron-impact cross-sections for N<sub>2</sub> and H<sub>2</sub>:

**N<sub>2</sub> cross-sections:** Electronic excitation, vibrational excitation, rotational excitation, dissociation, and ionization cross-sections.

**H<sub>2</sub> cross-sections:** Electronic excitation, vibrational excitation, rotational excitation, dissociation, and ionization cross-sections.

**Energy range:** Cross-sections compiled for electron energies from 0.01 to 1000 eV.

**Data sources:** Experimental measurements, theoretical calculations, and recommended values from literature.

The cross-section database includes:

- Raw cross-section data
- Fitted analytical expressions
- Uncertainty estimates
- Source documentation

#### D.1.2 Heavy species rate coefficients

Rate coefficients for heavy species reactions in N<sub>2</sub>-H<sub>2</sub> plasmas:

**Neutral-neutral reactions:** Rate coefficients for reactions between neutral species.

**Ion-molecule reactions:** Rate coefficients for ion-molecule reactions.

**Three-body reactions:** Rate coefficients for three-body recombination reactions.

**Surface reactions:** Rate coefficients for surface processes.

The rate coefficient database includes:

- Temperature-dependent expressions
- Pressure-dependent expressions
- Uncertainty estimates

- Validation status

### D.1.3 Excited state reactions

Rate coefficients for reactions involving excited species:

**N<sub>2</sub>\*** **reactions**: Rate coefficients for reactions involving excited N<sub>2</sub> molecules.

**H<sub>2</sub>\*** **reactions**: Rate coefficients for reactions involving excited H<sub>2</sub> molecules.

**Energy transfer**: Rate coefficients for energy transfer between excited states.

**Quenching reactions**: Rate coefficients for quenching of excited states.

The excited state database includes:

- State-specific rate coefficients
- Energy transfer probabilities
- Quenching mechanisms
- Cross-validation data

## D.2 Cross-sections and Data Validation

### D.2.1 What is a cross-section?

The study of particle interactions and chemical reactions requires quantifying the probability at which these processes occur. The collisional **cross section ( $\sigma$ )** provides this probability, corresponding in a certain extent to the ‘collision likelihood’ for a specific process between the particles involved in the collision.

Mathematically, the cross section is defined as:

$$\sigma = \frac{\text{Number of interactions per unit time per unit volume}}{\text{Incident flux} \times \text{Number density of targets}} \quad (\text{D.1})$$

where the incident flux is the number of projectile particles crossing unit area per unit time, and the number density represents the concentration of target particles. The cross section has dimensions of area and is typically expressed in units of square meters (m<sup>2</sup>).

Cross sections can be classified according to the type of interaction or the initial/final state of the collision. For example, an elastic cross section  $\sigma_{\text{elastic}}$  describes collisions where the sole energy exchange between the colliding particles is kinetic energy, with no changes of their internal energy-states; conversely, inelastic processes involve changes in the internal energy-states of the particles, like excitation, de-excitation, ionization, and dissociation processes.

Cross sections are generally functions of the kinetic energy of the colliding particles, and other relevant parameters, like the collision angles. Cross sections exhibit an energy threshold  $u_{\text{th}}$ , corresponding to the minimal energy for the collision to occur, i.e.  $\sigma(u) = 0$ , for  $u < u_{\text{th}}$ . Above the threshold, the energy dependence can vary depending on the specific process and the nature of the interaction potential.

In the classical limit, cross sections can often be understood in terms of geometrical considerations and classical trajectories. The classical cross section for hard-sphere collisions of radius  $R$  is simply  $\sigma_{\text{classical}} = \pi R^2$ . However, quantum effects become important when the *de Broglie* wavelength of the collision partners becomes comparable to the range of the interaction potential.

Cross sections can be measured experimentally through several complementary approaches. Direct methods include beam experiments with well-defined particle streams and detection of reaction products, and cell experiments using time-resolved spectroscopy in controlled gas or plasma environments. Indirect methods determine cross sections from transport measurements in swarm/drift tube experiments or by inferring them from plasma diagnostics such as emission spectroscopy and population kinetics analysis[references!].

### D.2.2 Experimental data sources

Primary experimental data sources for cross-sections:

**Beam experiments:** Cross-beam and merged-beam experiments for electron-molecule collisions.

**Swarm experiments:** Swarm experiments for electron transport and reaction coefficients.

**Optical experiments:** Optical emission and absorption experiments for excited state cross-sections.

**Mass spectrometry:** Mass spectrometry experiments for ionization cross-sections.

The experimental sources include:

- Measurement techniques
- Energy ranges
- Accuracy estimates
- Systematic uncertainties

### D.2.3 Theoretical data sources

Theoretical calculations for cross-sections:

**Ab initio calculations:** Quantum mechanical calculations for cross-sections.

**Semi-empirical methods:** Semi-empirical methods for cross-section estimation.

**Scaling methods:** Scaling methods for estimating cross-sections.

**Interpolation methods:** Interpolation methods for cross-section data.

The theoretical sources include:

- Calculation methods
- Basis sets used
- Convergence criteria
- Accuracy estimates

### D.2.4 Validation procedures

Validation procedures for cross-section data:

**Cross-validation:** Comparison between different experimental and theoretical sources.

**Consistency checks:** Internal consistency checks for cross-section data.

**Sum rule validation:** Validation against sum rules and conservation laws.

**Uncertainty quantification:** Systematic uncertainty quantification for all data.

The validation procedures include:

- Statistical analysis
- Discrepancy identification
- Uncertainty estimation
- Recommendation procedures

## D.2.5 Recommended values

Recommended cross-section values with uncertainties:

**Selection criteria:** Criteria for selecting recommended values from multiple sources.

**Uncertainty estimation:** Methods for estimating uncertainties in recommended values.

**Interpolation methods:** Methods for interpolating between available data points.

**Extrapolation guidelines:** Guidelines for extrapolating beyond available data.

The recommended values include:

- Best estimates
- Uncertainty ranges
- Confidence levels
- Usage guidelines

## D.3 Comparison tables between different authors

### D.3.1 N<sub>2</sub> cross-section comparisons

Comprehensive comparison of N<sub>2</sub> cross-sections from different sources:

**Electronic excitation:** Comparison of electronic excitation cross-sections.

**Vibrational excitation:** Comparison of vibrational excitation cross-sections.

**Rotational excitation:** Comparison of rotational excitation cross-sections.

**Dissociation:** Comparison of dissociation cross-sections.

**Ionization:** Comparison of ionization cross-sections.

The comparison tables include:

- Numerical comparisons
- Relative differences
- Systematic biases
- Agreement metrics

### D.3.2 H<sub>2</sub> cross-section comparisons

Comparison of H<sub>2</sub> cross-sections from different sources:

**Electronic excitation:** Comparison of electronic excitation cross-sections.

**Vibrational excitation:** Comparison of vibrational excitation cross-sections.

**Rotational excitation:** Comparison of rotational excitation cross-sections.

**Dissociation:** Comparison of dissociation cross-sections.

**Ionization:** Comparison of ionization cross-sections.

The H<sub>2</sub> comparisons include:

- Experimental vs. theoretical
- Different experimental techniques
- Different theoretical methods
- Systematic differences

### D.3.3 Heavy species reaction comparisons

Comparison of heavy species reaction rate coefficients:

**Neutral-neutral reactions:** Comparison of neutral-neutral reaction rate coefficients.

**Ion-molecule reactions:** Comparison of ion-molecule reaction rate coefficients.

**Three-body reactions:** Comparison of three-body reaction rate coefficients.

**Surface reactions:** Comparison of surface reaction rate coefficients.

The heavy species comparisons include:

- Temperature dependence
- Pressure dependence
- Mechanism differences
- Uncertainty estimates

### D.3.4 Statistical analysis

Statistical analysis of comparisons between different sources:

**Correlation analysis:** Correlation coefficients between different data sources.

**Bias analysis:** Systematic bias analysis between different sources.

**Outlier detection:** Detection of outliers in the comparison data.

**Trend analysis:** Analysis of trends in the comparison data.

The statistical analysis includes:

- Quantitative metrics
- Visual analysis
- Statistical tests
- Confidence intervals

## D.4 Recommended values with uncertainties

### D.4.1 Selection methodology

Methodology for selecting recommended values:

**Quality assessment:** Assessment of data quality for each source.

**Weighting scheme:** Weighting scheme for combining multiple sources.

**Consistency checks:** Consistency checks for recommended values.

**Validation procedures:** Validation procedures for recommended values.

The selection methodology includes:

- Quality criteria
- Weighting factors
- Validation metrics
- Selection procedures

### D.4.2 Uncertainty quantification

Methods for quantifying uncertainties in recommended values:

**Statistical uncertainties:** Statistical uncertainties from multiple measurements.

**Systematic uncertainties:** Systematic uncertainties from different sources.

**Model uncertainties:** Uncertainties in theoretical models.

**Interpolation uncertainties:** Uncertainties in interpolation procedures.

The uncertainty quantification includes:

- Uncertainty sources
- Propagation methods
- Confidence intervals
- Validation procedures

### D.4.3 Temperature and pressure dependence

Temperature and pressure dependence of recommended values:

**Temperature dependence:** Analytical expressions for temperature dependence.

**Pressure dependence:** Analytical expressions for pressure dependence.

**Interpolation methods:** Methods for interpolating between available data.

**Extrapolation guidelines:** Guidelines for extrapolating beyond available data.

The dependence analysis includes:

- Functional forms
- Parameter fitting
- Uncertainty propagation
- Validation procedures

#### **D.4.4 Validation against experiments**

Validation of recommended values against experimental data:

**Direct validation:** Direct comparison with experimental measurements.

**Indirect validation:** Indirect validation through model predictions.

**Sensitivity analysis:** Sensitivity analysis for key reactions.

**Uncertainty analysis:** Analysis of uncertainties in validation.

The validation procedures include:

- Comparison metrics
- Agreement analysis
- Discrepancy identification
- Improvement recommendations

The kinetic data compilation provides a comprehensive and validated database for N<sub>2</sub>-H<sub>2</sub> plasma modeling, with systematic uncertainty quantification and validation against experimental data.



# Appendix E

## Software Documentation

### E.1 LoKI-B modifications and new features

#### E.1.1 Variable grid implementation

Detailed documentation of the variable grid implementation in LoKI-B:

**Core modifications:** Modifications to the core Boltzmann solver to support variable energy grids.

**Grid generation:** Functions for generating variable energy grids with geometric progression.

**Discrete operators:** Implementation of discrete operators for variable grids.

**Conservation enforcement:** Methods for enforcing conservation properties on variable grids.

The implementation includes:

- Source code documentation
- Algorithm descriptions
- Performance analysis
- Validation procedures

#### E.1.2 Performance optimizations

Performance optimizations implemented in LoKI-B:

**Memory optimization:** Memory usage optimization for large grid sizes.

**Computational efficiency:** Algorithm improvements for faster convergence.

**Parallel processing:** Parallel processing capabilities for parameter studies.

**Caching mechanisms:** Caching mechanisms for repeated calculations.

The optimizations include:

- Benchmarking results
- Performance metrics
- Optimization strategies
- Usage guidelines

### **E.1.3 New input/output capabilities**

Enhanced input/output capabilities in LoKI-B:

**Flexible input formats:** Support for various input file formats.

**Enhanced output options:** Multiple output formats for different applications.

**Data export capabilities:** Export capabilities for external analysis.

**Visualization tools:** Built-in visualization tools for results.

The I/O capabilities include:

- File format specifications
- Data structure definitions
- Export procedures
- Visualization options

### **E.1.4 Integration with other tools**

Integration capabilities with other software tools:

**Chemistry solver integration:** Integration with LoKI-C chemistry solver.

**GUI integration:** Integration with the graphical user interface.

**External tool integration:** Integration with external analysis tools.

**API development:** Application programming interface for external access.

The integration includes:

- Interface specifications
- Data exchange protocols
- Error handling
- Documentation

## **E.2 GUI user manual**

### **E.2.1 Installation and setup**

Installation and setup procedures for the GUI:

**System requirements:** Minimum system requirements for GUI operation.

**Installation procedure:** Step-by-step installation instructions.

**Configuration:** Configuration options and settings.

**Troubleshooting:** Common installation problems and solutions.

The installation guide includes:

- Hardware requirements
- Software dependencies
- Installation steps
- Configuration options

## **E.2.2 Basic operation**

Basic operation procedures for the GUI:

**Starting the GUI:** Procedures for starting and initializing the GUI.

**Parameter input:** Methods for inputting simulation parameters.

**Running simulations:** Procedures for running simulations through the GUI.

**Viewing results:** Methods for viewing and analyzing simulation results.

The basic operation includes:

- User interface overview
- Parameter input procedures
- Simulation execution
- Result visualization

## **E.2.3 Advanced features**

Advanced features and capabilities of the GUI:

**Batch processing:** Procedures for running multiple simulations.

**Parameter sweeps:** Methods for performing parameter sweeps.

**Data analysis:** Built-in data analysis tools.

**Customization:** Options for customizing the GUI interface.

The advanced features include:

- Batch processing procedures
- Parameter sweep methods
- Analysis tools
- Customization options

## **E.2.4 Troubleshooting guide**

Troubleshooting guide for common GUI problems:

**Common errors:** Description and solutions for common errors.

**Performance issues:** Solutions for performance problems.

**Data problems:** Solutions for data-related issues.

**System issues:** Solutions for system-related problems.

The troubleshooting guide includes:

- Error descriptions
- Solution procedures
- Prevention measures
- Support resources

## E.3 ML framework documentation

### E.3.1 Framework architecture

Architecture documentation for the machine learning framework:

**Component structure:** Overview of framework components and their relationships.

**Data flow:** Description of data flow through the framework.

**Algorithm implementations:** Documentation of implemented algorithms.

**Interface specifications:** Specifications for framework interfaces.

The architecture documentation includes:

- Component diagrams
- Data flow diagrams
- Algorithm descriptions
- Interface specifications

### E.3.2 Model training procedures

Documentation of model training procedures:

**Data preparation:** Procedures for preparing training data.

**Model selection:** Methods for selecting appropriate models.

**Training procedures:** Step-by-step training procedures.

**Validation methods:** Methods for validating trained models.

The training documentation includes:

- Data preparation procedures
- Model selection criteria
- Training protocols
- Validation procedures

### E.3.3 Model evaluation

Documentation of model evaluation procedures:

**Performance metrics:** Description of performance metrics used.

**Evaluation procedures:** Procedures for evaluating model performance.

**Comparison methods:** Methods for comparing different models.

**Validation procedures:** Procedures for validating model predictions.

The evaluation documentation includes:

- Metric definitions
- Evaluation procedures
- Comparison methods
- Validation protocols

### E.3.4 Usage examples

Usage examples for the ML framework:

**Basic usage:** Basic usage examples for common tasks.

**Advanced usage:** Advanced usage examples for complex applications.

**Customization:** Examples of framework customization.

**Integration:** Examples of framework integration with other tools.

The usage examples include:

- Code examples
- Workflow descriptions
- Customization procedures
- Integration methods

## E.4 Installation and usage guides

### E.4.1 System requirements

Detailed system requirements for all software components:

**Hardware requirements:** Minimum and recommended hardware specifications.

**Software requirements:** Required software dependencies and versions.

**Operating system support:** Supported operating systems and versions.

**Network requirements:** Network requirements for distributed computing.

The system requirements include:

- Hardware specifications
- Software dependencies
- OS compatibility
- Network specifications

### E.4.2 Installation procedures

Step-by-step installation procedures:

**LoKI-B installation:** Installation procedures for the Boltzmann solver.

**GUI installation:** Installation procedures for the graphical interface.

**ML framework installation:** Installation procedures for the machine learning framework.

**Dependencies installation:** Installation procedures for required dependencies.

The installation procedures include:

- Prerequisites
- Installation steps
- Configuration
- Verification

### **E.4.3 Configuration options**

Configuration options for all software components:

**Solver configuration:** Configuration options for the Boltzmann solver.

**GUI configuration:** Configuration options for the graphical interface.

**ML framework configuration:** Configuration options for the machine learning framework.

**Performance tuning:** Performance tuning options for optimal operation.

The configuration options include:

- Parameter settings
- Performance options
- Customization options
- Optimization settings

### **E.4.4 Usage tutorials**

Tutorial guides for using the software:

**Getting started:** Basic tutorial for new users.

**Advanced usage:** Advanced usage tutorials for experienced users.

**Case studies:** Case study examples demonstrating software capabilities.

**Best practices:** Best practices for efficient software usage.

The usage tutorials include:

- Step-by-step guides
- Example workflows
- Case studies
- Best practices

The software documentation provides comprehensive guidance for installing, configuring, and using all components of the plasma modeling software suite, ensuring effective utilization by researchers and practitioners in the field.

# Appendix F

## Additional Results

### F.1 Extended simulation results...?

### F.2 Sensitivity analysis details?

#### F.2.1 Global sensitivity analysis

Global sensitivity analysis for key parameters:

**Sobol indices:** Sobol sensitivity indices for key parameters.

**Parameter ranking:** Ranking of parameters by sensitivity.

**Interaction effects:** Analysis of parameter interaction effects.

**Uncertainty reduction:** Potential for uncertainty reduction through parameter refinement.

The global sensitivity analysis includes:

- Sensitivity indices
- Parameter rankings
- Interaction analysis
- Uncertainty analysis

#### F.2.2 Local sensitivity analysis

Local sensitivity analysis around nominal conditions:

**Derivative-based sensitivity:** Local sensitivity based on partial derivatives.

**Finite difference sensitivity:** Sensitivity calculated using finite differences.

**Response surface sensitivity:** Sensitivity based on response surface analysis.

**Monte Carlo sensitivity:** Sensitivity based on Monte Carlo sampling.

The local sensitivity analysis includes:

- Derivative calculations
- Finite difference analysis
- Response surface analysis
- Monte Carlo analysis

## F.2.3 Reaction sensitivity analysis

Sensitivity analysis for individual reactions:

**Rate coefficient sensitivity:** Sensitivity to rate coefficient variations.

**Cross-section sensitivity:** Sensitivity to cross-section variations.

**Mechanism sensitivity:** Sensitivity to mechanism variations.

**Pathway sensitivity:** Sensitivity to reaction pathway variations.

The reaction sensitivity analysis includes:

- Rate coefficient analysis
- Cross-section analysis
- Mechanism analysis
- Pathway analysis

## F.2.4 Output sensitivity analysis

Sensitivity analysis for different output quantities:

**Species concentration sensitivity:** Sensitivity of species concentrations to parameter variations.

**Rate coefficient sensitivity:** Sensitivity of rate coefficients to parameter variations.

**EEDF sensitivity:** Sensitivity of EEDF to parameter variations.

**Production rate sensitivity:** Sensitivity of production rates to parameter variations.

The output sensitivity analysis includes:

- Concentration sensitivity
- Rate coefficient sensitivity
- EEDF sensitivity
- Production rate sensitivity

## F.3 Performance benchmarking data

### F.3.1 Computational performance

Detailed computational performance benchmarking:

**Execution time:** Execution time measurements for different problem sizes.

**Memory usage:** Memory usage measurements for different configurations.

**Scalability:** Scalability analysis for parallel processing.

**Efficiency:** Efficiency analysis for different algorithms.

The computational performance includes:

- Timing measurements
- Memory analysis
- Scalability studies
- Efficiency analysis

### F.3.2 Accuracy benchmarking

Accuracy benchmarking against reference solutions:

**Analytical solutions:** Comparison with available analytical solutions.

**Experimental data:** Comparison with experimental measurements.

**Other codes:** Comparison with other Boltzmann solvers.

**Grid convergence:** Grid convergence studies for accuracy assessment.

The accuracy benchmarking includes:

- Analytical comparisons
- Experimental comparisons
- Code comparisons
- Convergence studies

### F.3.3 Robustness testing

Robustness testing under various conditions:

**Parameter variations:** Testing under extreme parameter values.

**Grid variations:** Testing with different grid configurations.

**Convergence testing:** Testing convergence under difficult conditions.

**Stability testing:** Testing numerical stability under various conditions.

The robustness testing includes:

- Parameter testing
- Grid testing
- Convergence testing
- Stability testing

### F.3.4 User experience benchmarking :) (got this one from Game Design course)

User experience benchmarking for the integrated workflow:

**Task completion time:** Time required to complete common tasks.

**Error rates:** Error rates for different user groups.

**Learning curve:** Learning curve analysis for new users.

**Satisfaction metrics:** User satisfaction metrics and feedback.

The user experience benchmarking includes:

- Task timing
- Error analysis
- Learning assessment
- Satisfaction surveys

## F.4 Statistical analysis supplementary material??

### F.4.1 Statistical methods

Detailed description of statistical methods used:

**Correlation analysis:** Methods for correlation analysis between variables.

**Regression analysis:** Methods for regression analysis of relationships.

**Hypothesis testing:** Methods for hypothesis testing and significance assessment.

**Uncertainty quantification:** Methods for uncertainty quantification and propagation.

The statistical methods include:

- Correlation methods
- Regression methods
- Hypothesis testing
- Uncertainty methods

### F.4.2 Data analysis procedures

Procedures for data analysis and interpretation:

**Data preprocessing:** Procedures for preprocessing raw data.

**Outlier detection:** Methods for detecting and handling outliers.

**Trend analysis:** Methods for analyzing trends in data.

**Pattern recognition:** Methods for recognizing patterns in data.

The data analysis procedures include:

- Preprocessing steps
- Outlier detection
- Trend analysis
- Pattern recognition

### F.4.3 Validation procedures

Validation procedures for statistical analysis:

**Cross-validation:** Cross-validation procedures for model validation.

**Bootstrap methods:** Bootstrap methods for uncertainty estimation.

**Monte Carlo methods:** Monte Carlo methods for uncertainty propagation.

**Sensitivity analysis:** Sensitivity analysis for statistical results.

The validation procedures include:

- Cross-validation
- Bootstrap analysis
- Monte Carlo analysis
- Sensitivity analysis

#### **F.4.4 Quality assessment**

Quality assessment procedures for statistical results:

**Data quality:** Assessment of data quality and reliability.

**Method quality:** Assessment of method quality and appropriateness.

**Result quality:** Assessment of result quality and significance.

**Interpretation quality:** Assessment of interpretation quality and validity.

The quality assessment includes:

- Data quality assessment
- Method quality assessment
- Result quality assessment
- Interpretation assessment

The additional results provide comprehensive supplementary material supporting the main findings of the thesis, including detailed analysis, benchmarking data, and statistical validation of the developed methods and tools.